ECHO MAPPING OF ACTIVE GALACTIC NUCLEI

Thesis submitted to CHRIST (Deemed to be University)

for the award of the Degree of

DOCTOR OF PHILOSOPHY

IN

PHYSICS

by

AMIT KUMAR MANDAL

Under the Supervision of

BLESSON MATHEW
Assistant Professor

C S STALIN
Professor
Indian Institute of Astrophysics, Bengaluru

CENTRE FOR RESEARCH
CHRIST (Deemed to be University)
BENGALURU

JUNE 2021

Dedicated to

my

family, teachers and friends

DECLARATION

I hereby declare that the research work contained in this thesis titled 'ECHO MAPPING OF ACTIVE GALACTIC NUCLEI' is the result of the investigations undertaken by me at the CHRIST (Deemed to be University), Bengaluru under the supervision of Dr. Blesson Mathew, Assistant Professor at CHRIST (Deemed to be University), Bengaluru and Dr. C S Stalin, Professor at Indian Institute of Astrophysics, Bengaluru. This work has not been submitted for the award of any other degree, diploma, associateship, fellowship, etc. of any other University or Institute.

I hearby confirm the originality of the work and that there is no plagiarism in any part of the dissertation.

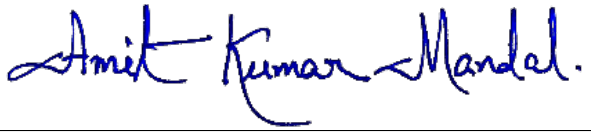

Name and signature of the Research Scholar
Amit Kumar Mandal
Reg. No. 1740077
Department of Physics and Electronics
School of Sciences
CHRIST (Deemed to be University)
Bengaluru 560 029
Karnataka, India

Place: Bengaluru

Date: 29 June 2021

CERTIFICATE

This is to certify that the thesis titled 'ECHO MAPPING OF ACTIVE GALACTIC NUCLEI' submitted to the CHRIST (Deemed to be University) by Mr. Amit Kumar Mandal for the award of the degree of Doctor of Philosophy, is based on the results of the investigations carried out by him under our supervision and guidance, at the CHRIST (Deemed to be University), Bengaluru in collaboration with the Indian Institute of Astrophysics, Bengaluru.

This thesis has not been submitted for the award of any other degree, diploma, associateship, fellowship, etc. of any other University or Institute.

Name and signature of the Supervisors

Dr. Blesson Mathew

Assistant Professor

Department of Physics and Electronics

School of Sciences

CHRIST (Deemed to be University)

Bengaluru 560 029

Karnataka, India

and

Dr. C S Stalin

Professor

Indian Institute of Astrophysics

Bengaluru 560 034

Karnataka, India

Place: Bengaluru

Date: 29 June 2021

ACKNOWLEDGEMENT

I sincerely thank all the people whose companionship and help have helped me to move on with my life. I like to express my cordial gratitude to my Supervisors Dr. C. S. Stalin and Dr. Blesson Mathew for their continuous support, guidance and motivation throughout my Ph.D. work. Their spontaneous energy, passion and dedications towards their work always motivate me to think and explore new things. I am specially thankful to Prof. Ram Sagar, senior scientist, National Academy of Sciences, India (NASI) for mentoring and providing research grants during my Ph.D. I also acknowledge the financial support from NASI, India to conduct my thesis work. I would like to thank my senior and collaborator Dr. Suvendu Rakshit for helping me to carry out my research work. I am thankful to be a part of a good research group and acknowledge all the the support from Priyanka, Bhoomika, Kshama and Indrani.

I acknowledge all the discussions with my collaborators Drs. Sebastian Hoenig, Poshak Gandhi, M. B. Pandge, R. G. Petrov, S. Muneer. I specially thank Prof. Jean Surdej to work under his guidance at Université de Liège, Belgium under the scholarship "Erasmus + International Credit Mobility" and Dr. Dominika Wylezalek and Prof. M. K. Patig for giving opportunity for carrying out research at the European Southern Observatory (ESO) under the Alexander von Humboldt Foundation, Germany under the Group linkage long-term research program between IIA, Bengaluru and ESO, Garching, Germany.

I am thankful to all the supporting staff, specially Pramod, Kiran, Sujith, Anaswar at CREST, Hoskote and the Indian Astronomical Observatory (IAO), operated by IIA, Bengaluru for carrying out observations and providing data used in this thesis.

It is my fortunate to have friends like Samrat, Chayan, Snehalata, Di-

panweeta, Rubinur, Prolay, Anirban, Megha, Prasanta, Avrajit, Bikram, Avinash, Aritra, Raghubar, Debjit, Piyali, Priya, Adira, Anohita, Gourav, Akshaya, Prajwal, Kashyap and Arun who are always there with me to support.

I want to thank Dr. Paul KT, Head of the Department, Prof. Shivappa B Gudennavar, Associate Director, Centre for Research and Dr. Sreeja Kartha, assistant professor for their academic support.

I am indebted to all my school and college teachers without whom I could not have reached this place.

I acknowledge the support from the Centre for Research, CHRIST (Deemed to be University) for providing me the opportunity to conduct my research.

I am thankful to the Director, IIA for providing institutional infrastructural support during this work.

Last but not the least, I would like to thank my parents Mrs. Aloka Mandal and Mr. Jagannath Mandal for their blessings and continuous support in my life. I thank my beloved brother Mr. Arabinda Mandal and sister-in-law Mrs. Shreyasi Dey for being with me, especially during the hardest days of this journey.

Amit Kumar Mandal

DATA USAGE

The research work carried out in this thesis has used data from various ground and space based telescopes. I thankfully acknowledge all the data usage from several space and ground based telescopes and all the members of the respective teams who made the data available.

Major part of the thesis work constitutes data from the 2 m Himalayan Chandra Telescope (HCT), situated at Hanle, owned and operated by the Indian Institute of Astrophysics, Bengaluru. HCT is operated remotely from CREST, Hoskote near Bengaluru through a dedicated satellite link provided by the Indian Space Research Organisation (ISRO). I cordially thank all the supporting members involved at the various work-stations associated with the HCT.

I used the *Gaia* DR2 catalogue that contains data from the all sky astrometric and photometric survey with accurate positions for about 1.7 billion sources and proper motion and parallax measurements for about 1.3 billion sources. *Gaia* is operated by the European Space Agency (ESA). I also used data from the Sloan Digital Sky Survey (SDSS) that provides multicolor, deep images covering more than a quarter of the sky.

I used the 8.2 m Subaru Telescope situated at Hawaii operated by the Mauna Kea Observatories and National Astronomical Observatory of Japan.

I also used the Prompt 8, a 60 cm robotic telescope from Skynet. The telescope is located at the Cerro Tololo Inter American Observatory.

Also, I used data retrieved from several published papers. I thank all the authors of the respective articles.

ABSTRACT

Active galactic nuclei (AGN) are the persistent high luminosity sources powered by accretion of matter onto super massive black holes (SMBHs) at their centres. They are known to show flux variation and this property can be used as an effective tool to map the extent of the broad line region (BLR) and the dusty torus that surrounds the central SMBH. Though the mass of the SMBH (M_{BH}) can be directly measured using the dynamics of stars that are close to the SMBH, this method is limited to objects in the low redshift Universe ($z < 0.1$). On the other hand, the technique of reverberation mapping (RM) can provide M_{BH} estimate over a range of redshifts. RM is based on the light travel time delayed response of the line emitting gas as well as the re-processed torus emission to changes in the continuum emission from the accretion disk. As of now, M_{BH} measurements are available for more than 100 sources based on RM. The obtained BLR sizes (R_{BLR}) are found to be correlated with the optical luminosity (L_{5100}) at wavelength 5100 Å. This relationship is obtained based on measurements of AGN available over a limited range of luminosity. Moreover, many of these measurements also have larger error bars. Therefore, there is an urgent need to increase RM measurements with small errors on more AGN covering a wide range of redshifts to better constrain the $R_{BLR} - L_{5100}$ relation. We have carried out photometric reverberation observations on the AGN Mrk 590. Using both broad band (that overlaps with the continuum) and narrow band (that overlaps with the Hα emission line) observations, we found the BLR size to be $21.44^{+1.49}_{-2.11}$ days, which is equivalent to $0.018^{+0.001}_{-0.002}$ pc. Using this measured BLR size and the full width at half maximum of the Hα line measured from the newly acquired Subaru spectrum we found a black hole mass of $1.96^{+0.15}_{-0.21} \times 10^8\,M_\odot$, using virial relationship and adopting a scale factor of 1.12.

Similar to BLR reverberation mapping, the extent of the dusty torus in AGN can also be measured using dust reverberation mapping (DRM) based on the delayed response of the near infrared (NIR) flux from the torus to the ionizing UV/optical continuum coming from the accretion disk. From these observations too, a strong correlation is known to exist between the torus size (R_{dust}) and the optical luminosity (L_V). Based on the $R_{dust} - L_V$ relation, it is also possible to use AGN as standard candle to constrain the Hubble constant (H_0) and other cosmological parameters. But for that, a large number of DRM observations are needed at different redshifts. As of today, very few NIR interferometric observations are available, but measurements of the torus size via such direct imaging observations are again limited to very near and bright AGN. Moreover, there is a large discrepancy in the size of the torus obtained via the direct imaging method through interferometry and that obtained from DRM. From long term monitoring in the optical and infra-red, we found the inner edge of the dust torus in H0507+164 and Z229−15 to lie at a distance of $0.029^{+0.010}_{-0.008}$ pc and $0.017^{+0.005}_{-0.005}$ pc, respectively, from the central optical continuum source. These two new measurements are also found to lie closely on the known $R_{dust} - L_V$ relation line. Also, by modeling the available BLR RM data in the literature, it is possible to constrain the size, structure and kinematics of the BLR using Bayesian approach. This approach is adopted several times to study the BLR morphology by different ways but is not applied to a large number of sources in an homogeneous manner. From an analysis of the RM data for a total of 57 sources following a Bayesian approach, we could constrain the structure of the BLR in them as well as derive other properties of BLR.

Knowledge of the long term variability characteristics of AGN is very crucial in RM program. Ideal targets for such studies are AGN that are known

to show flux variability. For this purpose a dedicated telescope is needed to monitor large number of AGN/quasars over long duration of time. The 4 m International Liquid Mirror Telescope (ILMT) is expected to be commissioned soon on the Aryabhatta Research Institute of Observational Sciences (ARIES) in Devasthal, India. The ILMT, which will observe in the Time Delayed Integration (TDI) mode, will be repeatedly scanning the sky within a narrow stripe of width $\sim 27'$. In this thesis, we arrived at a catalogue of 6738 quasars that will be covered by ILMT. Observations from the ILMT in the future can enable one to select variable quasars from this new catalogue for RM programs. Also, the quasars presented in this catalogue can serve as astrometric calibrators to convert the ILMT observations in the pixel coordinate system to the world coordinate system (α, δ).

Contents

[1]The contents of this chapter are based on Mandal et al. (2021a) (MNRAS, under preparation)

[2]The contents of this chapter are published in Mandal et al. (2018, 2019, 2021c)
[3]The contents of this chapter are published in Mandal et al. (2021b)

[4]The contents of this chapter are based on Mandal et al. (2020)

List of Figures

List of Tables

Chapter 1

INTRODUCTION

Active Galactic Nuclei (AGN) are one of the most luminous objects in the universe that emit radiation covering the whole accessible bands of the electromagnetic spectrum, predominantly in X-ray, UV, and optical wavelengths (Lynden-Bell, 1969; Salpeter, 1964). It is now believed that the accretion of matter on to super massive black holes (SMBHs; $10^6 - 10^{10}$ $M_\odot$) located at the centers of galaxies, is mainly responsible for such high luminosity ($10^{42} - 10^{46}\,\mathrm{erg\,s^{-1}}$; Fabian, 1999). The SMBH is surrounded by an optically thick and geometrically thin accretion disk (Shakura & Sunyaev, 1973). Broad line region (BLR) that lies on scales of about ~ 0.01 pc (typical for the Seyfert category of AGN) from the accretion disk, produces the line emission due to photo-ionization of gas clouds by the UV-optical ionizing continuum from the accretion disk. According to the unified scheme of AGN, a putative torus that surrounds the BLR region is responsible for the different manifestations of the AGN (Type 1 and Type 2), when viewed at different orientations (Antonucci, 1993; Urry & Padovani, 1995). The inner radius of the torus can extend to $0.01 - 0.1$ pc, equivalent to $10 - 100$ light-days, for a typical UV luminosity of $10^{42} - 10^{46}\,\mathrm{erg\,s^{-1}}$ (Suganuma et al., 2006). So, different regions located at the central part of AGN are so compact that it is difficult to probe these regions using any current imaging techniques, except for a handful of the closest ones. A schematic representation of the different components of AGN is shown in Fig. 1.1.

Few interferometric observations are available that could probe the central regions of AGN via direct imaging. For example, Gravity Collaboration et al. (2018) observed 3C 273 using the GRAVITY instrument mounted on the 8 m Very Large Telescope (VLT) and found a mean BLR size of 145 ± 35 days using Paα line through interferometric technique. Recently, from high resolution radio observations using the Very Large Array, Carilli

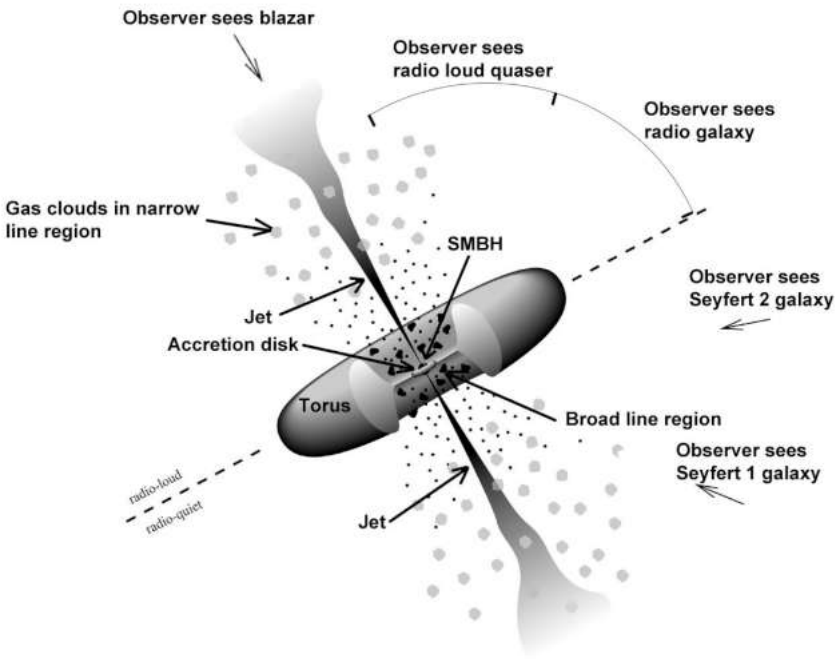

Figure 1.1: Unification scheme of AGN. Image courtesy: *Fermi* Gamma−ray Space Telescope.

et al. (2019) imaged the torus in a radio galaxy Cygnus A. They found an elongated structure, perpendicular to the radio jet and centered on the core, with a full length of about 528 pc and a full width of 286 pc. GRAVITY Collaboration et al. (2019) partially resolved the size and structure of hot dust torus using VLTI/GRAVITY and reported the increase of the physical radius with bolometric luminosity in eight Type 1 AGN. All these interferometric observations are limited by the brightness and compactness in terms of the sizes of the regions to resolve in these objects. But this kind of limitation is not with reverberation mapping (RM) or Echo mapping method that uses the variability characteristics of AGN and thus can be used to probe the central regions of AGN at comparatively higher redshifts.

BLR reverberation mapping is based on measuring the time delay (τ) between the UV/optical continuum from the accretion disk and the broad emission line produced in the BLR. The time delay (τ) can be measured

using traditional cross-correlation techniques (Peterson, 1993; Edelson & Krolik, 1988), which in principle gives the average radius of the BLR ($R_{BLR} = \tau/c$, where c is the velocity of light). The mass of the black hole (M_{BH}) in an AGN can be estimated from the measured R_{BLR} and the width of the broad emission line (ΔV), measurable from the spectrum using the relation

$$M_{BH} = f_{BLR}\left(\frac{\Delta V^2 R_{BLR}}{G}\right) \tag{1.1}$$

where G is the gravitational constant and f_{BLR} is the virial factor that depends on the geometry and kinematics of BLR. The method of RM has been applied to measure M_{BH} in more than 100 AGN with most of the measurements coming from the compilation[1] of Bentz & Katz (2015), the Sloan Digital Sky Survey Reverberation Measurement project (Grier et al., 2017b) and the Super-Eddington Accretion in Massive Black Holes project (Du et al., 2014, 2016, 2018; Wang et al., 2014). The f_{BLR} in Equation 1.1 can be calibrated considering the $M - \sigma_*$ relation that is applicable for both AGN and local quiescent galaxies (e.g., Onken et al., 2004; Woo et al., 2015), where σ_* represents the stellar velocity dispersion. However, it is not clear whether a constant f_{BLR} can be used to estimate M_{BH} for all AGN. Considering the complex geometry and kinematics of individual AGN, it is found that the virial factor depends on the bulge type of the host galaxy (Ho & Kim, 2014).

As of today, BLR reverberation is applied to measure the size of BLR in more than 100 AGN, which leads to a linear relation between R_{BLR} and the continuum luminosity at 5100 Å (Bentz & Katz, 2015; Grier et al., 2017b; Wang et al., 2014), in the luminosity range between $10^{42} - 10^{46}\,\mathrm{erg\,sec^{-1}}$. Most of the RM studies available in the literature are mainly focused on es-

[1] http://www.astro.gsu.edu/AGNmass/

timating BLR sizes and M_{BH}, which are driven by the quality of the available RM data, characterized by time resolution and signal-to-noise ratio (SNR). Using a direct RM approach it is difficult to constrain the geometry and kinematics of the emitting regions unless the transfer function can be recovered. However, it is in principle possible to calculate time delays as a function of velocity across the emission line profile and better constrain the geometry and kinematics of the gas in the BLR for sources with densely sampled and good SNR spectra (e.g., Ulrich & Horne, 1996; Bentz et al., 2010; Grier et al., 2013b; Xiao et al., 2018). Also, there are reports in the literature that model the RM data using Bayesian approach to constrain the geometry and dynamics of the BLR by estimating different AGN parameters, as well as, f_{BLR} for individual objects (Pancoast et al., 2011; Brewer et al., 2011; Pancoast et al., 2012, 2014; Li et al., 2018). In addition, Li et al. (2013) developed a geometrical modeling code, PBMAP (Parallel Bayesian code for reverberation−MAPping data) providing several parameters, e.g., BLR size, inclination angle (θ_{inc}), opening angle (θ_{opn}) including non-linear response of the line emission to the continuum and allow for detrending the light curves (Welsh, 1999; Denney et al., 2010; Li et al., 2013, 2019). They applied this technique to a sample of 40 objects using archival Hβ line and continuum light curves to recover velocity integrated transfer function considering a disk-like BLR structure emitting Hβ line. Such a flattened disk like BLR is also seen in the high resolution observations of 3C 273 with the VLT (Gravity Collaboration et al., 2018). Also, there are evidences of non-linear responses of the line fluxes to the continuum (Li et al., 2013), which were ignored in the previous RM studies. It is therefore important to extend this approach to a large number of AGN to examine differences, if any, in the geometry of the BLR between different AGN.

A putative torus, that obscures the central engine, is the dominant source of infrared (IR) radiation. This shows a bump in the IR region in the broad-band spectral energy distribution (SED) (Barvainis, 1987; Sanders et al., 1989; Kobayashi et al., 1993) in most of the AGN. A method analogous to the BLR reverberation mapping experiment is the dust reverberation mapping (DRM; Suganuma et al., 2006; Koshida et al., 2014; Mandal et al., 2018; Minezaki et al., 2019; Mandal et al., 2021c), which is based on the delayed response of the near infrared (NIR) radiation from the dust torus to changes in the UV/optical continuum emission from the accretion disk. From NIR interferometric observations it has been found that the dust torus size does not follow the known relation $\Delta t \propto L^{0.5}$ as found in reverberation mapping program (Koshida et al., 2014), instead the half light radius $R_{1/2}$, which is defined as the radius within which half of the total integrated light at a given wavelength is contained, varies as $R_{1/2} \propto L^{0.21}$ (Kishimoto et al., 2011b). More than three dozen AGN have been studied using DRM as of today to measure the inner radius of the dust torus (Koshida et al., 2014; Minezaki et al., 2019). Koshida et al. (2014) applied DRM on 17 Seyfert 1 galaxies and published 49 measurements of lag times between the K-band flux and that of the optical continuum in the V-band for those sources. Their study reveals a systematically smaller torus size measured from DRM compared to the interferometric radius in the K band. Minezaki et al. (2019) carried out a DRM survey of quasars at redshifts $z < 0.6$ and reported torus sizes for 22 targets. They found a strong correlation between the reverberation radius of the inner dust torus and the optical V-band luminosity with a slope of 0.424, which is smaller than the value 0.5, which is theoretically expected (Koshida et al., 2014).

Moreover, combining the dust inner angular size measured by optical interferometry, with the linear size measured by reverberation mapping, it

is possible to estimate direct distance, which could allow one to constrain cosmological models and prove the nature of dark energy if a dozen of objects could be observed by both techniques (Hönig et al., 2014). Both the emission line lag (Haas et al., 2011; Watson et al., 2011; Czerny et al., 2013) and dust reverberation lag (Oknyanskij et al., 1999; Oknyanskij & Horne, 2001; Hönig et al., 2014; Yoshii et al., 2014; Hönig et al., 2017) have been proposed to serve as standard candles. Unfortunately, there are only a few objects having dust lag measurements (Suganuma et al., 2006; Koshida et al., 2014; Pozo Nuñez et al., 2014), which motivated Hönig et al. (2017) to carry out a large DRM program, 'VEILS' (VISTA Extragalactic Infrared Legacy Survey) to use dust lag as standard candle for cosmology and constrain cosmological parameters from a survey of about 1350 Seyfert 1 galaxies in the redshift range $0.1 < z < 1.2$. They, however, missed the objects in the local universe, which are crucial in determining the normalization parameter of the AGN distance moduli (see Hönig et al., 2017). There are only about 20 AGN (Suganuma et al., 2006; Koshida et al., 2014; Mandal et al., 2018, 2021c) studied for DRM program in the local universe with redshift < 0.1. There is thus a need to increase the number of AGN with measured dust lags.

An important requirement of RM observations to determine the lag between different time series data is that the AGN need to be variable during the period of monitoring observations. Therefore, knowledge on the long term variability characteristics of AGN is very crucial and this will help one to preselect AGN for RM observations. To know the long term variability characteristics of AGN a dedicated telescope is needed to monitor a large number of AGN over a long duration of time. The 4 m International Liquid Mirror Telescope (ILMT), which will observe in the Time Delayed Integration (TDI) mode, is expected to be commissioned soon on

the Aryabhatta Research Institute of Observational Sciences (ARIES) site in Devasthal, India (Surdej et al., 2018). The ILMT, which will be repeatedly scanning the sky within a narrow stripe of width $\sim 27'$, can play an important role to study optical variability properties of AGN falling in the ILMT stripe. Moreover, quasars available in the ILMT stripe can also serve as astrometric calibrators to convert the ILMT observations in the pixel coordinate system to the world coordinate (α, δ) system. Such a catalogue of quasars in the ILMT stripe can be of use to study the optical flux and colour variability characteristics of AGN, which can also serve as a good data base to preselect quasars for RM programs.

Since the discovery of AGN, the progress in revealing the inner parts of AGN came with the advancement of observing facilities like telescopes, satellites, detectors as well as improvements in theoretical models. This thesis aims to probe the inner regions of AGN, which could pave the way for improved understanding of their central regions.

1.1 REVIEW OF LITERATURE

Because of the compactness of the central regions in AGN, it is difficult to probe those regions using any current direct imaging techniques except for a handful of nearby AGN using interferometric observations. One of the important characteristics of AGN is that they show flux variability over the entire electro-magnetic spectrum (Wagner & Witzel, 1995; Ulrich et al., 1997). This flux variability property of AGN can be used to probe the spatially unresolved inner regions in them. A method that relies on this flux variability property used to probe different emitting regions in the central part of AGN is the RM technique, first introduced by Blandford & McKee (1982). Since then, many observational and theoretical efforts were done to reveal the structure and kinematics of the central part of AGN using RM

(Ulrich & Horne, 1996; Bentz et al., 2010; Grier et al., 2013b; Xiao et al., 2018).

The various observational efforts that are devoted to probe the central regions of AGN fall under the following three categories.

1. **Program to find the extent of the BLR (and subsequently the black hole mass) via BLR reverberation mapping:** This is usually accomplished by spectroscopic monitoring observations. However, over the last few years, photometric monitoring observations through suitable selection of narrow band filters that could cover the emission line coming from the BLR and the continuum from the central region have been attempted as an alternative to spectroscopic monitoring observations. RM measurements of the size of the BLR are now available for more than 100 AGN, but this study is limited to sources that cover a small range of redshift and luminosity. Most of such measurements are from the compilation of Bentz & Katz (2015), the Sloan Digital Sky Survey Reverberation Measurement project carried out by Grier et al. (2017b) and the Super-Eddington Accretion in Massive Black Holes project by Wang et al. (2014); Du et al. (2016); Li et al. (2018) and Xiao et al. (2018).

2. **Program to find the extent of the dusty torus:** This is accomplished by photometric monitoring of AGN in the optical and NIR bands and then use the time delay between the optical and IR light curves to indirectly find the extent of the inner edge of the dusty torus. This has been carried out for about 40 objects. Recently, Lyu et al. (2019) using optical and mid infrared (MIR) observations reported results of the size of the torus for most of the Palomar-Green quasars and found the MIR time lags to follow the relation $\Delta t \propto L^{0.5}$. And for most of the objects

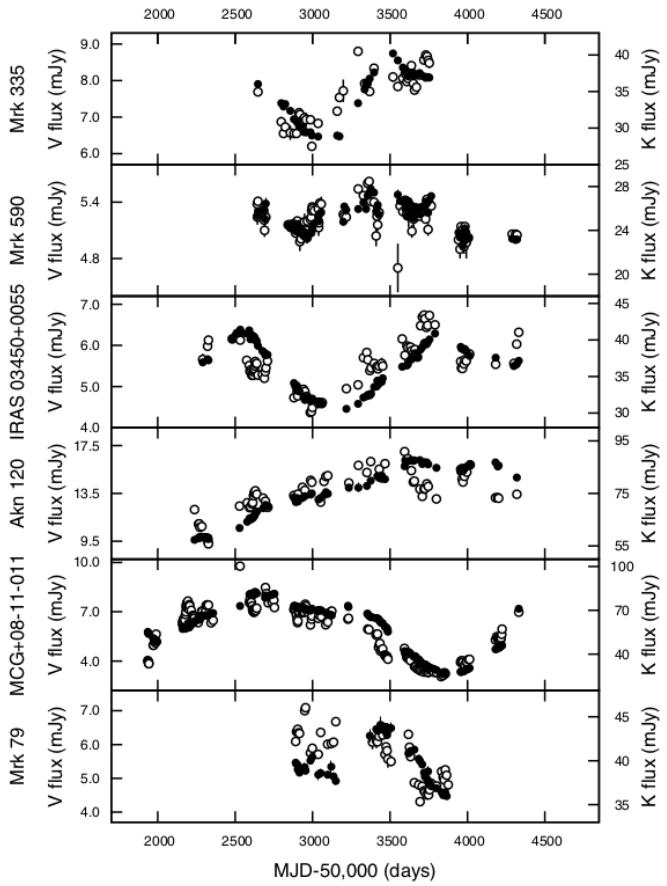

Figure 1.2: Light curves used in DRM study by Koshida et al. (2014).

for which dust torus size is available, the light curves used to find the lag are not well sampled in time (Koshida et al., 2014; Minezaki et al., 2019). An example of such light curves used by Koshida et al. (2014) is shown in Fig. 1.2.

3. **Direct imaging of the central region:** In addition to the above two indirect ways to find the extent of the different components in AGN, direct imaging observations too are now possible using sensitive instruments on the large optical/IR telescopes that are currently operational in the world. But this is limited to only a handful of very nearby and bright objects, made possible by interferometric techniques. The inner extent of the dust torus via interferometry is now known for about three dozen AGN (Kishimoto et al., 2009, 2011a; GRAVITY Collab-

oration et al., 2019; Gravity Collaboration et al., 2020). Moreover, by combining dust inner angular size measured by optical/IR interferometry with linear size measured by reverberation mapping it has been possible to estimate direct distance. This could allow one to constrain cosmological models and prove the nature of dark energy if a dozen objects spanning a wide range of redshifts could be observed by both the techniques (Hönig et al., 2014).

1.2 STATEMENT OF THE RESEARCH PROBLEM

From the brief overview of the current observational status on the indirect method of using RM to probe the central regions of AGN, it is evident that one needs to increase the number of sources with better RM based measurement of BLR size and dust torus size. Any progress in this direction is contingent upon carrying out good quality (time sampling and SNR) observations of more number of AGN. The key ideas that we aim to pursue in this thesis work are

1. How does the BLR size estimated from photometric monitoring observations compare with that obtained from spectroscopic reverberation mapping observations?

2. How do new measurements on the inner extent of the dust torus fit into the already existing dust lag v/s luminosity relation? This involves measurement of the torus size in more AGN.

3. From modeling of the observed light curves, one can infer the geometry and kinematics of the BLR. Based on modeling approach, how do the geometry and kinematics of BLR compare among different sources?

4. How many known quasars are there in the ILMT stripe? What is their usability as astrometric standards?

   These questions will be addressed in this thesis.

1.3 OBJECTIVES

Based on the key research problems stated above on RM studies of AGN, the main objectives of the thesis are as follows

1. Measurement of the size of the BLR using narrow band photometric monitoring and subsequently, black hole mass estimation from a single epoch spectrum.

2. Determination of the size and structure of dust torus in AGN through optical and NIR photometric monitoring.

3. Estimation of the size and structure of the BLR region using Bayesian statistics through the theoretical model.

4. Finding quasars in the ILMT stripe and their usability as astrometric calibrators.

1.4 OVERVIEW OF THE THESIS

The main motivation of the thesis is to find the mass of the black hole and the extent of the BLR and torus in AGN using the technique of RM. The details of this work will be presented as seven chapters in the thesis, as shown below.

1.4.1 Chapter 1: Introduction

This chapter starts with the basic introduction to AGN, gives a brief overview of the available methods to measure BLR and torus size, discusses the cur-

rent status in this field, the avenues for new research and ends with the motivation of the present thesis.

1.4.2 Chapter 2: Sample selection, Observations and Data reduction

This chapter gives the details of how the sample was selected for the thesis work and the observational strategy adopted. It gives details of the instruments that acquired data used in this thesis. The nature of the data and the various procedures followed to reduce the data are explained in detail in this chapter. In addition to that, the chapter also provides details of the models used to analyse the available RM data to estimate the size and structure of BLR region. It also details the cross-correlation analysis techniques used in this work to find the correlation between flux variations in different wave-bands.

1.4.3 Chapter 3: BLR reverberation on Mrk 590, a changing look AGN

This chapter presents the analysis carried out and results obtained on the source Mrk 590 using photometric reverberation observations.

1.4.4 Chapter 4: Dust reverberation on H0507+164 and Z229−15

This chapter presents the first time measurements on the inner edge of the dusty torus in two AGN namely, H0507+164 and Z229−15.

1.4.5 Chapter 5: Estimation of the size and structure of the broad line region using Bayesian statistics

The results on the structure of BLR obtained via a Markov Chain Monte Carlo approach are presented in this chapter.

1.4.6 Chapter 6: Quasars in the ILMT stripe

This chapter presents the selection of known quasars that will be covered by the ILMT in the future. In addition to that, it also presents the usability of such a catalogue.

1.4.7 Chapter 7: Summary and Future prospects

This last chapter compiles the outcome of the problems addressed in this thesis along with detailed discussions and conclusions. This chapter also details a few research problems that will be pursued in the future.

Chapter 2

SAMPLE SELECTION, OBSERVATIONS AND DATA REDUCTION

2.1 THE SAMPLE

1. **BLR reverberation:**

   Photometric monitoring of AGN has started to emerge as an alternative method to the conventional spectroscopic monitoring of AGN to find the extent of the BLR and obtain the BH mass using a single epoch spectrum. Such a program demands a careful selection of the target so that the continuum and line fall on the set of broad/narrow band filters available at any observing facility. For this objective, we have carefully selected the source Mrk 590 whose redshifted Hα line falls in the narrow filter centered at the S II region and the continuum falls on the broad B-band. This source is a changing look AGN at a redshift z = 0.0264.

2. **Dust Reverberation:**

   The size of the inner edge of dust torus is known for about three dozen AGN (Suganuma et al., 2006; Koshida et al., 2014; Minezaki et al., 2019; Mandal et al., 2018, 2021c). Most of these measurements are based on sparsely sampled optical and near-infrared observations. A possible reason for the paucity of such data could be due to the difficulty in scheduling observations in the optical and NIR bands, simultaneously. To increase the measurements of dust torus size in AGN, we have initiated a program called REMAP (REverberation Mapping of AGN Program) that uses the 2 m Himalayan Chandra Telescope (HCT). The initial sample of sources for monitoring under REMAP was selected as follows.

   (i) We used the sample of Bentz & Katz (2015) that provides RM of BLR for 60 sources. There are only a few sources that have the time

Table 2.1: Details of the initial list of objects selected for the REMAP monitoring.

No.	Object Name	RA (2000)	DEC (2000)	V (mag)	z	Type	M_{BH} ($\times 10^6 M_\odot$)	R_{BLR} (days)
1	H0507+164	05:10:45.5	+16:29:56	15.64	0.018	Seyfert 1.5	$9.62^{+0.33}_{-3.73}$	$3.01^{+0.42}_{-1.84}$
2	Z 229−15	19:05:25.9	+42:27:40	15.40	0.028	Seyfert 1	$10.00^{+1.90}_{-2.40}$	$3.86^{+0.69}_{-0.90}$
3	Mrk 142	10:25:31.3	+51:40:35	16.15	0.045	Seyfert 1	$2.17^{+0.77}_{-0.83}$	$2.74^{+0.73}_{-0.83}$
4	MCG+10-16-111	11:18:57.7	+58:03:24	16.71	0.028	Seyfert 1	$5.50^{+2.00}_{-1.80}$	$2.31^{+0.62}_{-0.49}$
5	Arp 151	11:25:36.2	+54:22:57	16.49	0.021	Seyfert 1	$6.41^{+0.92}_{-1.19}$	$3.99^{+0.49}_{-0.68}$
6	Mrk 1310	12:01:14.3	−03:40:41	15.91	0.019	Seyfert 1	$2.20^{+0.90}_{-0.90}$	$4.20^{+0.90}_{-0.10}$
7	Mrk 202	12:17:55.0	+58:39:35	16.41	0.021	Seyfert 1	$1.30^{+0.40}_{-0.40}$	$3.50^{+0.10}_{-0.10}$
8	NGC 5273	13:42:08.3	+35:39:15	13.12	0.003	Seyfert 1	$4.70^{+1.60}_{-1.60}$	$2.21^{+1.19}_{-1.60}$

lag measurements for both BLR and the torus and comparison of these measurements stipulate that the BLR size is about 4−5 times smaller than that of the torus (Koshida et al., 2014; Mandal et al., 2019).

(ii) We imposed the condition that the BLR lag should be within the range of 3 days to 10 days. This condition helps us to observe each source for dust lag once every five days, which sets the time resolution of our data. With this time resolution, it would be possible to obtain meaningful lag only for those sources that are expected to have dust lag more than 30 days or so and monitored for a duration of about 6 months.

(iii) We selected only those sources that are brighter than 16.5 magnitude in the V-band to get good SNR data within our allocated time and must have declination greater than −10 degree for the observability of sources from the Himalayan Chandra Telescope.

Based on the above selection criteria, we finally arrived at a sample of 8 sources for REMAP. The details of those sources are mentioned in Table 2.1. For this thesis work I only concentrated on the brightest two

sources in this sample, namely H0507+164 and Z229−15.

3. **Estimation of the size and structure of the BLR using Bayesian approach:**

   In order to estimate the black hole masses and study the accretion mechanisms in AGN it is important to understand the kinematics and geometry of the BLR. From high SNR spectra and using the technique of velocity resolved RM, it is possible to infer the geometry and kinematics of the BLR. However, such observations are available for only limited AGN. An alternative to this approach is to use conventional RM data in a theoretical formalism to get the geometry and kinematics of BLR. To infer the geometry and kinematics of a large sample of AGN via modeling of their emission and continuum light curves using a Markov Chain Monte Carlo method based on Bayesian statistics, we used the PBMAP (Parallel Bayesian code for reverberation−MAPping data) code. Firstly, we retrieved data from the literature for all objects that are in the black hole mass database by Bentz & Katz (2015) and the SDSS−RM program (Shen et al., 2016; Grier et al., 2017b) and imposed two additional constraints (i) the sources must have the continuum and line light curves which can be either of Mg II, Hβ or Hα and (ii) there are no previous investigations of the BLR structure for the objects. Based on the above two criteria we arrived at a sample of 57 objects. Among these 57 objects, 22 have data for both Hβ and Hα lines, 3 have data for both Hβ and Mg II lines, 25 have only Hβ , 4 have only Hα, whereas 3 have light curve data for only Mg II line. All these amount to a total of 82 independent measurements. The light curve data for these objects were retrieved from Shen et al. (2016), Grier et al. (2017b), Wang et al. (2014), Grier et al. (2012), Bentz et al.

Table 2.2: Details of the objects used in the modeling work. Here τ_{cent} is in days, FWHM and σ are in km s^{-1} and logL_{5100} is in erg s^{-1}.

No.	α_{2000}	δ_{2000}	Type	z	line	τ_{cent}	FWHM	σ	logL_{5100}	Reference
1	00:10:31.01	+10:58:29.5	Sy1	0.090	Hβ	$12.6^{+3.9}_{-3.9}$	5054 ± 145	3321 ± 107	44.320 ± 0.050	D
2	02:30:05.52	-08:59:53.2	Sy1	0.016	Hβ	$4.8^{+7.4}_{-3.7}$	-	-	42.950 ± 0.050	C
3	06:52:12.32	+74:25:37.2	Sy1	0.019	Hβ	$10.1^{+1.1}_{-1.1}$	9744 ± 3700	3714 ± 68	43.75 ± 0.060	D
4	11:39:13.92	+33:55:51.1	Sy1	0.033	Hβ	$12.5^{+0.5}_{-11.5}$, $23.3^{+7.5}_{-5.8}$	-	-	43.700 ± 0.060	G, C
5	12:42:10.61	+33:17:02.7	Sy1	0.044	Hβ	$11.4^{+2.9}_{-1.9}$	-	-	43.590 ± 0.040	H
6	13:42:08.39	+35:39:15.3	Sy1	0.003	Hβ	$2.22^{+1.19}_{-1.61}$	4615 ± 330	1544 ± 98	41.534 ± 0.144	E
					Hα	$2.06^{+1.42}_{-1.31}$	-	-	41.534 ± 0.144	E
7	14:05:18.02	+53:15:30.0	QSO	0.467	Hβ	$41.6^{+14.8}_{-8.3}$	3131 ± 44	1232 ± 16	44.300 ± 0.001	B
					Hα	-	-	-	44.300 ± 0.001	B
8	14:05:51.99	+53:38:52.1	QSO	0.455	Hα	$53.0^{+8.7}_{-5.7}$	3489 ± 84	1590 ± 24	43.900 ± 0.002	B
9	14:07:59.07	+53:47:59.8	Sy1	0.173	Hβ	$19.2^{+4.3}_{-12.8}$	5115 ± 59	1790 ± 10	43.541 ± 0.001	A
10	14:08:12.09	+53:53:03.3	Sy1	0.116	Hβ	$10.5^{+1.0}_{-2.2}$	3111 ± 36	1409 ± 11	43.120 ± 0.001	B
					Hα	$8.3^{+4.9}_{-6.3}$	2794 ± 15	1185 ± 7	43.120 ± 0.001	B
11	14:09:04.43	+54:03:44.2	QSO	0.658	Hβ	$11.6^{+8.6}_{-4.6}$	12673 ± 455	5284 ± 54	44.120 ± 0.003	B
12	14:09:15.70	+53:27:21.8	Sy1	0.258	Hα	$42.1^{+2.7}_{-2.1}$	6279 ± 20	3232 ± 40	43.300 ± 0.002	B
13	14:10:04.27	+52:31:41.0	QSO	0.527	Hβ	$53.5^{+4.2}_{-4.0}$	3172 ± 85	2126 ± 35	44.190 ± 0.001	B
					Hα	-	-	-	44.190 ± 0.001	B
14	14:10:18.04	+53:29:37.5	QSO	0.470	Mg II	$32.3^{+12.9}_{-5.3}$	-	-		A
					Hβ	$16.2^{+2.9}_{-4.5}$	2377 ± 288	1781 ± 38	43.550 ± 0.003	B
					Hα	$22.1^{+7.7}_{-7.3}$	2103 ± 365	1738 ± 31	43.550 ± 0.003	B
15	14:10:31.33	+52:15:33.8	Sy2	0.608	Hβ	$35.8^{+1.1}_{-10.3}$	2578 ± 112	1619 ± 38	43.990 ± 0.002	B
16	14:10:41.25	+53:18:49.0	QSO	0.359	Hβ	$21.9^{+4.2}_{-2.4}$	4183 ± 51	1909 ± 12	43.790 ± 0.001	B
					Hα	$21.0^{+1.4}_{-2.8}$	3642 ± 26	1318 ± 11	43.790 ± 0.001	B
17	14:11:12.72	+53:45:07.1	QSO	0.587	Hβ	$18.6^{+7.1}_{-3.8}$	2089 ± 77	1221 ± 36	44.092 ± 0.002	A
18	14:11:15.19	+51:52:09.0	QSO	0.572	Hβ	$49.1^{+11.1}_{-2.0}$	3234 ± 164	1423 ± 32	44.280 ± 0.001	B
					Hα	-	-	-	44.280 ± 0.001	B
19	14:11:23.42	+52:13:31.7	Sy1	0.472	Hβ	$13.0^{+1.4}_{-0.8}$	4123 ± 40	1443 ± 11	44.100 ± 0.001	B
					Hα	$22.6^{+0.6}_{-1.5}$	3483 ± 44	1346 ± 13	44.100 ± 0.001	B
20	14:11:35.89	+51:50:04.5	QSO	0.650	Hβ	$17.6^{+8.6}_{-7.4}$	3422 ± 491	1527 ± 22	44.010 ± 0.003	B
21	14:12:14.20	+53:25:46.7	QSO	0.458	Mg II	$36.7^{+10.4}_{-4.8}$	-	-		A
22	14:12:53.92	+54:00:14.4	Sy1	0.187	Hβ	$21.5^{+5.8}_{-7.7}$	5120 ± 130	1758 ± 22	42.972 ± 0.003	A
23	14:13:14.97	+53:01:39.4	QSO	1.026	Hβ	$43.9^{+4.9}_{-4.3}$	11002 ± 1743	6543 ± 34	44.500 ± 0.038	B
24	14:13:18.96	+54:32:02.4	QSO	0.362	Hβ	$20.0^{+1.1}_{-3.0}$	2730 ± 137	1353 ± 23	43.910 ± 0.001	B

No.	α_{2000}	δ_{2000}	Type	z	line	τ_{cent}	FWHM	σ	L_{5100}	Reference
25	14:13:24.28	+53:05:27.0	QSO	0.456	Hβ	$25.5^{+10.9}_{-5.8}$	7758 ± 77	6101 ± 48	43.910 ± 0.002	B
					Hα	$56.6^{+7.3}_{-15.1}$	5604 ± 31	4569 ± 51	43.910 ± 0.002	B
26	14:14:17.13	+51:57:22.6	QSO	0.604	Mg II	$29.1^{+3.6}_{-8.8}$	-	-		A
					Hβ	$15.6^{+3.2}_{-5.1}$	7451 ± 221	2788 ± 48	43.370 ± 0.012	B
27	14:15:32.36	+52:49:05.9	Sy1	0.715	Hβ	$26.5^{+9.9}_{-8.8}$	1626 ± 243	857 ± 32	44.110 ± 0.003	B
28	14:16:25.71	+53:54:38.5	Sy1	0.263	Hβ	$21.9^{+7.9}_{-10.4}$	3752 ± 93	1636 ± 11	43.929 ± 0.018	A
					Hα	$32.2^{+15.6}_{-12.6}$	2632 ± 28	1298 ± 8	43.929 ± 0.018	B
29	14:16:44.17	+53:25:56.1	QSO	0.425	Mg II	$17.2^{+2.7}_{-2.7}$	-	-		A
30	14:16:45.15	+54:25:40.8	QSO	0.244	Hβ	$10.9^{+20.9}_{-6.6}$	4981 ± 97	1902 ± 20	43.178 ± 0.002	A
					Hα	$10.6^{+2.3}_{-2.4}$	6027 ± 19	3927 ± 30	43.178 ± 0.002	B
31	14:16:45.58	+53:44:46.8	Sy1	0.442	Hβ	$23.3^{+2.7}_{-11.2}$	1854 ± 70	990 ± 19	43.646 ± 0.008	A
					Hα	$16.7^{+4.1}_{-5.5}$	1575 ± 60	796 ± 23	43.646 ± 0.008	B
32	14:16:50.93	+53:51:57.0	QSO	0.527	Mg II	$25.1^{+2.0}_{-2.6}$	-	-		A
33	14:17:06.68	+51:43:40.1	Sy1	0.532	Hβ	$14.1^{+12.9}_{-9.5}$	1661 ± 104	743 ± 24	44.155 ± 0.001	A
34	14:17:12.30	+51:56:45.5	Sy1	0.554	Hβ	$12.5^{+1.8}_{-2.6}$	17614 ± 153	9475 ± 33	43.180 ± 0.012	B
					Hα	-	-	-	43.180 ± 0.012	B
35	14:17:24.59	+52:30:24.9	Sy1	0.482	Hβ	$10.1^{+12.5}_{-2.7}$	4930 ± 163	2036 ± 39	43.960 ± 0.002	B
					Hα	-	-	-	43.960 ± 0.002	B
36	14:17:29.27	+53:18:26.5	QSO	0.237	Hβ	$5.5^{+5.7}_{-2.1}$	9448 ± 367	6318 ± 38	43.260 ± 0.002	B
					Hα	$45.0^{+23.7}_{-3.9}$	8898 ± 66	5157 ± 40	43.260 ± 0.002	B
37	14:17:51.14	+52:23:11.1	QSO	0.281	Hα	$10.1^{+2.4}_{-1.9}$	7868 ± 66	3384 ± 71	42.700 ± 0.007	B
38	14:18:56.19	+53:58:45.0	QSO	0.976	Hβ	$15.8^{+6.0}_{-1.9}$	7156 ± 61	7568 ± 70	45.350 ± 0.002	B
39	14:19:23.37	+54:22:01.7	Sy1	0.152	Hβ	$11.8^{+0.7}_{-1.5}$	2709 ± 55	1205 ± 9	43.090 ± 0.001	B
					Hα	$80.2^{+4.9}_{-6.3}$	2643 ± 23	1018 ± 7	43.090 ± 0.001	B
40	14:19:41.11	+53:36:49.6	QSO	0.646	Hβ	$30.4^{+3.9}_{-8.3}$	2553 ± 136	1232 ± 30	44.490 ± 0.017	B
41	14:19:52.23	+53:13:40.9	QSO	0.884	Hβ	$32.9^{+5.6}_{-5.1}$	21468 ± 2120	7681 ± 64	44.220 ± 0.006	B
42	14:19:55.62	+53:40:07.2	QSO	0.418	Hβ	$10.7^{+5.6}_{-4.4}$	5136 ± 226	2291 ± 33	43.360 ± 0.003	B
					Hα	-	-	-	43.360 ± 0.003	B
43	14:20:10.25	+52:40:29.6	QSO	0.548	Hβ	$12.8^{+5.7}_{-4.5}$	10477 ± 114	6259 ± 23	44.060 ± 0.001	B
					Hα	$32.22^{+7.75}_{-11.55}$*	-	-	44.060 ± 0.001	B
44	14:20:23.88	+53:16:05.1	QSO	0.734	Hβ	$8.5^{+3.2}_{-3.9}$	11017 ± 109	7165 ± 36	44.190 ± 0.005	B
45	14:20:38.52	+53:24:16.5	QSO	0.265	Hβ	$29.6^{+2.5}_{-15.7}$	2975 ± 64	1362 ± 33	43.424 ± 0.001	A
					Hα	$20.2^{+10.5}_{-9.3}$	2808 ± 41	1320 ± 17	43.424 ± 0.001	B
46	14:20:39.80	+52:03:59.7	QSO	0.474	Hβ	$14.2^{+6.5}_{-8.1}$, $20.7^{+0.9}_{-3.0}$	3696 ± 55	1360 ± 20	44.109 ± 0.001	A, B
					Hα	$24.2^{+10.2}_{-5.3}$	3118 ± 80	1352 ± 24	44.109 ± 0.001	B
47	14:20:43.53	+52:36:11.4	QSO	0.337	Hα	$5.7^{+0.5}_{-0.5}$	2971 ± 114	1372 ± 40	43.370 ± 0.002	B
48	14:20:49.28	+52:10:53.3	QSO	0.751	Mg II	$34.0^{+6.7}_{-12.0}$	-	-		A
					Hβ	$46.0^{+9.5}_{-9.5}$	7625 ± 136	5013 ± 49	44.420 ± 0.002	B

No.	α_{2000}	δ_{2000}	Type	z	line	τ_{cent}	FWHM	σ	L_{5100}	Reference
49	14:20:52.44	+52:56:22.4	QSO	0.676	Hβ	$11.9^{+1.3}_{-1.0}$	13483 ± 141	7195 ± 40	45.030 ± 0.001	B
50	14:21:03.53	+51:58:19.5	Sy1	0.263	Hβ	$75.2^{+3.2}_{-3.3}$	3340 ± 82	1089 ± 22	43.600 ± 0.018	B
					Hα	-	-	-	43.600 ± 0.018	B
51	14:21:12.29	+52:41:47.3	QSO	0.843	Hβ	$14.2^{+3.7}_{-3.0}$	10839 ± 153	3658 ± 56	44.290 ± 0.008	B
52	14:21:35.90	+52:31:38.9	Sy1	0.249	Hβ	$3.9^{+0.9}_{-0.9}$	2078 ± 35	1026 ± 14	43.440 ± 0.001	B
					Hα	$5.9^{+1.6}_{-1.0}$	2142 ± 11	907 ± 6	43.440 ± 0.001	B
53	14:24:17.22	+53:02:08.9	QSO	0.890	Hβ	$36.3^{+4.5}_{-5.5}$	2752 ± 90	1252 ± 11	44.060 ± 0.060	B
54	15:36:38.40	+54:33:33.2	Sy1	0.039	Hβ	$20.0^{+8.7}_{-3.2}$	-	-	43.59 ± 0.030	C
55	15:59:09.62	+35:01:47.6	Sy1	0.031	Hβ	$12.2^{+3.5}_{-16.7}$	-	-	43.000 ± 0.060	C
56	17:19:14.49	+48:58:49.4	Sy1	0.024	Hβ	$20.61^{+54.33}_{-18.71}$	-	-	42.460 ± 0.140	I
57	23:03:15.67	+08:52:25.3	Sy1	0.016	Hβ	$10.8^{+3.4}_{-1.3}$	-	-	43.330 ± 0.030	F

A:Shen et al. (2016), B:Grier et al. (2017b), C:Wang et al. (2014), D:Grier et al. (2012), E:Bentz et al. (2014), F:Peterson et al. (2014), G:Rafter et al. (2013), H:Du et al. (2014), I: Shapovalova et al. (2013). *lag derived from ICCF analysis (see section 5.3).

Note: Col. (1): Number. Col. (2): RA. Col. (3): Dec. Col. (4): Type of the object. Col. (5): Redshift. Col. (6): Emission line. Col. (7): Centroid lag obtained from CCF analysis retrieved from literature. Col. (8): FWHM. Col. (9): Line dispersion. Col. (10): Optical luminosity at 5100 Å corrected for host-galaxy contribution. Col. (11): Reference.

(2014), Peterson et al. (2014), Rafter et al. (2013), Du et al. (2014) and Shapovalova et al. (2013). The continuum light curves of the objects taken from Shen et al. (2016) are measured at 5100 Å, whereas for the objects from Grier et al. (2017b), the continuum light curves are obtained from the photometric monitoring observations done in g and i bands. The details of the objects are given in Table 2.2.

4. **The ILMT quasar (IQ) catalogue**

To select all known quasars that are available in the ILMT stripe and their subsequent use for the calibration of ILMT observations, we looked at the suitability of all quasar catalogues that are available in the literature. One such quasar catalogue suited for our purpose is the Million Quasars (Milliquas) catalogue by Flesch (2017), the largest compilation of quasars available as of today. This catalogue contains about 1998464 quasars taken from different quasar surveys. The majority of quasars in the Milliquas catalogue are from the The Sloan Digital Sky Survey (SDSS), one of the ambitious sky surveys covering more than a quarter of the sky in the northern hemisphere in five optical filters. Other quasars included in Milliquas come from the NBCKDE, NBCKDE-v3 (Richards et al., 2009, 2015), XDQSO (Bovy et al., 2011; Myers et al., 2015), All-WISE and Peters photometric quasar catalogues (Peters et al., 2015), as well as quasars from all-sky radio/X-ray surveys. The Milliquas catalogue is a compilation of quasars from different surveys with varied uncertainties in the equatorial coordinates. But one needs to have quasars with precise positions with uncertainties to carry out astrometric calibration. The only source that provides precise positions in equatorial coordinates of celestial sources is the survey being presently carried out by the

European Space Agency *Gaia* mission. *Gaia*-DR2 (Lindegren et al., 2012; Gaia Collaboration et al., 2018) contains data from the all sky astrometric and photometric survey conducted by *Gaia* and provides accurate positions for about 1.7 billion sources, with proper motion (PM) and parallax measurements for about 1.3 billion sources (Marrese et al., 2019). Therefore, we used the precise and homogeneous measurements from *Gaia*-DR2 to get accurate positions for the quasars in the Milliquas catalogue.

2.2 OBSERVATIONS

1. BLR Reverberation

We monitored Mrk 590, a changing-look AGN to find the black hole mass. The photometric observations of Mrk 590 were carried out in the broad band B and R filters and in the narrow band Hα and S II filters over 115, 90, 86 and 83 epochs, respectively, during July, 2018 to December, 2018 using the Prompt 8, a 60 cm robotic telescope from Skynet[1]. The telescope is located at the Cerro Tololo Inter American Observatory having a focal length of 4200 mm and an f-ratio of 6.9. A 2048 $\times$ 2048 (15 μm pixels) CCD was used for observation covering a total FoV of 25.1 $\times$ 25.1 arcmin^2. The redshifted Hα line falls in the narrow S II and broad R bands, whereas B-band contains the continuum flux from the accretion disk. The average readout noise and gain of the CCD used in the observations are 10.21 electrons and 2.2 electrons/ADU, respectively. The average exposure time in B, R, Hα and S II bands are about 240 s, 240 s, 900 s and 900 s, respectively. One spectrum of the source was also obtained using the 8.2 m Subaru tele-

[1] https://skynet.unc.edu/telescopes/view?id=23

scope, Hawaii, operated by the National Astronomical Observatory of Japan using the High Dispersion Spectrograph[2] (Noguchi et al., 2002).

2. **Dust Reverberation**

As part of the REMAP project (Mandal et al., 2018, 2019), the two sources studied in this thesis, namely H0507+164 and Z229−15 were monitored using the 2 m HCT, operated by the Indian Institute of Astrophysics, Bengaluru. The telescope is a Ritchey−Chretien system with an f/9 beam. The optical observations were carried out using the Himalayan Faint Object Spectrograph and Camera (HFOSC) mounted at the Cassegrain focus and equipped with a 2K $\times$ 4K SiTe CCD system. Readout noise and gain of the CCD are 4.8 electrons and 1.22 electrons/ADU, respectively. The observations were carried out in binned mode using only the central 2K $\times$ 2K region of the CCD. The pixel scale of the CCD in this mode is $\sim$ 0.3 arcsec with a FoV of 10 $\times$ 10 arcmin^2. The NIR observations were performed subsequently to the optical observations at each epoch using the TIFR Near Infrared Spectrometer (TIRSPEC) mounted on one of the side ports of HCT (Ninan et al., 2014). The CCD used in TIRSPEC is a 1024 $\times$ 1024 HgCdTe array with a pixel size of 18 μm covering a field of view of 5 $\times$ 5 arcmin^2. The CCD has a readout noise of 25 electrons and gain of 6 electrons/ADU. The NIR observations were carried out in dithered mode each consisting of five exposures of 20 s at three dither positions for each of the three NIR filters, namely J, H, and K_s. To generate master sky frame, apart from the science frames, sky regions were also observed in the same dithering pattern as the object.

For H0507+164, we could observe for a total of 35 epochs during the

[2] https://www.subarutelescope.org/Observing/Instruments/HDS/

period October 2016 to April 2017 in the optical V-band and NIR J, H and K_s bands. Similarly, for Z229−15, observations in the optical B and V bands and in the NIR J, H and K_s bands were carried out for a total of 48 epochs during the period July 2017 to December 2018.

2.3 DATA REDUCTION

We used IRAF [3] (Image Reduction and Analysis Facility) and MIDAS [4] (Munich Data Analysis System) to reduce the acquired data. Two of the three objects monitored in this thesis have prominent host galaxy contribution to the AGN flux in the observed images. The host galaxy contribution was removed to get the AGN flux by modeling the underlying galaxy-starlight using GALFIT, a computer code that uses a model-fitting approach to 2-D image decomposition, developed by Peng et al. (2002). We also used Python programming language in various steps of data reduction whenever required. The details of the procedure adopted to reduce the data for the different objects are discussed below.

2.3.1 Mrk 590

Spectroscopy

We obtained a single epoch optical spectrum of Mrk 590 using the 8.2 m Subaru telescope. The photometric observations were carried out in the broad band B and R filters and in the narrow band Hα and S II filters. The spectroscopic and photometric observations of Mrk 590 were reduced using the standard procedures available in IRAF.

The reduced spectrum was first corrected for Galactic extinction using the

[3] IRAF is operated by the Association of Universities for Research in Astronomy, Inc., under cooperative agreement with the National Science Foundation

[4] MIDAS is the trade-mark of the European Southern Observatory

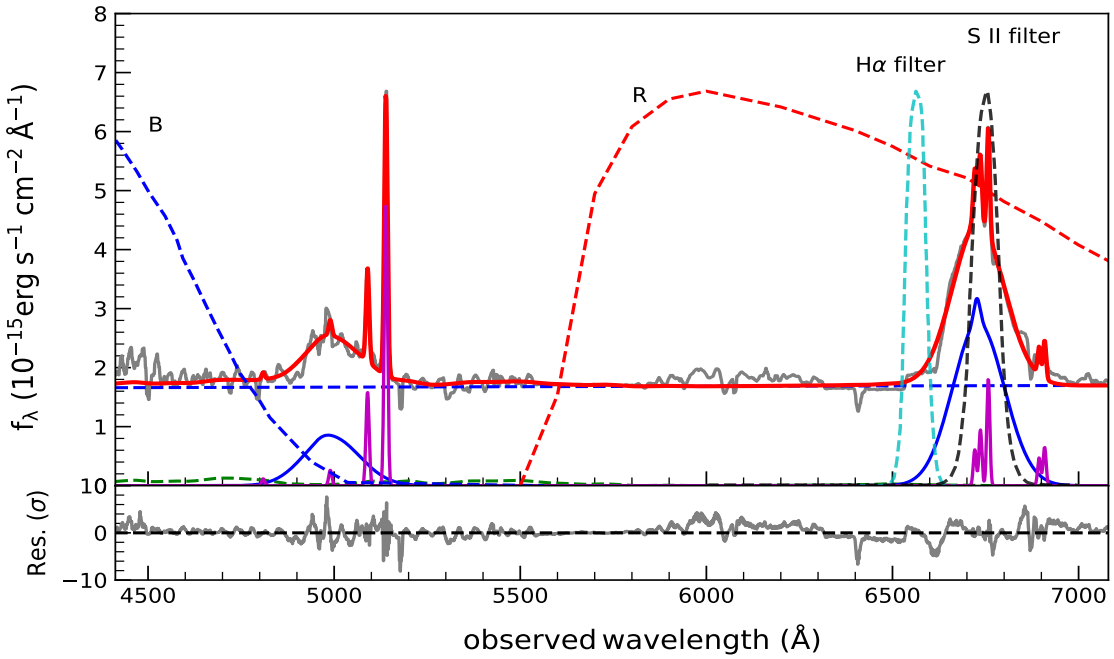

Figure 2.1: Spectrum of Mrk 590. Top panel: The observed data (grey), best-fit model (red) and decomposed power-law continuum model (black dashed), broad line (blue), and narrow line (magenta) are shown. The broad band B and R and narrow-band Hα and S II filters are over-plotted. Lower panel: Difference between the observed spectrum and the fitted spectrum.

Table 2.3: Spectral properties of Mrk 590. Columns are (1-2) FWHM and luminosity of Hβ broad component, (3-4) FWHM and luminosity of [O III]λ5007, (5-6) FWHM and luminosity of Hα broad component, (7) luminosity of Hα narrow component, and (8) luminosity at 5100Å. The units of FWHM and luminosity are km s^{-1} and erg s^{-1}, respectively. Line widths are not corrected for instrumental resolution.

FWHM(Hβ)	log L(Hβ)	FWHM([O III])	log L([O III])	FWHM(Hα)	log L (Hα)	log L(Hα_n)	λL_λ(5100)
(1)	(2)	(3)	(4)	(5)	(6)	(7)	(8)
10390 ± 1718	41.38 ± 0.01	592 ± 7	40.88 ± 0.01	6478 ± 240	41.86 ± 0.01	40.13 ± 0.08	43.12 ± 0.01

Schlegel et al. (1998) map and the Milky Way extinction law of Fitzpatrick (1999) with $R_V = 3.1$ and then moved to the rest-frame to measure the emission line parameters. We estimated the emission line parameters by performing a multi-component modeling. We first modeled the continuum, masking prominent emission lines, using the combination of a power-law ($f_\lambda \propto \lambda^\alpha$) and an Fe II template from Boroson & Green (1992) accounting for the Fe II emission in AGN. The Hα and Hβ complexes of the best-fit continuum subtracted spectrum, were modeled using multiple Gaussians (e.g., Rakshit et al., 2020). We used three Gaussians to model the broad lines and single Gaussian for the narrow lines. The reduced spectrum along with the best fitted models are given in Fig. 2.1. The deduced parameters are given in Table 2.3.

The broad band B-filter effectively contains AGN continuum because of the negligible contribution of the higher order Balmer lines. The broad R-band contains the redshifted Hα line and the continuum flux from the accretion disk. The redshifted Hα line falls in the narrow S II band (see Figure 2.1), containing at least 92% of the Hα line flux. The total narrow components contribution in the Hα line flux is found to be only $\sim 6\%$, which clearly demonstrates that the narrow S II band is mostly dominated by the response of the emission line clouds. Whereas, the narrow Hα band traces the AGN continuum underneath the Hα emission line. Therefore, the pure emission line flux can be estimated by removing the narrow band Hα flux from the narrow band S II flux. However, continuum subtraction from the observed R-band flux is a difficult task considering the larger accretion disk contribution compared to the narrow S II band.

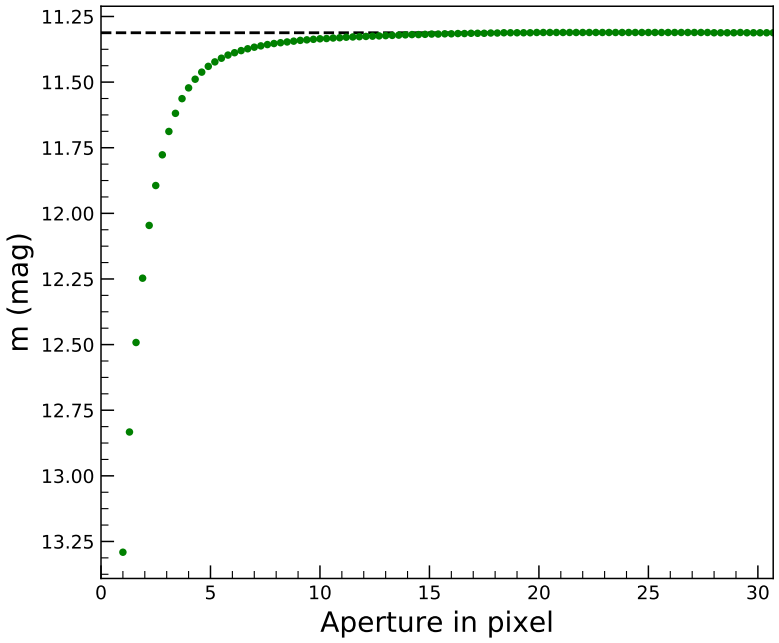

Figure 2.2: Curve of growth curve for a comparison star in S II-band. The dashed black line represents the best fit line to the points with aperture sizes more than 5 times the FWHM.

Photometry

The photometric data were reduced following the standard procedures for image reduction, such as bias and dark subtraction and flat-fielding.

We adopted the curve of growth (COG) method for aperture photometry of data from broad B and R and narrow Hα and S II-bands. We used the *daofind* task of IRAF to detect the objects in the observed images. We obtained instrumental magnitudes in several concentric apertures centered on the point source for a few comparison stars with the best SNR present in the same FoV of the target source using the *phot* task in IRAF. We obtained the COG by plotting the instrumental magnitude within each aperture as a function of aperture size, as shown in Fig. 2.2. The COG increases with aperture till the aperture is large enough to encompass most of the signal and becomes linear thereafter. Based on the method of least squares, we

fit a linear line (dashed black line in Fig. 2.2) to the portion of the growth curve with apertures between 4 and 6 times the FWHM of the comparison stars. The intercept of the fitted line is considered as the desired instrumental magnitude that corresponds to a particular optimum aperture. We applied this method to get the instrumental magnitudes of the target and the comparison stars present in the CCD frames for each epoch of observation in B, R, Hα and S II bands.

Flux Calibration

The instrumental magnitudes obtained in B, R, Hα and S II bands from aperture photometry based on COG were then converted into fluxes. This was carried out using the following steps

1. We collected the apparent magnitudes in u and g bands from the SDSS database for the comparison stars with the best SNR in the observed field of Mrk 590. We obtained the apparent B-band magnitudes of those comparison stars using the SDSS u and g magnitudes as [5]

$$B = u - 0.8116(u - g) + 0.1313 \tag{2.1}$$

   Using differential photometry, we then obtained the apparent B-band magnitudes of the target source. We collected the R-band standard magnitudes of the comparison stars from Zacharias et al. (2017) and subsequently, obtained the R-band apparent magnitudes. The apparent magnitudes thus obtained, were converted to B and R-band fluxes using the conversion factor given in Bessell et al. (1998).

[5] https://www.sdss.org/dr12/algorithms/sdssUBVRITransform/#Lupton2005

2. The narrow Hα and S II filters have mean wavelengths of 6563 Å and 6719 Å (Andjelić et al., 2011), respectively. The SDSS r-band ranges from 5380 Å to 7230 Å with the central wavelength at 6166 Å. So, both the narrow Hα and S II bands completely lie within the SDSS r-band. Therefore, we retrieved the r-band apparent magnitudes of the comparison stars from the SDSS database and obtained the Hα and S II-band apparent magnitudes of the target source with respect to the comparison stars using differential photometry. To convert the apparent magnitudes to fluxes, we used the SDSS r-band conversion factor [6].

   The apparent magnitudes were corrected for Galactic extinction taken from the NASA/IPAC Extragalactic data base (NED)[7] for the broad B and R bands and for the narrow Hα and S II bands, Galactic extinction in r-band was used.

Correction for the host-galaxy contribution

The observed S II-band image of Mrk 590 is shown in Fig. 2.3 (left), which clearly shows a prominent host galaxy. This is also conspicuous in the observations acquired in B and Hα bands. The host galaxy contribution therefore needs to be removed to get the true AGN flux. We used the two dimensional image-decomposition program GALFIT developed by Peng et al. (2002) to the observed B, R, Hα and S II-band images to estimate the host-galaxy contribution. We stacked 10 frames of different epochs with good seeing condition spanning the whole duration of our monitoring period to get a single image with high SNR for each of the four bands separately. GALFIT was then applied on the combined images.

[6] https://www.sdss.org/dr12/algorithms/fluxcal/

[7] http://nedwww.ipac.caltech.edu

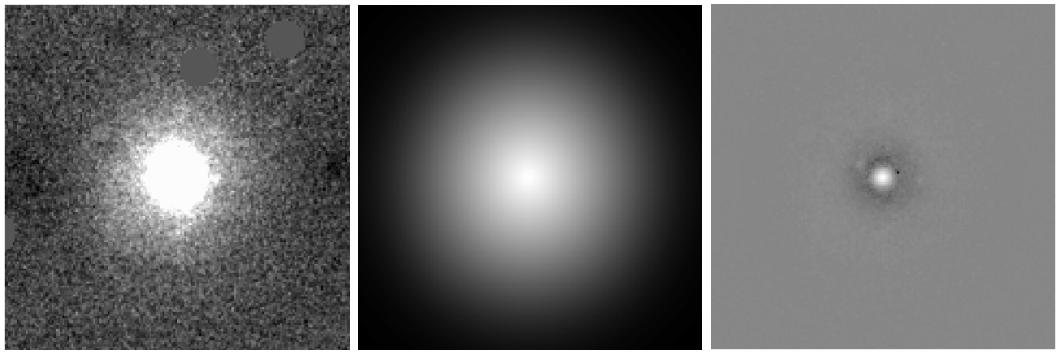

Figure 2.3: Observed S II-band image of Mrk 590 (left), the modeled galaxy image (middle) and the residual image containing the AGN at the center (right) obtained from GALFIT. The modeled and residual images are shown in logarithmic scale.

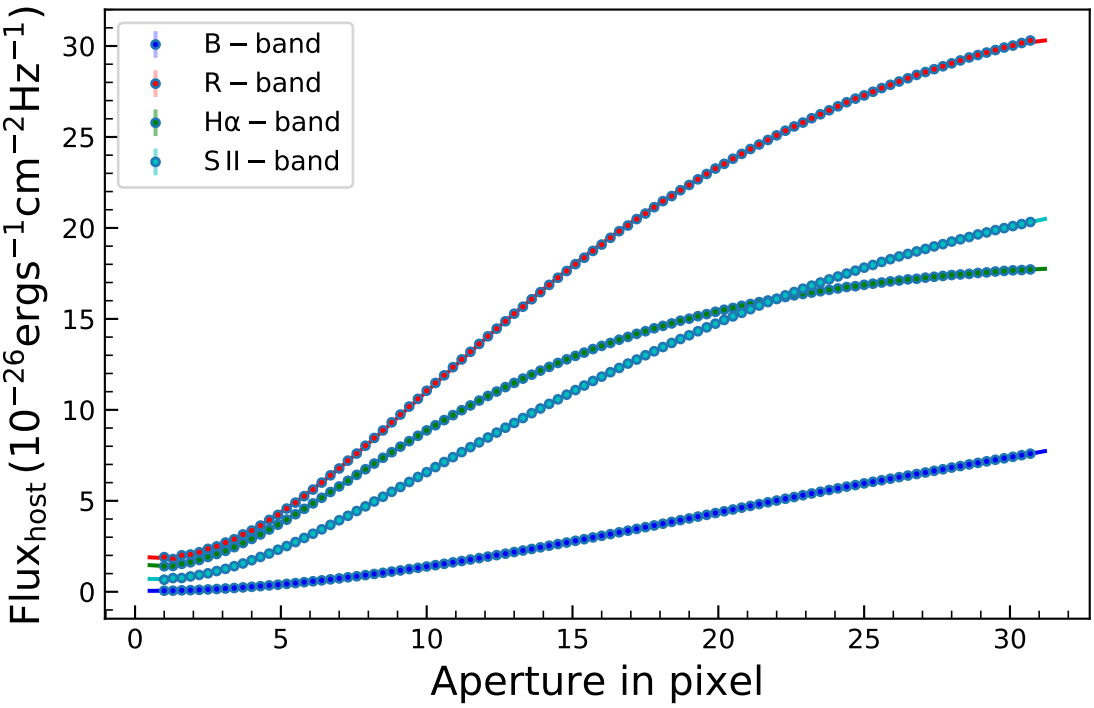

Figure 2.4: Host-galaxy flux as a function of aperture size in pixels. The points with error bars represent the galaxy-flux values and the solid lines are the best fit polynomials. The original B-band fluxes are multiplied by 10 for the purpose of presentation.

By modeling Mrk 590 using GALFIT, Kim et al. (2017) found that the host galaxy has a pseudo bulge with Sérsic index n = 1.04 and a disk. An exponential disk profile is nothing but simply a Sérsic profile with an index of n = 1. Hence, we used the exponential disk profile to model the underlying galaxy. We convolved a PSF image, generated from stars within the FoV of the target. The modeled output galaxy image and the residual image that contains the AGN in S II-band obtained from GALFIT, are shown in Fig. 2.3.

Ideally, AGN flux, can be acquired from the photometry of the residual image containing the AGN at the center. But practically, because of poor SNR in many epochs of data, it is very difficult. Hence, we carried out aperture photometry on the modeled galaxy images at different concentric aperture sizes and the obtained galaxy-fluxes plotted against apertures are shown in Fig. 2.4, where the solid lines represent the best-fit curves for B, R, Hα and S II-bands. The host-galaxy fluxes were measured from the best fit curves at the same size of the aperture used at individual epoch for photometry of the target source in B, R, Hα and S II-bands. The host-galaxy fluxes were then subtracted from the observed total fluxes in those filters to get the AGN flux.

Generation of Hα emission line light curve

The accumulated data on Mrk 590, enables generation of Hα emission line light curve by three methods.

Method 1

The observed flux in the narrow S II-band ($F_{\mathrm{S\,II,tot}}$) contains both Hα line ($F_{\mathrm{H}\alpha}$) and continuum fluxes (F_{cont}). The variable continuum originates

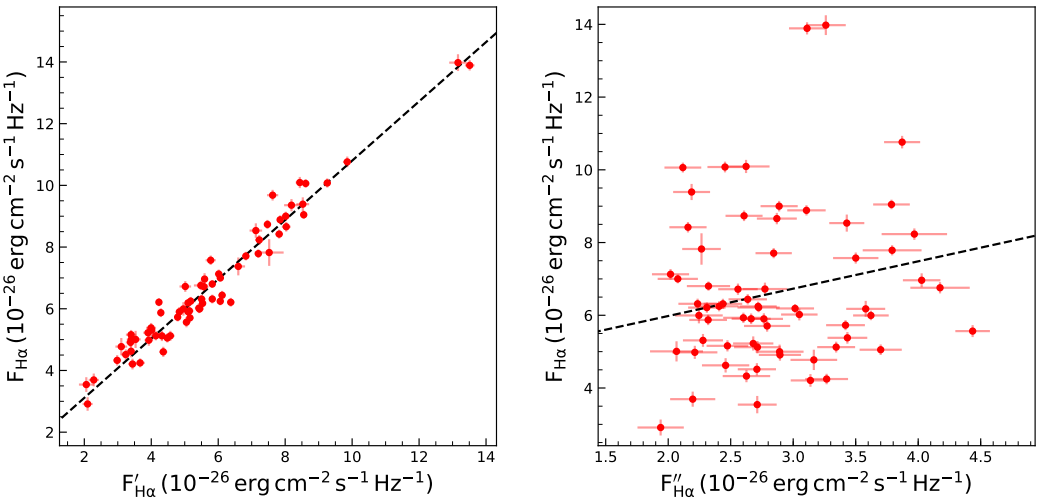

Figure 2.5: The Hα fluxes ($F_{H\alpha}$) evaluated using the continuum observations done in the narrow Hα filter as a function of Hα fluxes ($F'_{H\alpha}$) evaluated using broad B-band (left) and that ($F''_{H\alpha}$) obtained from R-band using PL spectrum of accretion disk (right). The dashed lines represent the best linear fits. Near simultaneous observations between the narrow Hα filter and the broad B and R-bands were used in both the plots.

from the accretion disk whose contribution to the observed S II-band fluxes ($F_{\rm S\,II,tot}$) would make the derived lag between the optical/UV continuum and Hα line shorter than the actual lag (Koshida et al., 2014). Therefore, the accretion disk contributions to the observed line fluxes need to be removed to get the actual time lag between optical B-band and Hα fluxes. The observations in narrow Hα-band contain continuum flux ($F_{\rm H\alpha,cont}$) from accretion disk. Hence, only Hα line flux ($F_{\rm H\alpha}$) can be obtained from the observed $F_{\rm S\,II,tot}$ as follows

$$F_{\rm H\alpha} = F_{\rm S\,II,tot} - F_{\rm H\alpha,cont} \tag{2.2}$$

Method 2

The continuum contribution from the accretion disk to the observed S II-band flux can also be evaluated from the observed B-band data. This is done by considering a power-law (PL) spectrum of the accretion disk given by Koshida et al. (2014)

$$F_{\rm S\,II,cont}(t) = F_B(t)\left(\frac{\nu_{\rm S\,II}}{\nu_B}\right)^{\alpha} \tag{2.3}$$

where $f_{\rm S\,II,cont}$(t) and f_B(t) represent the continuum flux of the S II-band from the accretion disk and the B-band flux at time t, respectively. The ν_B and $\nu_{\rm S\,II}$ are the effective frequencies of B and narrow S II bands, respectively, and α is the power-law index. According to Tomita et al. (2006), the power-law index of the accretion-disk component of the flux in optical and near-infrared may vary from -0.1 to +0.4. Kishimoto et al. (2008) found $\alpha = 0.44 \pm 0.11$ from spectropolarimetric observations. Using the quasar composite differential spectrum observed by the Sloan Digital Sky Survey, Wilhite et al. (2005) obtained a power-law index of $\alpha = 0$. We calculated

the continuum contribution in the S II-band flux for α = 1/3 as prescribed by standard accretion disk model (Shakura & Sunyaev, 1973). Finally, we subtracted the $f_{\rm S\,II,cont}$ from the observed S II-flux to get the Hα line flux ($F'_{\rm H\alpha}$) as

$$F'_{\rm H\alpha} = F_{\rm S\,II,tot} - F_{\rm S\,II,cont} \tag{2.4}$$

The Hα fluxes evaluated using the continuum observations done in the narrow Hα filter (Equation 2.2) and broad B-band (Equation 2.4) are found to be similar. This is shown in Fig. 2.5 (left) that includes those points which have near simultaneous observations in the B and narrow Hα filters. From linear least squares fit to the data, we found

$$F_{\rm H\alpha} = (0.96 \pm 0.03) F'_{\rm H\alpha} + 1.19 \pm 0.17 \tag{2.5}$$

Method 3

The observed R-band fluxes contain continuum contribution from the accretion disk and the redshifted Hα line flux from the BLR. To get a lag between B and the Hα line flux derived using the observations in the broad R-band, it is necessary to subtract the continuum contribution in the observed R-band flux. However, such decomposition is difficult to perform as the AGN continuum is the major contributor to the total flux. Assuming a PL spectrum of accretion disk, we measured the AGN continuum contribution to the observed host-corrected R-band fluxes from the near simultaneous B-band fluxes as

$$F_{\rm R,cont}(t) = F_B(t) \left(\frac{\nu_R}{\nu_B}\right)^{\alpha} \tag{2.6}$$

We used $\alpha = 1/3$ considering a standard accretion disk. From the observed

R-band fluxes the derived R-band continuum was subtracted to get the Hα line fluxes as

$$F''_{\mathrm{H}\alpha} = F_R - F_{\mathrm{R,cont}} \tag{2.7}$$

The Hα fluxes ($\mathrm{F}_{\mathrm{H}\alpha}$) evaluated using the continuum observations done in the narrow Hα filter (Equation 2.2) are plotted as a function of the Hα line fluxes ($\mathrm{F}''_{\mathrm{H}\alpha}$) derived from Equation 2.7 shown in Fig 2.5 (right). We could not find any strong correlation between $\mathrm{F}''_{\mathrm{H}\alpha}$ and $\mathrm{F}_{\mathrm{H}\alpha}$. From linear least squares fit to the data points, we found a Pearson correlation coefficient of $\mathrm{r} = 0.152$ with a p value of 0.228.

The errors in the final flux values in B, R, Hα and S II were estimated using the method of propagation of errors during the various steps of flux calibration.

2.3.2 H0507+164

The acquired images of H0507+164 were processed following the standard procedures using IRAF and MIDAS software. We performed point spread function (PSF) photometry on the images using the *daophot* and *allstar* packages available in MIDAS to obtain the instrumental magnitudes of the object and the comparison stars present in the same CCD frames in optical V and NIR J, H, $\mathrm{K_s}$ bands. The observed image in V-band is shown in Fig. 2.6.

The target AGN appears point like in the observed optical and NIR bands. The contribution of host galaxy to the derived brightness of H0507+164 is thus negligible. The obtained instrumental magnitudes from PSF photometry, were converted to standard magnitudes via differential photometry of few stars in the field whose apparent magnitudes were taken from the SIM-

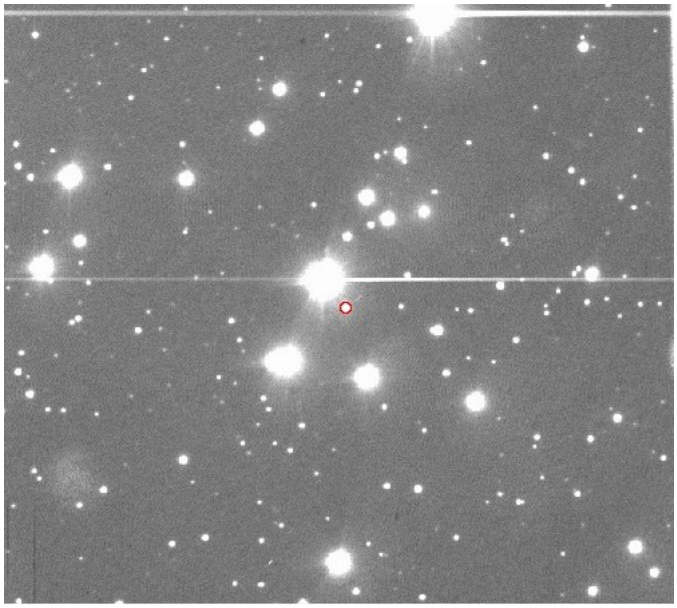

Figure 2.6: Observed field of H0507+164 in V-band. The target source H0507+164 is shown with a circle.

BAD database [8]. The standard magnitudes of H0507+164 were corrected for Galactic extinction using the values taken from NED and then converted into fluxes.

Subtraction of the accretion disk contribution to the observed NIR flux

The observed NIR fluxes are mainly dominated by the radiation from the torus via re-processing of the central UV/optical continuum emission by the hot dust. The observed NIR fluxes are also contaminated by variable flux from the accretion disk (Tomita et al., 2006; Kishimoto et al., 2008; Lira et al., 2011). This accretion disk contamination would make the calculated time lag between the optical and NIR light curves shorter than the actual lag (Koshida et al., 2014). Therefore, the contribution of the accretion disk to the observed NIR fluxes needs to be removed to get the true time lag, between optical and NIR flux variations. The contribution of the

[8] http://simbad.u-strasbg.fr/simbad/

accretion disk in the J, H, K_s-bands in each of the epochs of observations was estimated by considering a power-law spectrum of the accretion disk following Koshida et al. (2014) and given by

$$f_{\rm NIR}^{\rm AD}(t) = f_V(t)\left(\frac{\nu_{\rm NIR}}{\nu_V}\right)^{\alpha} \tag{2.8}$$

where $f_{\rm NIR}^{\rm AD}(t)$ and $f_V(t)$ are the accretion disk component of the NIR flux and the V-band flux at time t, ν_V and $\nu_{\rm NIR}$ represent the effective frequencies of V and the NIR (J, H, K_s) bands, respectively, and α is the power-law index.

The observations carried out in the optical and each of the NIR bands differ by typically less than 300 seconds at any given epoch, and therefore, they were treated as simultaneous observations for the purpose of removing the accretion disk contamination to each of the NIR bands. To calculate $f_{\rm NIR}^{\rm AD}(t)$, we assumed a power-law index of 1/3 prescribed by the standard accretion disk model (Shakura & Sunyaev, 1973), following Koshida et al. (2014). It is known that AGN show spectral variability with a bluer-when-brighter behavior (Meusinger et al., 2011), that demands adoption of a time dependent α to correct for the accretion disk contamination to NIR fluxes. Our single optical V -band observations could not allow determination of α at each epoch of our observations. Use of constant α might have some effect on the corrected J-band fluxes, however, it will have less effect on the corrected K_s -band flux values.

2.3.3 Z229−15

We followed the standard procedures to process the observed optical and NIR images. The observed field in V-band is shown in Fig. 2.7.

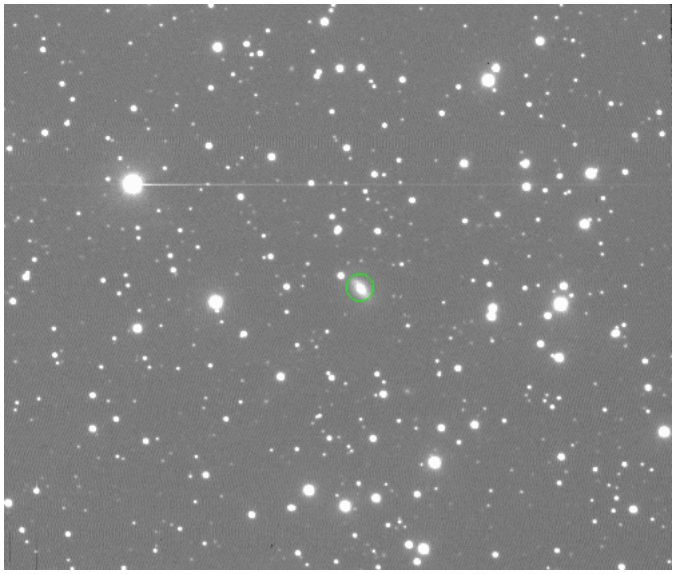

Figure 2.7: Observed field of Z229−15 in V-band. The target AGN Z229−15 is shown with a circle.

Optical photometry

We used the *daofind* task in IRAF to detect the objects in the observed image frames. We carried out the photometry of those detected objects using the *phot* task available in IRAF. We selected two comparison stars from the detected objects having similar brightness to the AGN to carry out differential photometry and bring the instrumental magnitude of the AGN to the standard system. We obtained the instrumental magnitudes in several concentric circular apertures centered on the comparison stars starting from FWHM to about 8 times the FWHM. Growth curves were generated by plotting the obtained instrumental magnitudes as a function of the apertures and the final instrumental magnitude for each of the comparison stars was obtained by COG method for each epoch. This adoption of the COG method makes sure that the total flux from a point source is measured. The growth curve for a comparison star is shown in Fig. 2.8. A straight line was fit based on linear least squares to the photometric points between 4 and 6

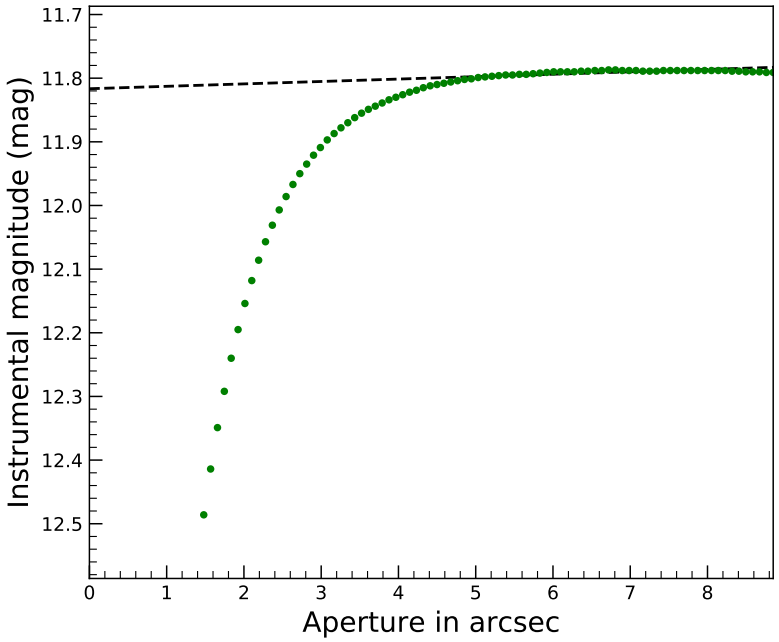

Figure 2.8: Curve of growth of a comparison star in V-band. The dashed black line represents the linear least squares fit to the points having aperture sizes between 4 and 6 times the FWHM.

times the FWHM of the point source, where the COG smoothly merges with the background and the intercept of that fitted line (shown as dashed line in Fig. 2.8) was taken as the magnitude of the point source. The two comparison stars are found to be non-variable during the duration of our observations. The differential light curve (DLC) in the V band of these two stars is illustrated in Fig. 2.9. The DLC is found to have a standard deviation of 0.008 mag, while the mean error of the photometric points is 0.004 mag. Gopal-Krishna et al. (1995) found that the photometric errors given by the *phot* task in IRAF is an underestimate by a factor of about 1.75, which implies that the standard deviation of the DLC obtained for the the comparison two stars is consistent with the photometric error, confirming them as non-variable stars.

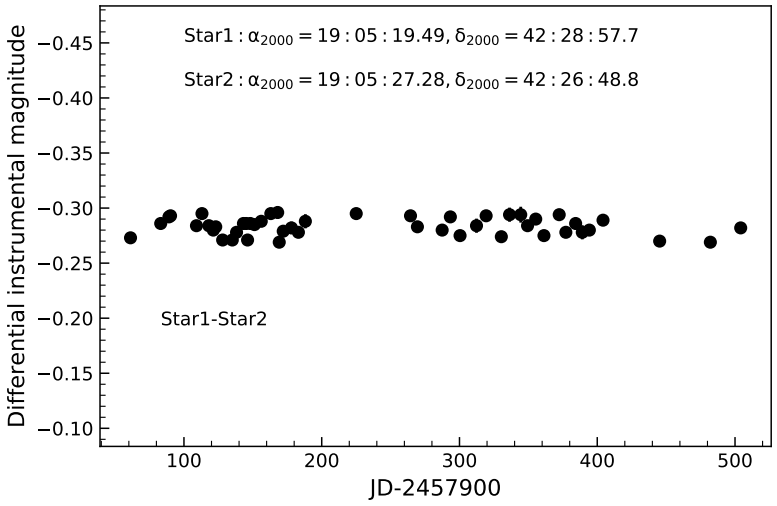

Figure 2.9: Differential light curve of the two comparison stars, Star 1 and Star 2 in the observed field of Z229−15 in V band.

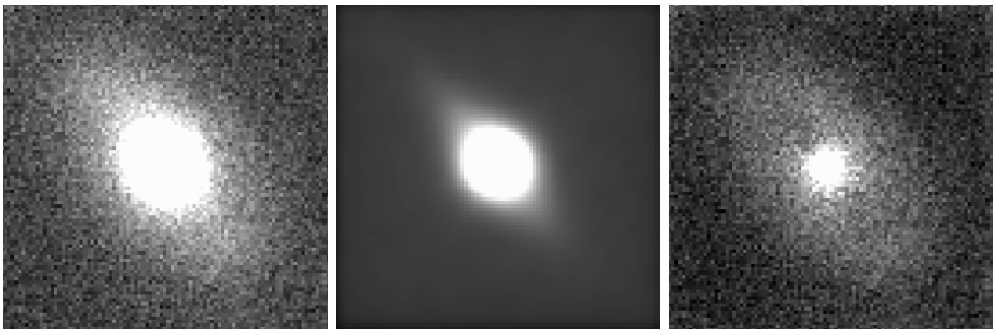

Figure 2.10: Observed image of Z229−15 in V-band (left), modeled galaxy image (middle) and the residual image containing the AGN at the center (right) obtained using GALFIT.

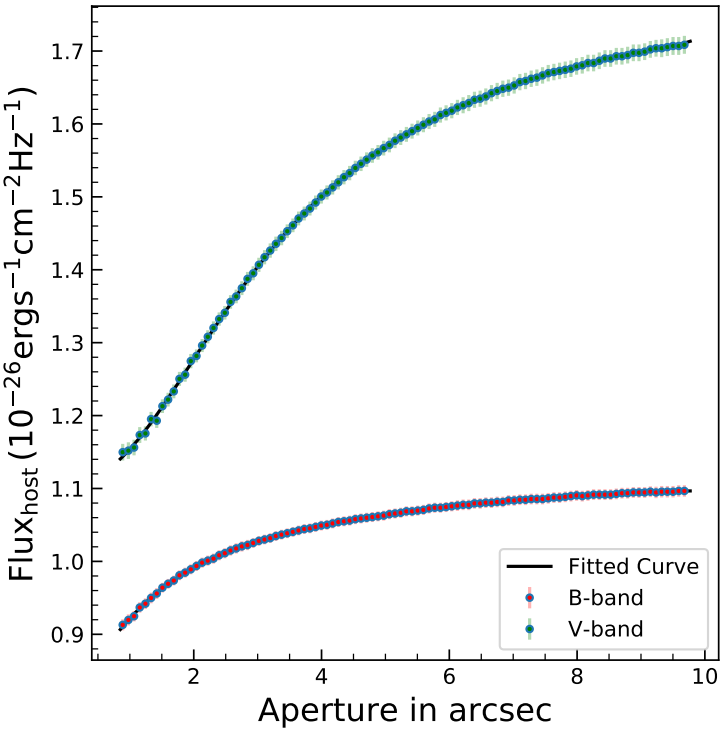

Figure 2.11: Host-galaxy flux against the aperture radii. The points with error bars represent the galaxy-flux values and the solid black lines are the best polynomial fits.

Correction for the host-galaxy contribution

We can not apply the COG method used to get the magnitude of the comparison stars for the target AGN as both the optical B and V-band images have a prominent host galaxy contribution (see Fig. 2.10 left for V-band). The host galaxy contamination in both the B and V-band needs to be removed to get the actual flux from the AGN. For that, we used GALFIT to model the observed image. We fitted a Sérsic profile and an edge-on disk profile component to the data of one good epoch of observation in B and V-bands. We used a point source with the best SNR, present close to the target source for generating the model PSF. The modeled galaxy and the residual image containing the AGN (after subtraction of the model galaxy) at the center for V-band are shown in the middle and right panels of Fig. 2.10. Ideally, light curves of the AGN, can be generated from the photometry of the residual AGN image produced by the GALFIT. However, practically, it is difficult due to the poor SNR in many epochs of data. Therefore, we followed the following approach to get the light curve of the AGN devoid of the host galaxy. For each epoch of observation, we performed aperture photometry on the observed target Z229−15 at an aperture radius equal to the aperture used for the comparison stars of that epoch. The derived flux ($F_{\rm total}$) carries the light from the AGN ($F_{\rm AGN}$) and the host galaxy ($F_{\rm host}$). Now, to subtract the host galaxy star light, aperture photometry was carried out on the modeled galaxy image (obtained from GALFIT and without the AGN) for different concentric aperture sizes. We generated the galaxy flux as a function of radii from its center and then modeled as a polynomial which is shown in Fig. 2.11. After getting the functional form of the galaxy light distribution, we found the contribution of galaxy star-light at the radius used for the photometry of Z229−15 for that epoch. This was

then subtracted from the total flux to get the true AGN flux as

$$F_{\rm AGN} = F_{\rm total} - F_{\rm host} \tag{2.9}$$

The above method was carried out for each epoch of observation to arrive at the final B and V-band light curves of the AGN. Finally, we converted the observed instrumental magnitudes into apparent magnitudes via differential photometry relative to the two comparison stars having brightness similar to the AGN in the field, whose apparent magnitudes were taken from Barth et al. (2011) and Fedorov et al. (2011) for V and B band, respectively. These comparison stars which are found to be non-variable during our monitoring period, were also used as non-variable reference stars by Barth et al. (2011) in their optical monitoring program. The obtained standard magnitudes were corrected for the Galactic extinction from NED. These magnitudes were then converted into fluxes using the zero points from Bessell (1979).

Infrared photometry

The acquired NIR images in J, H and K_s bands have very poor SNR compared to the optical B and V-band images. We also found the PSF to change across the image frames. We tried to obtain the magnitude of the comparison stars and the target Z229−15 (as the host galaxy is not seen) using the COG method similar to the optical band. However, the COG was found not to smoothly merge with the background and showed many wiggles instead (see Fig. 2.12). Hence, we followed a two step approach to obtain the total flux from the comparison stars and the target AGN. First, we performed aperture photometry on a sequence of circular apertures. The SNR was calculated at each of the aperture. We plotted SNR as a function of aperture as shown in Fig. 2.13 (left) to find the aperture at which the SNR

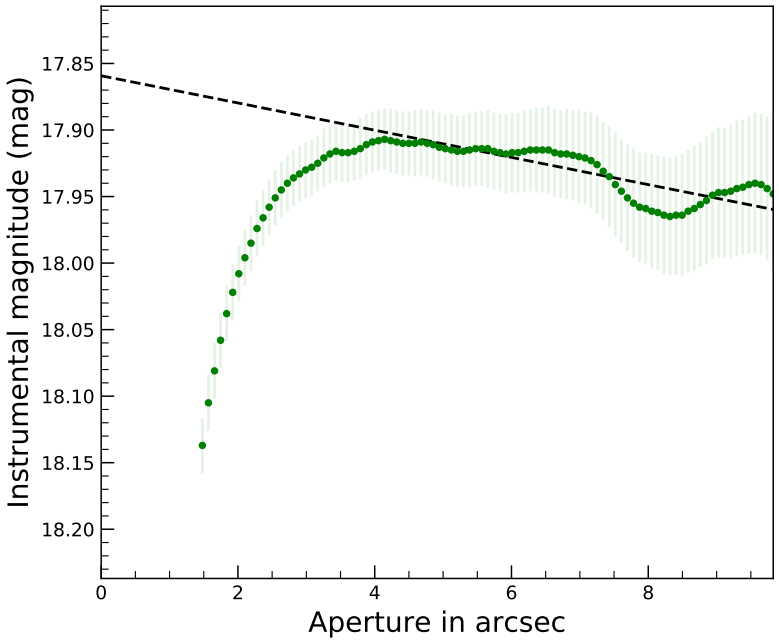

Figure 2.12: COG of the comparison star in K_s -band. The dashed black line represents the linear least squares fit to the points having aperture sizes between 4 and 6 times the FWHM.

is maximum. We used that aperture as the optimum aperture to find the magnitude of the objects. The aperture at which the SNR is maximum is found to change from epoch to epoch. Because of poor SNR, the optimum aperture found by this method is much smaller than the FWHM and therefore, the flux obtained for the comparison star and the target AGN within the optimum aperture is always an underestimation.

Therefore, we need to apply aperture correction to offset for the missing flux obtained at smaller apertures to get the actual brightness of the comparison stars and the AGN. The aperture correction was estimated using a mean differential curve of growth (DCOG) analysis. There are three point sources in the observed image frames in the NIR bands. We calculated the magnitude difference between successive apertures, i.e $\Delta m = m_{i+i} - m_i$, where i refers to the aperture radius for each of those stars, and plotted Δm

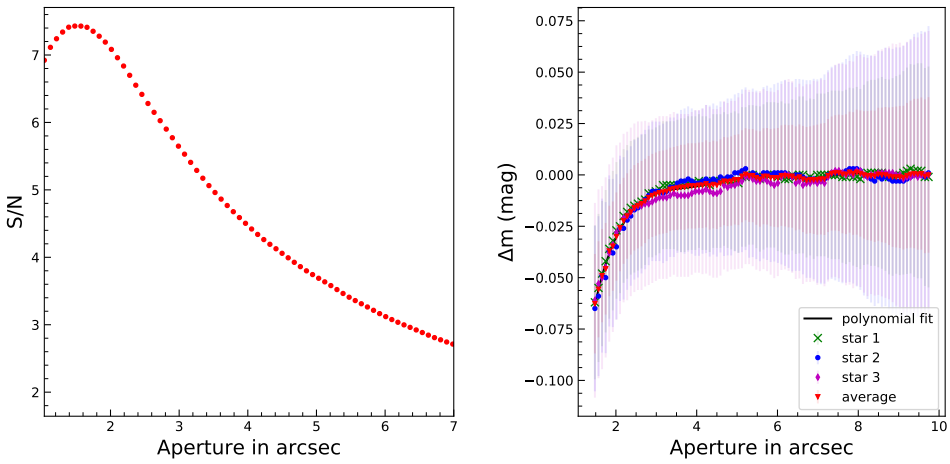

Figure 2.13: SNR as a function of aperture (left). Differential magnitude between successive apertures against aperture size (right). The green, blue, purple and the red points are the differential magnitudes for comparison star 1, star 2, star 3 and average of those, respectively. The black solid line represents the best polynomial fit to the average differential magnitudes.

as a function of aperture radii as shown in Fig. 2.13 (right panel). We obtained the mean DCOG by taking the average of the DCOG obtained for these three stars. We fit a polynomial to the mean DCOG. We applied the aperture correction by taking the difference between the Δm at the FWHM and the Δm at the optimum aperture obtained from the best polynomial fit to each of the comparison stars and the target AGN to get their true brightness. The final NIR apparent magnitudes were obtained by carrying out differential photometry of the AGN with respect to the three comparison stars, whose standard magnitudes were taken from the SIMBAD data base. We applied correction for Galactic extinction using the values taken from NED. The NIR apparent magnitudes were then converted into flux units using the zero points from Bessell et al. (1998).

The NIR fluxes obtained by the procedure outlined above will have flux contribution from the torus, the host galaxy, and the infrared radiation com-

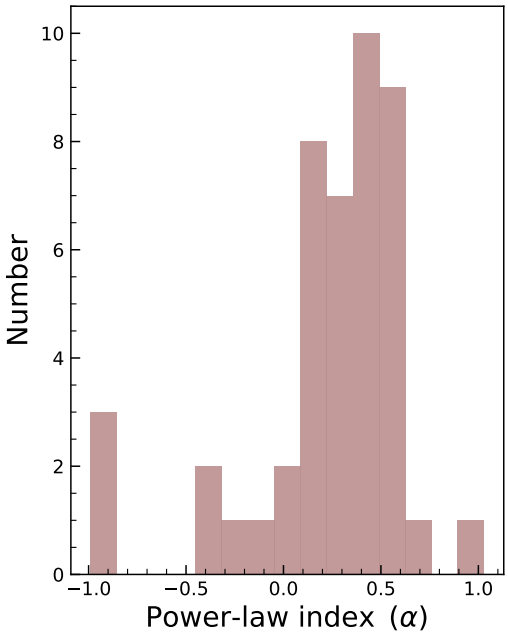

Figure 2.14: Distribution of the spectral index α.

ing from the accretion disk. The observed infrared flux can thus be written as

$$F_{\rm obs} = F_{\rm dust} + F_{\rm host} + F_{\rm AD} \tag{2.10}$$

Therefore, to generate the final infrared light curves that contain only the reprocessed optical/UV continuum from the accretion disk by the dust torus ($F_{\rm dust}$), we need to remove the contamination from the host galaxy ($F_{\rm host}$) and the AD ($F_{\rm AD}$) from the observed NIR fluxes ($F_{\rm obs}$). However, due to poor SNR, the AGN is only visible in the NIR images. Therefore, we did not attempt to correct for $F_{\rm host}$ and instead aimed to correct only for the accretion disk contamination $F_{\rm AD}$ to the observed NIR emission.

2.3.4 Subtraction of the accretion disk (AD) component to the NIR flux

The observed NIR flux contains contamination from the AD (Tomita et al., 2006; Kishimoto et al., 2008; Lira et al., 2011). This AD contribution to the

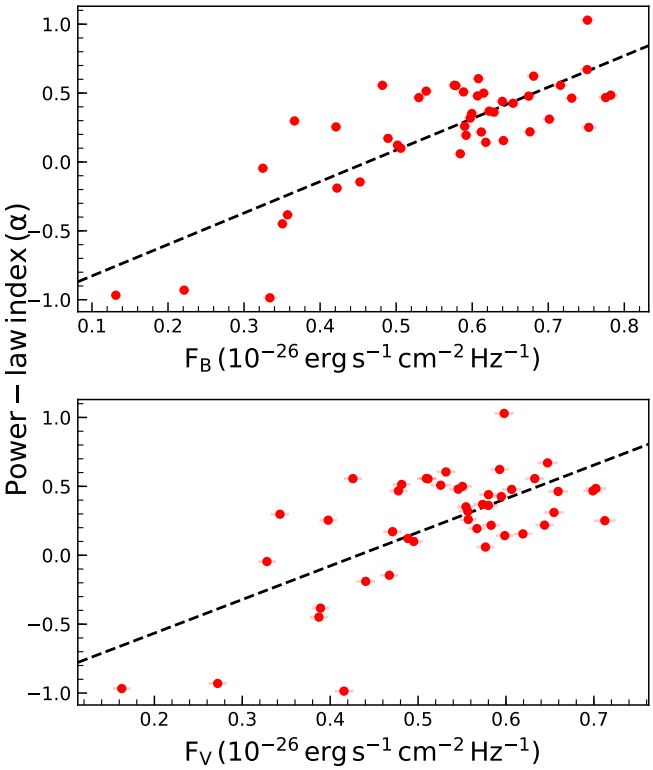

Figure 2.15: Dependency of α on B (top) and V-band (bottom) flux.

NIR flux makes the obtained lag between the optical and NIR continuum shorter than the true lag (Koshida et al., 2014). So, the contribution of the AD to the observed NIR fluxes needs to be removed to get the actual time lag between the optical and NIR flux variations. The AD contribution to the NIR fluxes was estimated by considering a power-law spectrum of the AD (Koshida et al., 2014) as given by Equation 2.8.

AGN do show spectral variations with their brightness (Meusinger et al., 2011) with bluer when brighter behaviour (Kokubo et al., 2014), which indicates that AGN have a time dependent power-law index α. Hence, each epoch of NIR observation has to be corrected for the AD contamination using the α evaluated at each epoch. The observations in the optical and each of the NIR bands were typically carried out within 300 sec of one another at any given epoch, and therefore, they were treated as nearly simultaneous

to remove the AD contamination to each of the NIR bands. We estimated α at each epoch of observation from the near-simultaneous observations in the optical B and V-bands using the relation given below (Mandal et al., 2019)

$$\alpha = \frac{ln(f_B/f_V)}{ln(\nu_B/\nu_V)} \tag{2.11}$$

where, f_B and f_V represent the flux densities in B and V-band, respectively, while ν_B and ν_V are the frequencies in B and V-band. The distribution of α obtained from the observations between B and V bands for all the epochs is shown in Fig. 2.14. The estimated values of α vary between -0.99 and 1.03. The median value of α is found to be 0.318 with a standard deviation of 0.418. This is similar to α = 1/3 expected from the standard accretion disk model (Shakura & Sunyaev, 1973). We found α to be positively correlated with the B and V-band brightness with Spearman rank correlation coefficients of $0.598^{+0.012}_{-0.012}$ and $0.442^{+0.015}_{-0.016}$ with probability of no correlation p-values of $10^{-5} \pm 10^{-6}$ and 0.002 ± 0.001, respectively following a bluer when brighter trend. The variation of α as a function of B and V-band fluxes are shown in Fig. 2.15. A bluer when brighter trend is evident. The α value evaluated at each epoch was used to calculate the epoch-wise value of $F_{\rm AD}$ using Equation 2.8. The obtained values of $F_{\rm AD}$ were then subtracted from the observed $F_{\rm obs}$ to get the IR radiation from the torus. We used error propagation method to find the uncertainties in the flux values in the different bands.

Chapter 3

BLR REVERBERATION ON MRK 590, A CHANGING LOOK AGN [1]

Mrk 590 is a changing look AGN at a redshift z = 0.0264. It was in its brightest state in 1990s. Then its continuum flux decreased by a factor of more than 100 during the period 2006 − 2012 over all wavelengths and broad Hβ line completely disappeared during that period. Again broad emission lines reappeared in 2017 after being absent for about 10 years with continuum flux about 10 times less than that observed in its most bright state in 1990s (Raimundo et al., 2019). From the previous studies on Mrk 590, it is found that the BLR lag based on Hβ line ranges from 19.5 days to 30 days (Zu et al., 2011; Bentz et al., 2013) with a black hole mass of $4.75 \pm 0.74 \times 10^7\,M_\odot$ measured by Peterson et al. (2004). This chapter discusses the analysis of the data as well as the results obtained on Mrk 590.

3.1 ANALYSIS

3.1.1 Light curves

Mrk 590 was observed during the period July 2018 to December 2018 in broad band B and R filters and narrow band Hα and S II filters. The light curves generated as per the procedures given in Chapter 2 are given in Fig. 3.1. The source is a radio-quiet Seyfert galaxy and therefore, there is negligible/no contribution from the relativistic jets to the observed flux variations seen in Fig. 3.1.

The flux variability properties of the target source were characterized by the normalized excess variance (F_{var}; Edelson et al. 2002; Vaughan et al.

[1]The contents of this chapter are based on Mandal et al. (2021a) (MNRAS, under preparation)

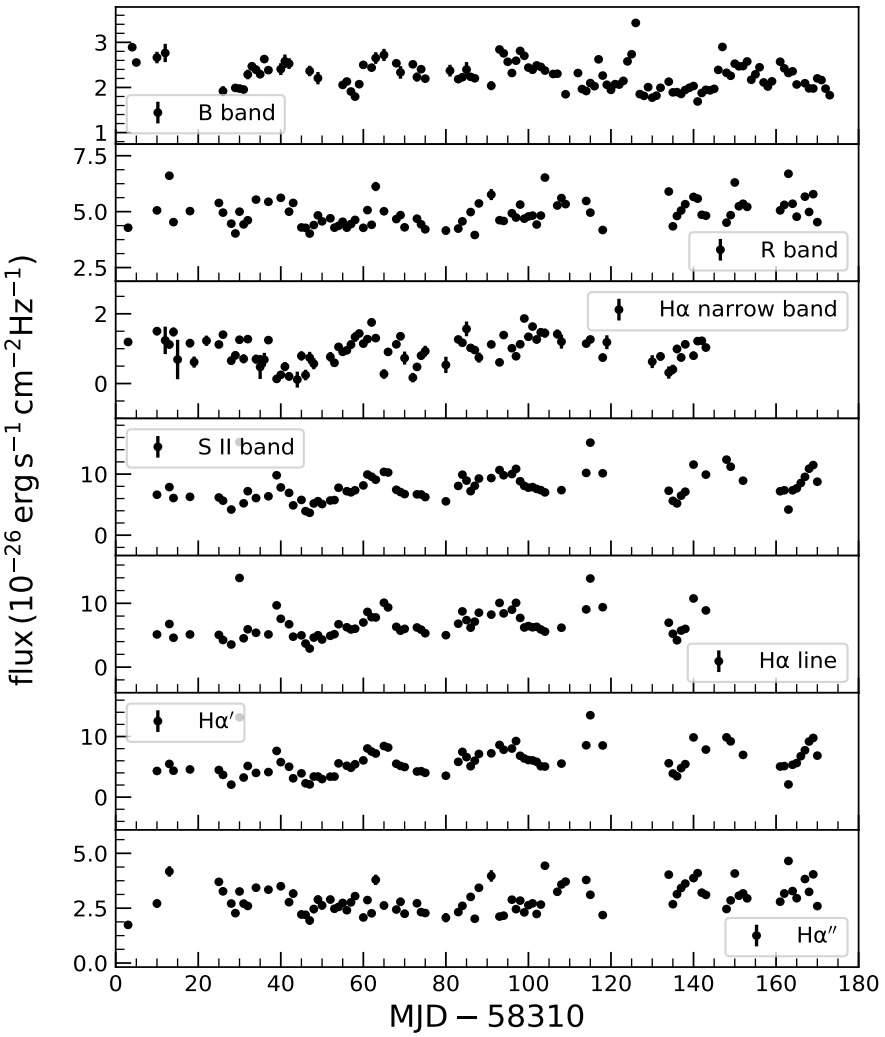

Figure 3.1: The light curves of Mrk 590 in broad band B and R filters and narrow band Hα and S II filters for the period July, 2018 to December, 2018. Flux in narrow Hα-band was subtracted from the S II-band fluxes to get the Hα line light curve, whereas Hα' and Hα'' light curves were obtained considering PL spectrum of accretion disk from narrow S II and broad R bands, respectively.

2003; Rani et al. 2017) defined as

$$F_{var} = \frac{\sqrt{S^2 - \overline{\delta_{err}^2}}}{\bar{f}} \tag{3.1}$$

where, $\bar{f}$, S^2 , $\overline{\delta_{err}}$ represent the mean flux, variance and mean error, respectively, for N observations and are given as

$$\bar{f} = \frac{1}{N}\sum_{i=1}^{N} f_i \tag{3.2}$$

$$S^2 = \frac{1}{N-1}\sum_{i=1}^{N} (f_i - \bar{f})^2 \tag{3.3}$$

$$\overline{\delta_{err}^2} = \frac{1}{N}\sum_{i=1}^{N} \delta_i^2 \tag{3.4}$$

The uncertainties in the $F_{\rm var}$ values were obtained following Edelson et al. (2002) as

$$err(F_{var}) = \sqrt{\left(\sqrt{\frac{1}{2N}}\frac{\overline{\delta_{err}^2}}{\bar{f}^2 F_{var}}\right)^2 + \left(\sqrt{\frac{\overline{\delta_{err}^2}}{N}}\frac{1}{\bar{f}}\right)^2} \tag{3.5}$$

We also calculated the ratio of the maximum to minimum flux denoted by R_{max} in the light curves.

The results on the analysis of variability are given in Table 3.1. In addition to $F_{\rm var}$, we also give the mean flux and the standard deviation, R_{max}, the luminosity of AGN ($L_{\rm AGN}$) and its host galaxy ($L_{\rm host}$).

3.1.2 Cross-correlation function (CCF) analysis

B-band v/s narrow band light curves

Mrk 590 shows strong variations in the optical B-band and Hα line light curves (see Fig. 3.1). The Hα light curves used here were derived (a) by

Table 3.1: Variability statistics in B, R, narrow Hα and S II bands and for H_α line in observer's frame, where $\lambda_{\rm eff}$ is the effective wavelength in Angstroms. The average values ($< f >$) and the standard deviation σ of the light curves are in units of $10^{-26}\,{\rm erg\,s^{-1}\,cm^{-2}\,Hz^{-1}}$. The luminosities in each band are in erg s^{-1}.

Filter	$\lambda_{\rm eff}$	$< f >$	σ	$F_{\rm var}$	$R_{\rm max}$	log $L_{\rm host}$	log $L_{\rm AGN}$
B	4363	2.26 ± 0.05	0.31	0.132 ± 0.001	2.03	42.22 ± 0.01	43.36 ± 0.01
R	6410	4.95 ± 0.15	0.62	0.121 ± 0.001	1.69	43.98 ± 0.01	43.53 ± 0.01
Hα	6563	0.97 ± 0.13	0.40	0.379 ± 0.005	16.60	43.85 ± 0.01	42.81 ± 0.06
S II	6719	7.88 ± 0.12	2.26	0.286 ± 0.001	4.17	43.70 ± 0.01	43.71 ± 0.01
Hα line	6564.6	6.73 ± 0.17	2.17	0.321 ± 0.001	4.80	–	43.65 ± 0.01
Hα' line	6564.6	5.90 ± 0.13	2.28	0.385 ± 0.001	6.56	–	43.60 ± 0.01
Hα'' line	6564.6	2.94 ± 0.16	0.63	0.206 ± 0.001	2.68	–	43.29 ± 0.02

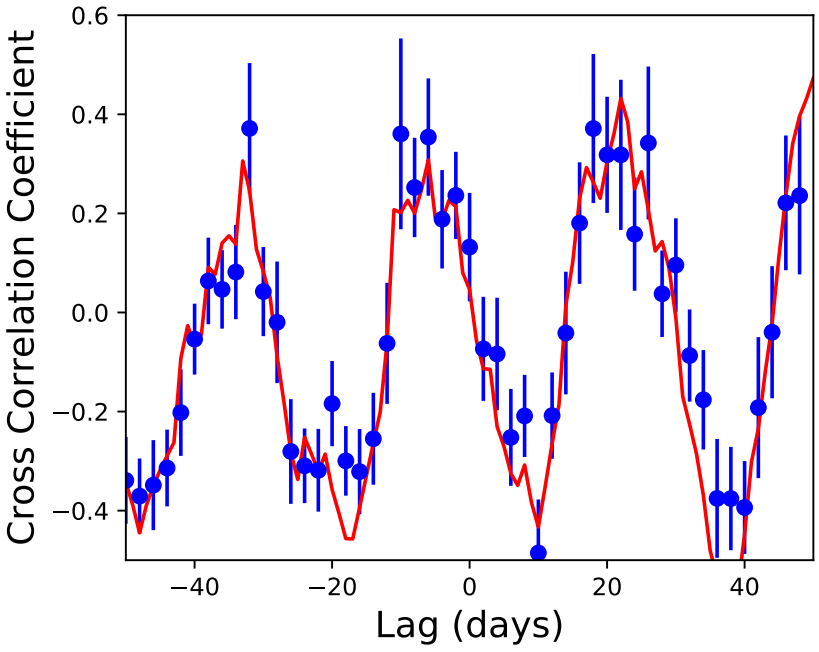

Figure 3.2: The CCF between B and Hα line light curves. The solid red line represents the ICCF, points with error bars show the DCF obtained using $\tau = 1$ day.

subtracting the observed fluxes in the narrow Hα band from that measured in the narrow S II band and (b) by subtracting the continuum obtained by extrapolating the observed B-band flux using $\alpha = 1/3$ from the measured S II fluxes. To calculate the time lag between the B-band and the Hα line light curves, we employed two well-known methods, namely the interpolated cross-correlation function (ICCF; Gaskell & Sparke, 1986; Gaskell & Peterson, 1987) and the discrete cross-correlation function (DCF; Edelson & Krolik, 1988). The total duration of S II-band data is $\sim$160 days. Hence, we first evaluated the CCF in the range -50 days to $+50$ days considering the total duration of observation should exceed at least 3 times the expected maximum lag to locate the peak of the CCF (Peterson & Horne, 2004) using a bin of $\tau = 1$ day (median time resolution of our observation). The CCFs (Fig. 3.2) show two peaks; one is at around -6 days and another is at around $+22$ days. As negative lag (line emission leading the continuum emission) here is physically not possible, we used the centroid of the CCF around the positive peak at around +22 days to estimate the expected BLR lag between B-band and Hα line. The lag can be determined either by the lag corresponding to the peak of the CCF ($\tau_{\rm peak}$) or the lag corresponding to the centroid of the CCFs ($\tau_{\rm cent}$). $\tau_{\rm cent}$ better represents the expected time lag, particularly in cases when the light curves are either noisy and/or sparsely sampled having less number of points (Peterson et al., 1998b). We therefore, calculated the centroid of the CCF following Peterson et al. (1998b) as

$$\tau_{\rm cent} = \frac{\Sigma_i \, \tau_i CCF_i}{\Sigma_i \, CCF_i} \tag{3.6}$$

The centroid was evaluated by considering the points that are within 80 per cent of the maximum of the ICCF as shown in Fig. 3.3. The distribution of cross-correlation centroid (CCCD) obtained using ICCF via Monte

Carlo simulation based on the flux randomization (FR) and random subset selection (RSS) described in Peterson et al. (1998b) for 20,000 iterations is shown in the histogram of Fig. 3.3. The median of the CCCD is taken as a representation of the lag, which is found to be about 22.00 days in the observed frame. We calculated CCF using two methods (i) using the continuum contribution of the narrow Hα band to the S II band (left panel of Fig. 3.3) and (ii) considering a power law component with the power law index α = 1/3 (right panel of Fig. 3.3) to correct for the continuum contribution from the accretion disk in narrow S II-band data.

We evaluated the uncertainties in the derived lag using a model-independent Monte Carlo approach based on flux randomization (FR) and random subset selection (RSS) described in Peterson et al. (1998b) with the additional improvement, suggested by Wandel et al. (1999) and Peterson & Horne (2004). In Monte Carlo simulation, we first employed RSS method by randomly selecting N independent points from the parent light curve having N data points regardless of whether any point has previously been selected. The new light curve thus generated from RSS method contains M data points. Then we applied FR method to take into account the errors in the measured flux values by randomly modifying the fluxes of the M data points by adding the uncertainties of the measured flux multiplied with a random Gaussian value. For each Monte Carlo iteration, the CCF of the modified light curve was computed and the $\tau_{\rm cent}$ was obtained using the points within 80% of the CCF peak. We repeated this process for 20,000 iterations retaining only those CCF having peak value > 0.5 to make the cross correlation result significant. The histograms in Fig. 3.3 represent the cross-correlation centroid distribution (CCCD) using Monte Carlo simulation. The lag, obtained from the median of the CCCD, is found to be 22.00 days in the observed frame. Since the CCCD has a non-Gaussian shape,

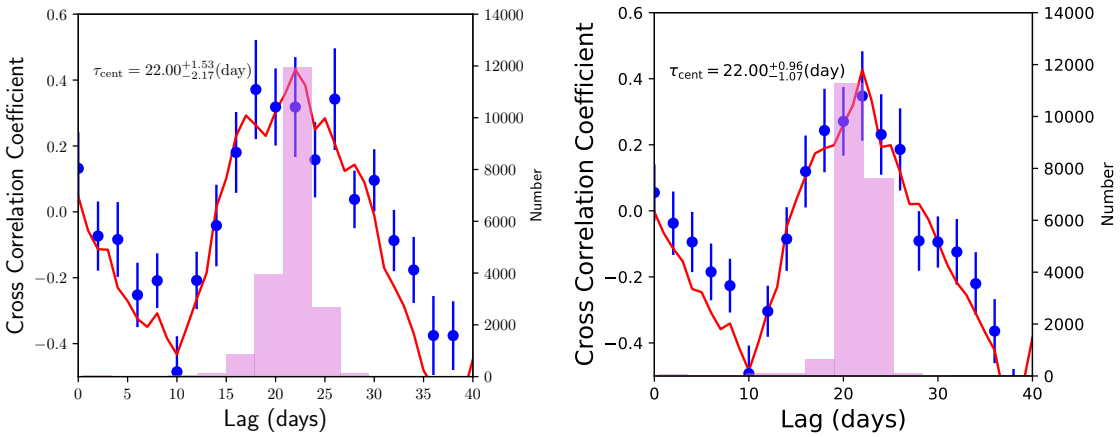

Figure 3.3: The CCFs between B and Hα line light curves (i) using observations in Hα band to correct for the continuum contribution to the S II band (left panel) and (ii) using a power-law contribution with the power law index = 1/3 (right panel) to correct for the accretion disk contamination in S II-band. The solid red line represents the ICCF, points with error bars show the DCF obtained using a bin width τ = 1 day. The shaded histograms show the distribution of τ_{cent} obtained using 20000 Monte Carlo simulation. The median value of the distribution is given on each panel.

we calculated the upper and lower uncertainties in the measured lag within 68% confidence interval around the median value as described in Mandal et al. (2018).

The obtained lags with their uncertainties between the B-band and Hα line light curves in the observed frame derived from the Monte Carlo simulation using ICCF method is given in Table 3.2. We could not find difference in the measured lags for those two different approaches. The rest frame time lag between B band and Hα line is found to be $21.44^{+1.49}_{-2.11}$ days. So the mean BLR size of Mrk 590 based on H_α line is $21.44^{+1.49}_{-2.11}$ days equivalent to $0.018^{+0.001}_{-0.002}$ pc.

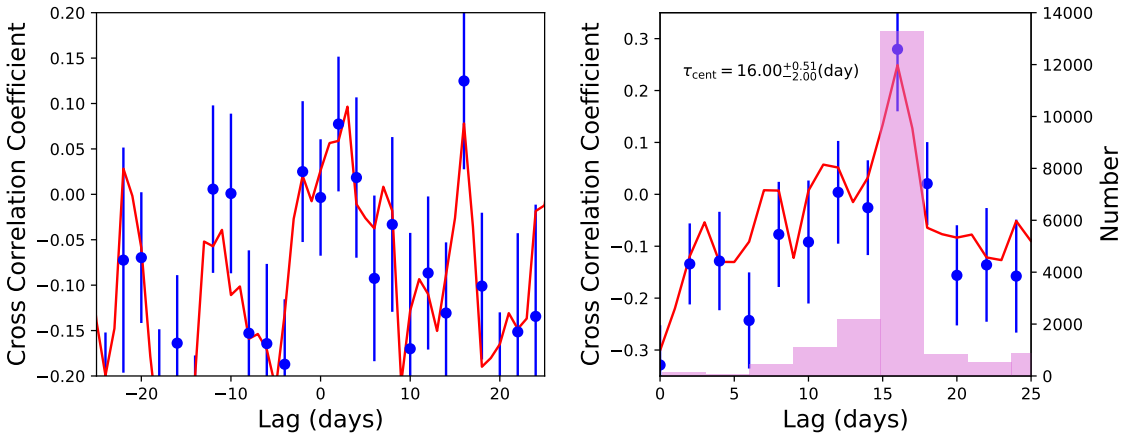

Figure 3.4: The CCFs between B and R (top panel) and continuum subtracted R with $\alpha = 1/3$ (bottom panel) are shown. The solid red line represents the ICCF, points with error bars show the DCF obtained using $\Delta\tau = 1$ day and the corresponding distribution of the $\tau_{\rm cent}$ obtained using 20,000 Monte Carlo Simulations is shown by histogram. The value of $\tau_{\rm cent}$ from the median of the distribution obtained using Monte Carlo simulation using ICCF is also noted in the bottom panel.

B-band v/s R-band light curves

The CCF between B and R-band light curves is shown in Fig. 3.4 (left). The host corrected R-band has contributions from continuum as well as the Hα line fluxes (see Fig. 2.1). This is also reflected in the CCF (Fig. 3.4; left panel), which shows two prominent peaks; one at smaller lag $\sim$3 days due to the contribution from the continuum flux originating from the accretion disk, and another at larger lag of $\sim$16 days, which is due to the contribution from Hα line flux from the BLR. We note a weak correlation with the peak of CCF $r_{\rm max}$ $\sim$0.1. This is because of the contribution from two spatially different regions to the R-band light curve. To have only the Hα line contributing to the measured flux in the R-band, we subtracted the contribution of the continuum to the observed R-band flux using Equation 2.7. We then,

Table 3.2: Lag measurements. Columns are (1) method used for continuum subtraction (2) filters (3) τ_{cent} with errors in days as obtained by ICCF methods in observer's frame. R-band fluxes are corrected for the continuum using power-law continuum with slope α.

method	filter	ICCF
(1)	(2)	(3)
direct	B−Hα	$22.00^{+1.53}_{-2.17}$
PL subtracted ($\alpha = 1/3$)	B−Hα	$22.00^{+0.96}_{-1.07}$
PL subtracted ($\alpha = 1/3$)	B−R	$16.00^{+0.51}_{-2.00}$

cross-correlated the B and continuum subtracted R-band light curves. We found a lag of ∼16 days in the observed frame with improved correlation of r_{max} ∼0.26 (Fig. 3.4; right panel). Such a weak correlation has also been found in other studies where reliable lag measurements have been claimed, e.g., broad band photometric RM has been carried out for NGC 4395 by Edri et al. (2012) between SDSS *g*, *r* and *i* filters, which provided a BLR size but with a weak correlation of r_{max} ∼0.1. The measured lag with uncertainties between B and continuum subtracted R-band is given in Table 3.2. Therefore, the lag between B and Hα line light curve obtained from continuum subtracted narrow S II band data is slightly larger compared to that of using continuum subtracted R-band as Hα line flux. This is because the narrow S II band has much smaller contribution from AGN continuum than in broad R-band.

Correlated errors in the light curves are found in many RM studies, specially in spectroscopic RM, when the emission line and continuum fluxes are extracted from the same spectra (Barth & Bentz, 2016). These correlated errors result in a spurious signal at zero lag in the CCF (Gaskell &

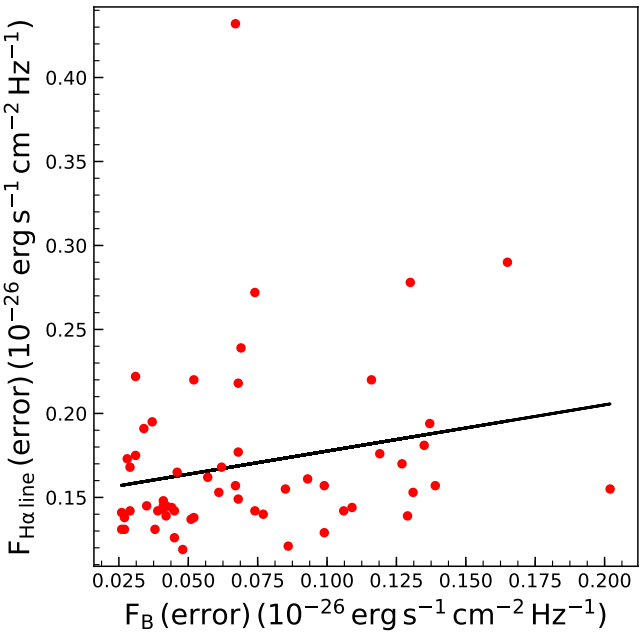

Figure 3.5: Variation of the errors in Hα line fluxes as a function of the errors in B-band fluxes. The black line represents the best fit straight line.

Peterson, 1987). We obtained light curves for Mrk 590 using photometric data acquired in different bands. To check for the presence of correlated errors if any in our obtained CCF analysis, we inspected the correlation between the errors in fluxes of B and Hα line (obtained using Equation 2.2) light curves. We found no strong correlation between them as can be seen from Fig. 3.5. The Pearson correlation coefficient (r) is found to be 0.216 with probability of no correlation p = 0.106. This suggests that the lag obtained from CCF analysis is not affected by any correlated errors.

3.2 DISCUSSION

3.2.1 Lag-luminosity correlation

We estimated the monochromatic continuum luminosity at 5100Å (L_{5100}) of 43.12 ± 0.01 erg s^{-1} from the single-epoch spectrum of Mrk 590 (see section 2.3.1). This corresponds to an expected BLR size of $\sim$ 12 days

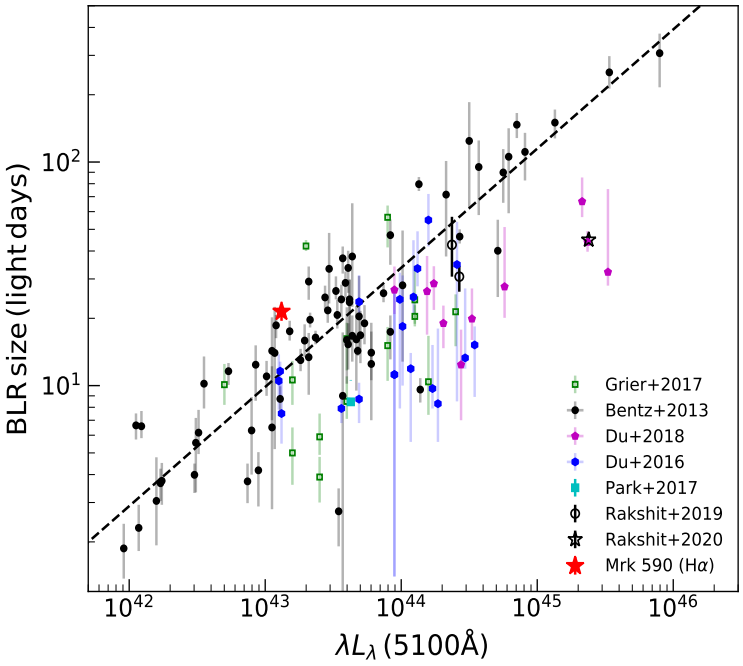

Figure 3.6: The position of Mrk 590 shown by red colour star point along with the other AGN from literature in lag−luminosity plane. The best-fit BLR size−luminosity relation from Bentz et al. (2013) is also shown by dashed black line.

according to the best-fit size-luminosity relation of Bentz et al. (2013), which is found to be a factor of 2 smaller than our measurement. We note that L_{5100} could be affected by the host galaxy star-light. Our photometric image decomposition method provides host galaxy contribution to the total flux of $\sim 50\%$ in the observed S II band data, whereas, the host galaxy corrected AGN luminosity in the B band is found to be $\log L_{AGN} = 43.36 \pm 0.01$ erg s^{-1}, which is in excellent agreement with the AGN luminosity of $\log L_{AGN} = 43.31 \pm 0.05$ erg s^{-1} at 5100 Å wavelength recently obtained by Kokubo & Minezaki (2020).

The position of Mrk 590 is illustrated in the size-luminosity plane (see Figure 3.6) based on our BLR size measurement from Hα line and L_{5100} (host uncorrected) along with other AGN culled from literature. Our measure-

ment does not significantly deviate from the best-fit relation of Bentz et al. (2013). Peterson et al. (1998a) performed Hβ spectroscopic RM of Mrk 590 and estimated a range of BLR size depending on the observational epoch, from $14.0^{+8.5}_{-8.5}$ light-days (MJD = 48848−49048) to $29.2^{+4.9}_{-5.0}$ light-days (MJD = 49183−49338). Therefore, our measured lag is consistent with the measurement of Peterson et al. (1998a). Note that, our result is based on Hα lag. Bentz et al. (2010) found that on-average Hα lag is 1.54 times higher than Hβ lag, therefore, the position of Mrk 590 in Figure 3.6 is consistent with the expectation.

3.2.2 Black hole mass measurement

The spectrum of Mrk 590, obtained by Peterson et al. (1998a), showed clear presence of broad Hβ line with an FWHM of ~ 2300 km s^{-1}. However, the continuum luminosity decreased by a factor of 100 and broad lines disappeared between 2006−2013 (Denney et al., 2014). The MUSE spectrum obtained by Raimundo et al. (2019) in October, 2017 showed strong broad Balmer component confirming the re-appearance of BLR and the transition of Mrk 590 from Type 2 to Type 1 AGN. Our Subaru spectrum obtained on October 27, 2018 showed both Hβ and Hα lines with FWHM of 10390 ± 1718 km s^{-1} and 6478 ± 240 km s^{-1}, respectively. Using our measured Hα BLR size of $21.44^{+1.49}_{-2.11}$ light-days and FWHM from the Hα line obtained from the single epoch spectrum, the black hole mass is found to be $1.96 \times 10^8\,M_\odot$ using virial relation and adopting a scale factor of 1.12. On the other hand, using the relation given by Woo et al. (2015), the black hole mass from the single-epoch spectrum is found to be $(1.59 \pm 0.14) \times 10^8\,M_\odot$ again based on the Hα line. Both the black hole masses are consistent with each other. Comparing the black hole mass of $4.75 \pm 0.74 \times 10^7$ M$_\odot$ measured by Peterson et al. (2004), our measurement

is a factor ~ 4 larger, which is due to the increase in the line width of the broad Balmer component by a factor of ~ 2.

3.3 SUMMARY

In this thesis we present the first time photometric RM observations on the source Mrk 590, which is a changing look AGN using observations carried out in the optical in broad B and R filters and narrow Hα and S II bands. The results of the work are summarized below:

1. We found a prominent host-galaxy contribution in the observed images in all of those three bands. The host-galaxy contributions were removed using GALFIT for B, R, Hα and S II-band. The host-corrected luminosity of the AGN in B, R, narrow Hα and S II bands are logL_{AGN} = 43.36 ± 0.01, 43.53 ± 0.01, 42.81 ± 0.06 and 43.71 ± 0.01 erg s^{-1}, respectively.

2. All the light curves show significant flux variations, which enabled us to carry out time series analysis to estimate BLR size of Mrk 590. We constructed Hα line light curve using different methods. We corrected the continuum contamination in narrow S II-band (1) using the observed narrow Hα-band data, which traces the continuum close to S II-band and (2) considering a fixed PL slope of $\alpha = 1/3$ to the observed B-band data. We found no difference in the measured lags between method 1 and 2 using CCF analysis.

3. The broad R-band data also contains Hα line flux. We removed the continuum flux in the observed R-band by extrapolating the continuum measured in the B-band and assuming a α value of 1/3. We found a lag of $\sim$16 days between the B-band light curve and the continuum subtracted R-band light curve. The lower value of lag is due to the

larger contribution of AGN continuum to the broad R-band than the narrow S II band.

4. Our estimated BLR size based on Hα line is $21.44^{+1.49}_{-2.11}$ days, which is equivalent to $0.018^{+0.001}_{-0.002}$ pc. The Hα BLR size of Mrk 590 is consistent with the best-fit size-luminosity relation of AGN.

5. The Subaru spectrum showed strong Hβ and Hα lines with FWHM of 6478 ± 240 and 10390 ± 1718 km s^{-1}, respectively, suggesting the transition of Mrk 590 from Type 2 (in 2006 $-$ 2013) to Type 1 (in 2017 $-$ 2019). The black hole mass measured from the single-epoch Subaru spectrum is found to be $1.96^{+0.15}_{-0.21} \times 10^8\,M_\odot$.

6. The size of the BLR in Mrk 590 determined in this work is found to be comparable to the inner radius of the dust torus determined from the lag between optical V and NIR K-band by Kokubo & Minezaki (2020) due to (a) the DRM observations reported by Kokubo & Minezaki (2020) were carried out during the period 2003 $-$ 2007 when the source was in faint state. Therefore, the drastic drop in the ionizing continuum radiation from the accretion disk can cause the dust particles to exist nearer to the BLR region making the torus size comparable to the BLR size. According to Kokubo & Minezaki (2020), after the drastic decrease in accretion disk luminosity, dust replenishment is attained by formation of new dust grains in the BLR/innermost dust torus region, and (b) the distribution of the dust particles in the torus region is not uniform as picturized in the Unification scheme of AGN and may change over the time. Because of the presence of a clumpy dust torus (Stalevski et al., 2013), the obscuration of ionizing continuum by the torus will also vary over time which may cause the torus to lie close to the BLR at certain epoch of time. Clumpy dust torus can

even play an important role in making an AGN to appear as changing-look AGN because of varying obscuration of the emission line from the BLR along the line of sight over time.

Chapter 4

DUST REVERBERATION OF H0507+164 AND Z229−15 [2]

This chapter presents the results of the dust reverberation observations carried out on two AGN, namely H0507+164 and Z229−15.

H0507+164:

This is a local Seyfert 1.5 galaxy at redshift z = 0.018 with RA = 05:10:45.5 and DEC = +16:29:56. It has optical g band brightness of 10 mag from the SIMBAD database with a black hole mass of $9.62^{+0.33}_{-3.73} \times 10^6\,M_\odot$ deduced from spectroscopic RM by Stalin et al. (2011).

Z229−15:

This a local Seyfert 1 galaxy at redshift z = 0.027 with RA = 19:05:25.94 and DEC = +42:27:39.76. It has a *Gaia* G magnitude of 16.44 mag. The central black hole mass of Z229−15 is $1.00^{+0.19}_{-0.24} \times 10^7\,M_\odot$ obtained from spectro-photometric RM by Barth et al. (2011).

4.1 ANALYSIS

4.1.1 Light curves and Flux variability

The final light curves for H0507+164 (corrected for accretion disk contribution to the NIR fluxes) in the optical and NIR bands are shown in Fig. 4.1. Similarly, we show in Fig. 4.2 the final optical (corrected for host galaxy contamination) and NIR (corrected for accretion disk contribution) light curves of Z229−15.

To characterize the variability nature of the sources, we used the normalised excess variations outlined in Chapter 3. In addition to F_{var}, we also calculated R_{max}, which is the ratio of the maximum to the minimum flux in the light curves. The results of the flux variability analysis of H0507+164 and Z229−15 are given in Table 4.1 and Table 4.2, respectively. In the case of H0507+164, F_{var} in the optical V-band is larger than that in the NIR K_s

[2]The contents of this chapter are published in Mandal et al. (2018, 2019, 2021c)

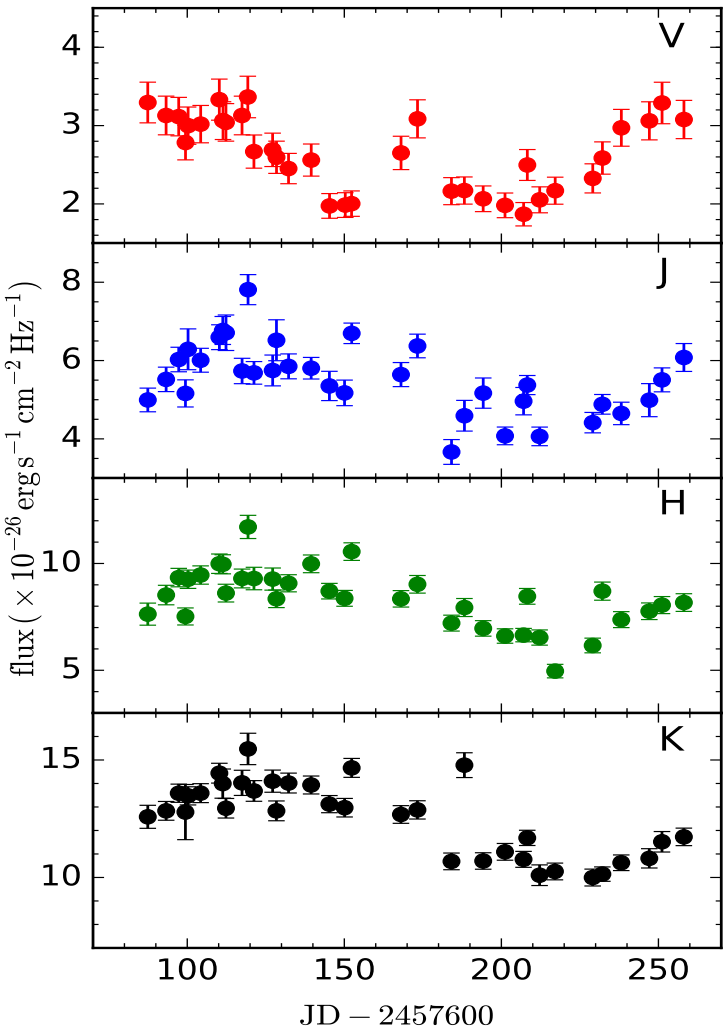

Figure 4.1: The light curves of H0507+164 in optical V and NIR J, H and K_s-bands during the period from October, 2016 to February, 2017. The NIR light curves were corrected for the accretion disk contamination.

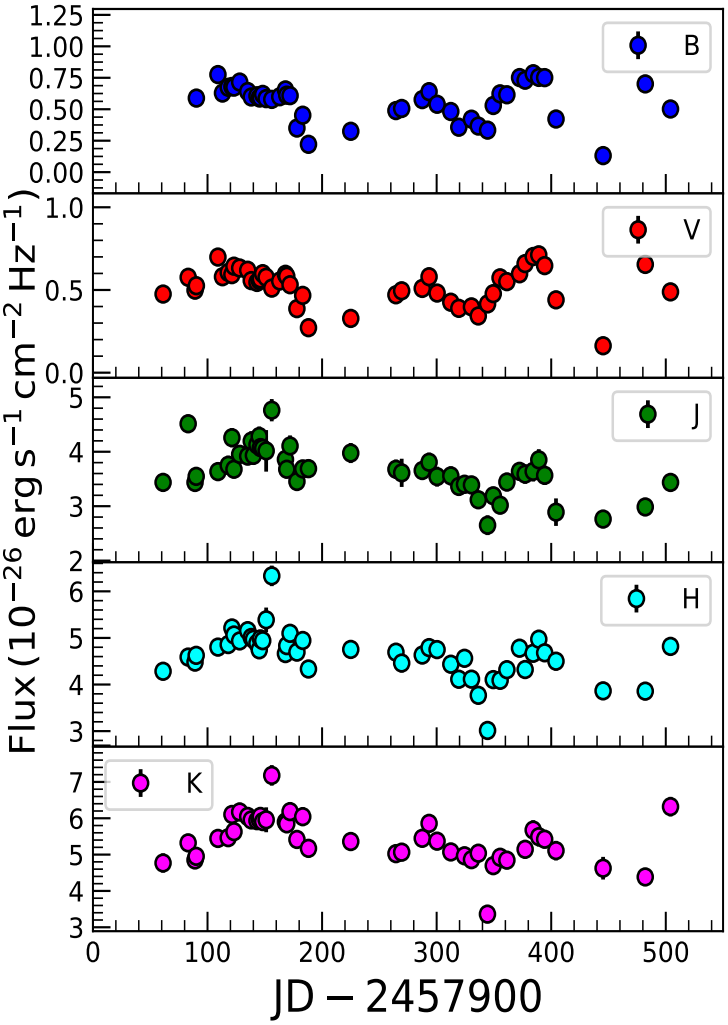

Figure 4.2: The light curves of Z229−15 in optical B, V and NIR J, H, K_s bands during the period from July, 2017 to December, 2018. All the NIR light curves were corrected for the accretion disk contamination using α measured at individual epoch.

Table 4.1: Results of the variability analysis of H0507+164 light curves in the observer's frame. The mean values of fluxes ($\bar{f}$) in various bands with their standard deviations σ are in units of $10^{-26}\,\mathrm{erg\,s^{-1}\,cm^{-2}\,Hz^{-1}}$. λ_{eff} represents the effective wavelength in Angstroms.

Filter	$\lambda_{\rm eff}$	$\bar{f}$	σ	$F_{\rm var}$	$R_{\rm max}$
V	5448	2.66	0.48	0.159 ± 0.005	1.801
J	12200	5.56	0.89	0.149 ± 0.003	2.131
H	16300	8.39	1.36	0.154 ± 0.002	2.360
K_s	21900	12.56	1.56	0.119 ± 0.001	1.548

band. Thus, there is a wavelength dependent variability. In the case of Z229−15, there is a decrease in the amplitude of variations gradually from the optical to the NIR bands.

Recently, Sánchez et al. (2017) found an anti-correlation between the amplitude of variability and wavelength based on the analysis of NIR variability of a large sample of AGN. Also, according to Enya et al. (2002), the amplitude of NIR variations is expected to be smaller compared to the optical bands. Though our data of H0507+164 do not reveal a clear anti-correlation of variability amplitude with wavelength, Z229−15 clearly showed a wavelength dependent variability amplitude as found by Sánchez et al. (2017) and Enya et al. (2002).

Table 4.2: Results of the variability analysis of Z229−15 light curves in the observer's frame. The mean values of fluxes ($\bar{f}$) in various bands with their standard deviations σ are in units of $10^{-26}\,\mathrm{erg\,s^{-1}\,cm^{-2}\,Hz^{-1}}$. λ_{eff} represents the effective wavelength in Angstroms.

Filter	λ_{eff}	$\bar{f}$	σ	F_{var}	R_{max}
B	4363	0.56	0.15	0.263 ± 0.000	5.953
V	5448	0.53	0.11	0.213 ± 0.000	4.374
J	12200	3.66	0.43	0.106 ± 0.002	1.797
H	16300	4.64	0.50	0.100 ± 0.002	2.101
K_s	21900	5.46	0.61	0.102 ± 0.002	1.905

4.2 CCF ANALYSIS TO FIND THE LAG BETWEEN OPTICAL AND NIR VARIATIONS

4.2.1 H0507+164

We used both DCF and ICCF to estimate the time lag between the optical and the NIR flux variations for H0507+164. The details of CCF analysis are mentioned in Section 3.1.2. We calculated the centroid of the CCF by considering all the points that are within 60% of the maximum of the CCF. The 60% cut off for H0507+164 was selected to have sufficient cross-correlation coefficients for the centroid determination. The CCFs of H0507+164 are shown in Fig. 4.3.

To calculate the lag and the associated error, we carried out Monte Carlo simulation as detailed in Section 3.1.2. The results of the correlation analysis calculated for different bin sizes are given in Table 4.3. The ICCF lags are found to agree well with the DCF values within uncertainties. For all further analysis, we consider the lag obtained using the DCF method

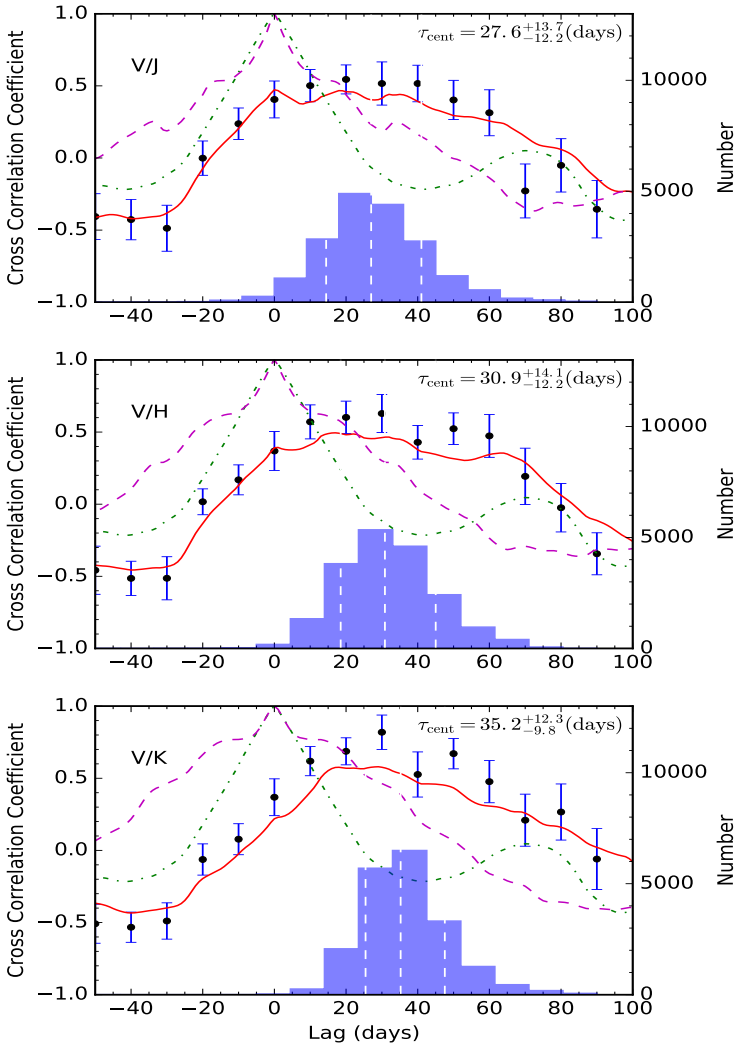

Figure 4.3: The CCFs of V vs. J (top), V vs. H (middle) and V vs. K_s (bottom) are shown for H0507+164. The solid line represents the ICCF, points with error bars are the DCF obtained using $\Delta\tau = 5$ days and the corresponding CCCD obtained using 20,000 Monte Carlo simulations is shown by the histogram at each panel. The dashed-dot line is the auto correlation function (ACF) of V -band light curve and the dashed line represents the ACF of corresponding NIR band light curve. The value of τ_{cent} calculated from Monte Carlo simulation is also noted at each panel.

Table 4.3: Values of τ_{cent} and their associated erros in days of H0507+164 as obtained by DCF (for various bin size ($\Delta\tau$)) and ICCF methods in observer's frame.

Bands	DCF ($\Delta\tau$ in days)					ICCF
	2	3	4	5	6	
$V-J$	$31.1^{+16.5}_{-15.0}$	$28.6^{+15.4}_{-13.8}$	$28.0^{+15.1}_{-12.2}$	$27.6^{+13.7}_{-12.2}$	$27.3^{+15.1}_{-12.0}$	$20.7^{+13.5}_{-11.0}$
$V-H$	$33.9^{+17.4}_{-14.8}$	$32.0^{+15.4}_{-13.6}$	$32.8^{+15.7}_{-14.0}$	$30.9^{+14.1}_{-12.2}$	$31.9^{+13.6}_{-12.6}$	$25.1^{+12.4}_{-11.0}$
$V-Ks$	$39.2^{+14.9}_{-12.3}$	$37.6^{+13.1}_{-11.1}$	$36.7^{+12.9}_{-10.7}$	$35.2^{+12.3}_{-9.8}$	$36.3^{+12.1}_{-10.7}$	$30.2^{+9.0}_{-7.9}$

with a bin size of $\Delta\tau$ = 5 days, as the typical sampling of the light curves is about 5 days. Based on the above mentioned approach, we found the redshift corrected rest frame time lags of $27.1^{+13.5}_{-12.0}$ days between V and J bands, $30.4^{+13.9}_{-12.0}$ days between V and H bands and $34.6^{+12.1}_{-9.6}$ days between V and K_s bands. Though there is an indication that the lag increases with wavelength, because of the larger uncertainties, we conclude that within errors, the obtained lags are consistent with each other. The lag between V and K_s band defines the inner radius of the dust torus that corresponds to the dust sublimation radius. Therefore, we used the rest frame lag between V and K_s band of $34.6^{+12.1}_{-9.6}$ days to estimate the inner size of the dust torus in H0507+164. This lag is found to be larger than the lag of $3.01^{+0.42}_{-1.84}$ days obtained between the optical and Hβ emission line flux variations from optical spectroscopic monitoring observations by Stalin et al. (2011) as expected from the unification model of AGN. We conclude that the inner edge of the dusty torus is at a distance of $\sim 0.029^{+0.010}_{-0.008}$ pc from the central UV/optical AGN continuum source emitting radiation in V-band.

4.2.2 Z229−15

For Z229−15 we used all the points that are within 80% of the maximum of the CCF to calculate τ_{cent}. The Monte Carlo simulation based on RSS and FR was repeated 5000 times and the centroid of the lag was obtained each time. We then constructed CCCD and cross-correlation peak distribution (CCPD). The CCCDs obtained from the ICCF method are shown in Fig. 4.4 and Fig. 4.5. As the typical sampling of our multi-band light curves is $\sim$ 5 days, a time bin ($\Delta\tau$) of 5 days was used for CCF analysis. We represent the DCF by blue filled circles and ICCF by red solid line obtained between the optical B and V bands in Fig. 4.4. The CCF peaks at zero lag, which is expected as both the optical B and V band radiation are coming from almost similar regions from the accretion disk. Similarly, for the three other filter combinations, namely V/J, V/H and V/K_s bands, the CCFs obtained using both the ICCF and DCF methods, are shown in Fig. 4.5. The CCFs peak at a lag different from zero, and also, the pattern of the CCFs obtained by both the ICCF and DCF are found to be similar. The results obtained from the CCF analysis are mentioned in Table 4.4. We found consistent centroid lags using both ICCF and DCF considering their uncertainties. However, for all further analysis, we consider the CCCD lags calculated from the ICCF method as it gives comparatively smaller uncertainties than the DCF method (see Table 4.4).

The rest frame time lag of Z229−15 between V and K_s is found to be $20.36^{+5.82}_{-5.68}$ days, while we found rest frame time lags of $15.63^{+5.05}_{-5.11}$ days and $12.52^{+10.00}_{-9.55}$ days between V and H and V and J, respectively. There is a hint that the obtained lag between V and K_s band is larger than V and H, which is larger than V and J. However, the uncertainties are too large to unambiguously argue for the presence of wavelength dependent

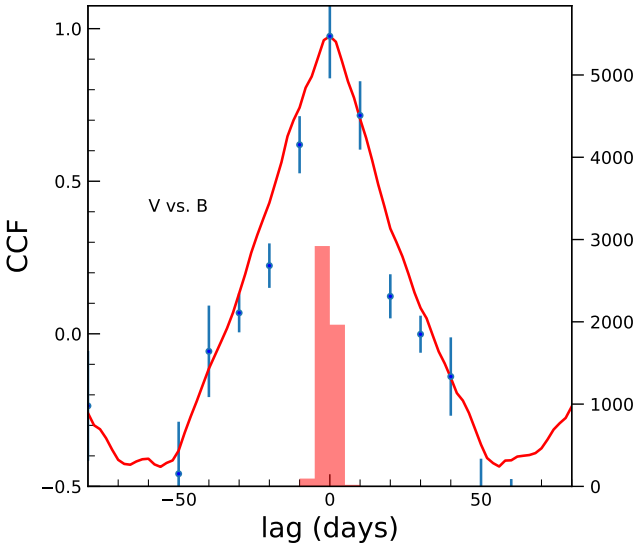

Figure 4.4: CCF between V and B band. The solid red line is the ICCF and points with error bars represent the DCF. The distribution of τ_{cent} obtained from ICCF is also shown.

lag. We conclude that the lags measured between different wavelengths are consistent with each other. The rest frame lag between V and K_s band of $20.36^{+5.82}_{-5.68}$ days was used to infer the inner edge of the dust torus of Z229−15, which is found to be at a distance of 0.017 ± 0.005 pc from the central ionizing continuum source.

We also checked for the presence of any correlated errors in the light curves on the CCF analysis for H0507+164 and Z229−15. The dependencies of the errors in fluxes in the K_s-band as a function of the errors in the V-band are shown for H0507+164 (top panel) and Z229−15 (bottom panel) in Fig. 4.6. For H0507+164 linear least squares fit to the data gave a Pearson correlation coefficient of r = 0.252 with a p-value of 0.144. Similarly, for Z229−15, linear least squares fit to the errors in K and V-band gave a Pearson correlation coefficient of r = −0.172 with a p-value of 0.264. So, the effect of the correlated error is negligible on the CCF analysis for H0507+164 and Z229−15.

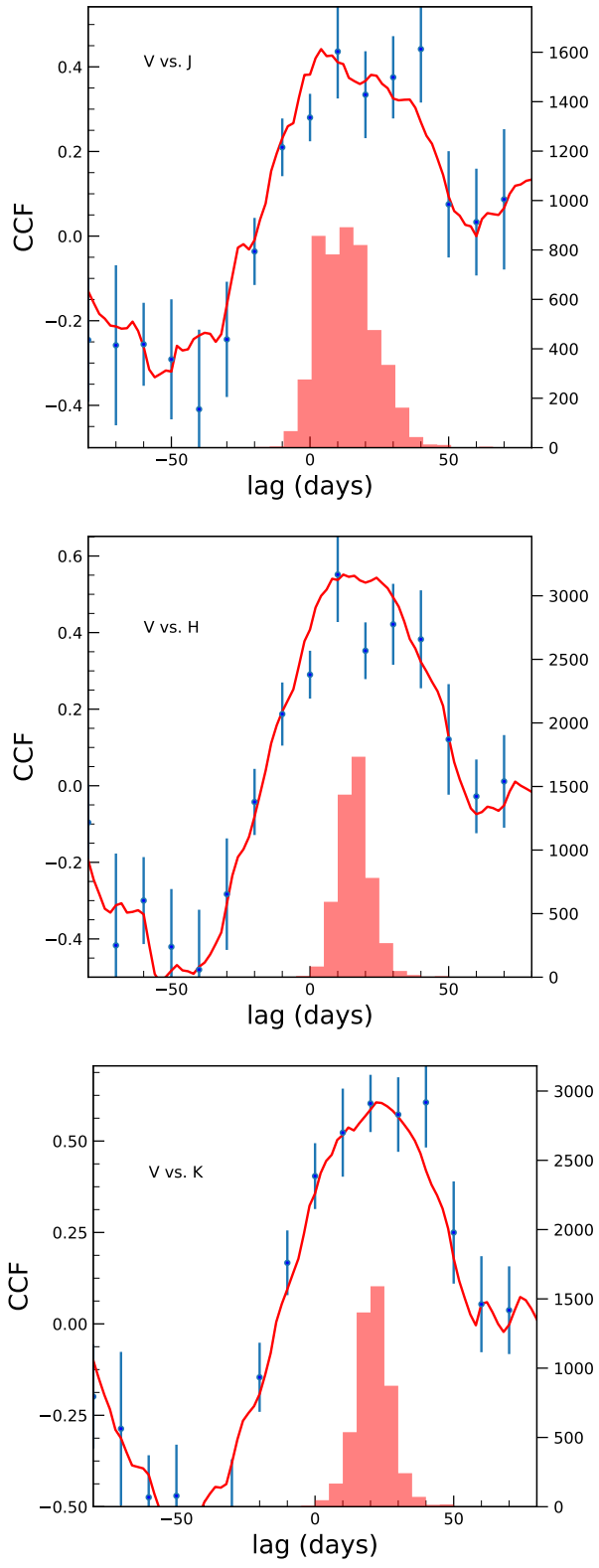

Figure 4.5: The CCFs between V and J (top panel), V and H (middle panel), and V and K_s (bottom panel) are shown. The solid red line is the ICCF and the points with error bars are the DCF. The distribution of τ_{cent} obtained from ICCF method is also shown in each panel.

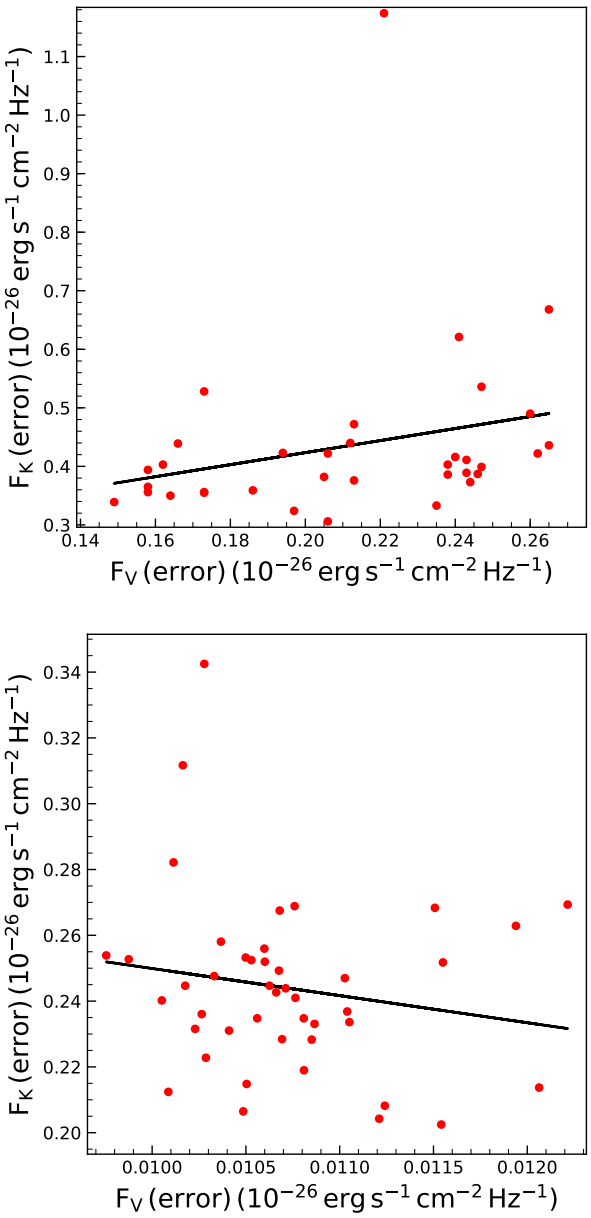

Figure 4.6: Dependency of the errors in the fluxes between V and K_s-bands for H0507+164 (top) and Z229−15 (bottom). The black lines represent the best fit lines.

Table 4.4: Median values of time delays with errors in days of Z229−15 from the CCCDs obtained using DCF and ICCF and CCPD from ICCF in the observer's frame.

Band	DCF	ICCF	CCPD from ICCF
		varying α	
V − B	$-0.24^{+3.90}_{-4.39}$	$-0.87^{+1.94}_{-2.00}$	$0.00^{+0.00}_{-2.00}$
V − J	$22.33^{+16.58}_{-15.16}$	$12.86^{+10.27}_{-9.81}$	$10.00^{+14.00}_{-8.00}$
V − H	$18.16^{+14.55}_{-9.91}$	$16.06^{+5.19}_{-5.25}$	$14.00^{+12.00}_{-6.00}$
V − K_s	$25.42^{+13.49}_{-14.88}$	$20.92^{+5.98}_{-5.84}$	$22.00^{+6.00}_{-10.00}$
		constant $\alpha = 0.1$	
V − J	$34.01^{+11.99}_{-14.76}$	$27.96^{+7.07}_{-8.73}$	$28.00^{+8.00}_{-8.00}$
V − H	$9.67^{+11.07}_{-12.19}$	$26.14^{+5.85}_{-5.12}$	$26.00^{+6.00}_{-4.00}$
V − K_s	$34.80^{+8.69}_{-12.93}$	$30.86^{+6.22}_{-4.95}$	$30.00^{+8.00}_{-4.00}$

4.3 DISCUSSION

The inner edge of the dust torus in AGN is represented by the lag obtained between the optical V band coming from the accretion disk and the NIR K_s band from the torus as the temperature of the dust at the wavelength of K_s band is close to the sublimation temperature of dust particles (Almeyda et al., 2017). As of today, DRM observations based on monitoring in the optical V band and NIR K band have been used to find the inner radius of the dust torus in about 40 AGN. A majority of those measurements come from the Multicolor Active Galactic Nuclei Monitoring (MAGNUM) project that includes 17 Seyfert 1 galaxies (Koshida et al., 2014) and 22 quasars (Minezaki et al., 2019) and few sources are from other campaigns (Pozo Nuñez et al., 2014, 2015; Ramolla et al., 2018; Mandal et al., 2018, 2021c).

4.3.1 Correlation between the infrared lag and optical luminosity

Barvainis (1987) and Koshida et al. (2014) found that the size of the torus is correlated with the optical luminosity of the accretion disk as $R_{\rm torus} \propto L^{0.5}$. We show in Fig. 4.7 the correlation between the $R_{\rm torus}$ measured from K band DRM lags against their optical luminosity taken from literature (Koshida et al., 2014; Mandal et al., 2018; Minezaki et al., 2019). In the same figure, we represent the linear regression relation of $R_{\rm torus} \propto L^{0.424}$ (Minezaki et al., 2019) by dashed black line and $R_{\rm torus} \propto L^{0.5}$ (Koshida et al., 2014) by dashed red line. Our object H0507+164 for which we used a constant $\alpha = 1/3$ to correct for the AD contamination in the observed NIR fluxes, is shown by the blue triangular point in the lag−luminosity plane. Our obtained dust lag in H0507+164 is in excellent agreement with that expected from its optical luminosity at V-band and closely follows the dust lag−optical luminosity correlation of $\rm R_{torus} \propto L^{0.5}$. The other source Z229−15 is shown as a filled red circle in the same Figure. Our measured lag on the Z229−15 is found to deviate from the linear regression line obtained by Minezaki et al. (2019). This deviation could be because of the adoption of variable α in our work to correct for the contamination of the AD to the observed NIR fluxes. We used α determined at each epoch from the near simultaneous observations between optical B and V band, while for the lags measured for the other sources in Fig. 4.7, the corresponding authors used a constant α to correct for the contribution of the AD to the observed NIR fluxes. Kishimoto et al. (2008) found that the power law continuum of quasar accretion disk can extend up to NIR with a shape given as $F_\nu \propto \nu^{1/3}$. AGN show flux variations in the optical and NIR bands with different amplitude of flux variations across wavelengths. Therefore, in addition to variations in fluxes, AGN are also known to show spectral

variation (Tomita et al., 2006; Kishimoto et al., 2008) over time. Hence, the assumption of a constant α from optical to NIR to correct for the AD contamination to the observed IR emission might not be proper. In spite of that, we reanalysed the NIR light curves by adopting a constant $\alpha = 0.1$ as prescribed by Minezaki et al. (2019). By this, we found a lag of $30.04^{+6.05}_{-4.82}$ days between V and K_s band in the rest frame of the source Z229−15 as shown by the red square point, which lies closer to the linear regression lines of Koshida et al. (2014) and Minezaki et al. (2019) in Fig. 4.7. This lag of $30.04^{+6.05}_{-4.82}$ days is equivalent to a distance of $0.025^{+0.005}_{-0.004}$ pc.

In Fig. 4.7, $R_{\rm torus}$ is related to the optical luminosity at V-band with an index of about 0.5 (ie. $R_{\rm torus} \propto L^{0.5}$), though, there is scatter. The scatter present in the $R_{\rm torus} - L$ relation might come from various factors (cf. Minezaki et al. 2019), such as (a) adaptation of a constant α to subtract the AD component in the observed NIR light curves, (b) effect of viewing angle on the measured lag (Kawaguchi & Mori, 2011; Barvainis, 1992), (c) the effect of accretion rate on the estimated lag and (d) the distribution of the dust in the torus and how it is illuminated by the central ionizing source (Almeyda et al., 2020). Koshida et al. (2014) could not find systematic changes in the dust lag with the viewing angle and the accretion rate by analysing the residuals of the dust lag from the best fit linear regression. Similarly, optical reverberation studies aimed to find the BLR size too found a linear correlation between the BLR radius and the luminosity at 5100 Å with a power law index close to 0.5. However, from an analysis of the light curves obtained for the SEAMBH program, Du et al. (2016) found systematically shortened BLR size for objects with high accretion rate. Their slope of $R_{\rm BLR} \propto L^{0.33}$ is found to be much shallower than the slope of 0.533 found by Grier et al. (2013a). Based on this observational finding, it is likely that the accretion rate in an AGN should also have an influence on the derived

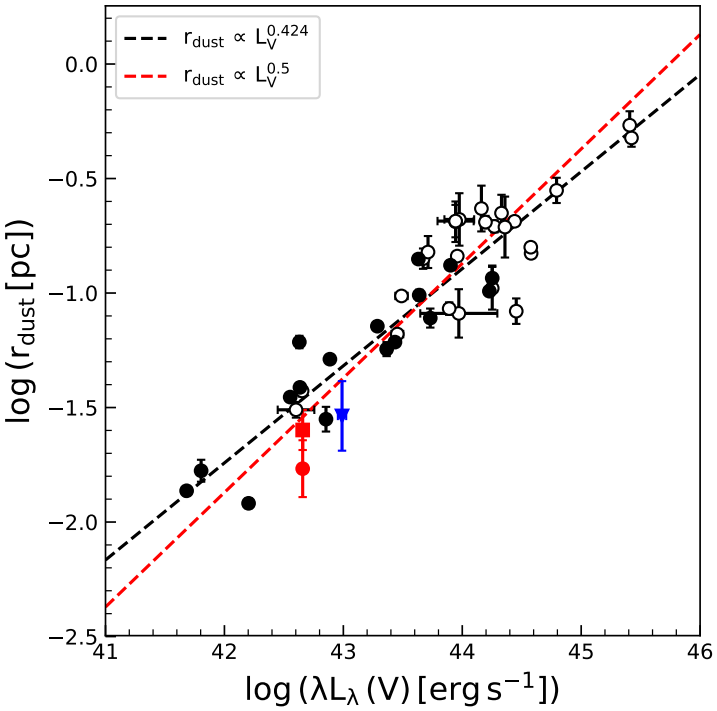

Figure 4.7: Dust lag − luminosity plot. The lags are in the rest frame of the sources. The empty and filled black circles are the objects from Minezaki et al. (2019) and Koshida et al. (2014), respectively, triangular blue point shows the object H0507+164, the red circle and square points correspond to the lag of Z229−15 from our DRM observations for α obtained from observations measured at individual epoch and a constant $\alpha = 0.1$, respectively.

dust lag obtained from DRM. We need more homogeneous analysis on a larger number of quasars to arrive at a firm conclusion of the dependence of $R_{\rm torus}$ on accretion rate.

4.3.2 Structure of the BLR and the Dust Torus

Stalin et al. (2011) estimated BLR size of H0507+164 of $3.01^{+0.42}_{-1.84}$ days in the rest frame of the object from spectroscopic RM observations of BLR based on the lag between the optical/UV continuum and the Hβ line emission. Our findings from the DRM observations on the same object at different NIR wavelengths together with the result obtained by Stalin et al. (2011) provide important information about the structure of the BLR and the dust torus of H0507+164. The dust-lag between V -band and K_s-band is found to be larger than the BLR lag as expected from the Unified scheme of AGN. Similarly, from spectro-photometric RM observations, Barth et al. (2011) found the BLR size in Z229−15 as $3.86^{+0.69}_{-0.90}$ days in the rest frame of the object based on the lag between V-band continuum variations and Hβ line. Our estimated dust lag is found to be larger than the BLR lag again satisfying the Unification model of AGN.

There are indications that the derived dust lag increases with wavelength in our multi-wavelength data acquired for H0507+164 and Z229−15. But considering the large uncertainties present in the estimated lags, the wavelength dependency of dust-lag is not statistically significant. Koshida et al. (2014) found that the dust-lag is about 4−5 times larger than the BLR radius from an analysis of a sample of 17 Seyfert galaxies and typically a factor of 2 smaller than their interferometric radius. Similarly, the BLR radius obtained from RM is found to be smaller than the same observed by NIR interferometry (Petrov et al., 2012). Such difference may arise as RM is a response weighted radius originating from the compact region, while

the interferometric radius is flux weighted and sensitive to the flux coming from the outer regions (Kishimoto et al., 2007). However, there are few exceptions, such as NGC 4151 (Bentz et al., 2006), NGC 4593 (Bentz et al., 2013) and Mrk 335 (Du et al., 2014), where the dust lag is found to be about 10 times larger than the BLR radius. We found about 11 times larger dust lag than the BLR lag in H0507+164 and a factor of about 5.3 times larger dust lag than the BLR lag in Z229−15. Such varied differences between the mean radius of the dust torus and BLR known in AGN indicate for variable dust emission (Koshida et al., 2009; Schnülle et al., 2015). To establish this, we need more measurements of the size of the dust torus for a large number of AGN.

4.4 SUMMARY

We carried out the first DRM observations on the sources H0507+164 and Z229−15 in the optical (V for H0507+164 and B, V for Z229−15) and NIR (J, H, K_s) bands. We accumulated near simultaneous photometric data for a total of 35 and 48 epochs during the period October, 2016 to April, 2017 and July, 2017 to December, 2018 for H0507+164 and Z229−15, respectively. The results are summarized below:

1. Both H0507+164 and Z229−15 showed flux variations in the observed optical and NIR bands. The variations between different bands are also found to be correlated during our observing period.

2. For H0507+164 we found a rest-frame lag of $27.1^{+13.5}_{-12.0}$ days between V and J bands, $30.4^{+13.9}_{-12.0}$ days between V and H bands and $34.6^{+12.1}_{-9.6}$ days between V and K_s bands. The rest-frame lags for Z229−15 are $12.52^{+10.00}_{-9.55}$ days between (V−J), $15.63^{+5.05}_{-5.11}$ days between (V−H) and $20.36^{+5.82}_{-5.68}$ days between (V−K_s). Because of the large error bars, the

presence of wavelength dependent lags if any could not be ascertained for both the sources, instead the lags between different wavelengths are consistent with each other.

3. We found that the inner edges of the dust torus in H0507+164 and Z229−15 are at a distance of $0.029^{+0.010}_{-0.008}$ pc and 0.017 ± 0.005 pc, respectively, from the central optical ionizing source.

4. The dust lags of 34.6 and 20.36 days obtained for H0507+164 and Z229−15 are found to be about a factor of 11.5 and 5.3 times larger than the BLR lag.

5. Positioning our sources in the known $R_{\rm torus} - L$ relation for a sample of about 40 DRM sources, we found H0507+164 to lie close to the best fit line, whereas, Z229−15 was found to lie below the expected $R_{\rm torus} - L$ relation. However, using a constant α of 0.1 to correct for the AD contamination in the NIR light curves (which is what is done for the objects in Fig. 4.7), we found Z229−15 to move closer to the known $R_{\rm torus} - L$ relation. But, we disfavour the usage of constant spectral index α in DRM studies, as α is known to vary with the brightness of the source.

Chapter 5

ESTIMATION OF THE SIZE AND STRUCTURE OF THE BROAD LINE REGION USING BAYESIAN STATISTICS [3]

RM observations that use the time delay between the continuum and emission line observations are routinely used to infer the size of the BLR and then the black hole mass assuming virial relationship. Those observations alone are not usable to infer the structure and kinematics of the BLR. However, using those observations along with theoretical models it is possible to infer the structure and kinematics of the BLR. One such theoretical model that uses the observed light curves to infer the properties of BLR is PBMAP (Parallel Bayesian code for reverberation−MAPping data, Li et al., 2013). In this chapter by collecting line and continuum data for a sample of 57 sources, as inputs to PBMAP, we derived the properties of a large sample of AGN. The details of the 57 sources are given in Table 2.2.

5.1 LIGHT CURVE RECONSTRUCTION: THE PBMAP CODE

The PBMAP code developed by Li et al. (2013) was used to perform the light curve modeling. We describe briefly the methodology adopted here. The observed continuum and line light curves collected from the literature were used in this code as input data. The code reconstructs the continuum light curve from irregularly sampled observed continuum light curve using the damped random walk model (DRW; Kelly et al. 2009) following a Bayesian approach. Many previous investigations available in the literature suggest that the AGN optical flux variations can be well explained by DRW (e.g., Kozłowski et al., 2010; MacLeod et al., 2010; Zu et al., 2011).

We modeled the AGN continuum variability as a random process, where the co-variance matrix S of the signal can be written as

$$S(t_i - t_j) = \sigma_d^2 exp\left[-\left(\frac{|t_i - t_j|}{\tau_d}\right)^{\alpha}\right] \tag{5.1}$$

Here, t_i and t_j represent the two epochs, whereas the co-variance func-

[3]The contents of this chapter are published in Mandal et al. (2021b)

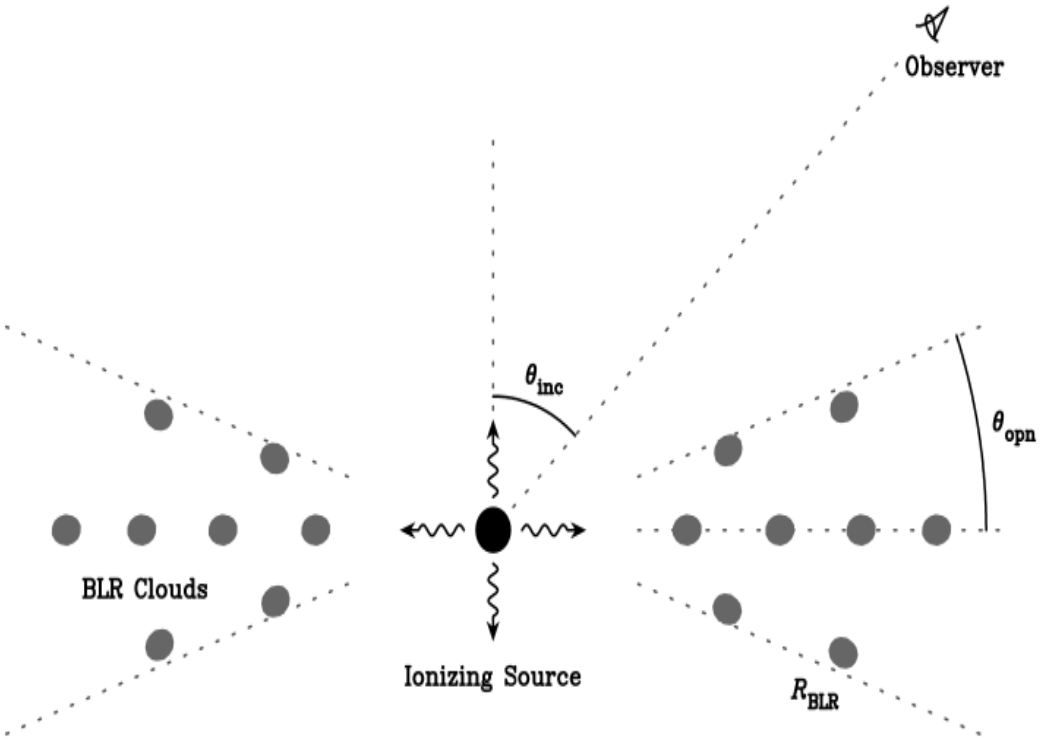

Figure 5.1: A diagram of the BLR chracterized by a flexible disk-like geometry with an inclination angle $\theta_{\rm inc}$ to the observer along the line of sight and an opening angle $\theta_{\rm opn}$ (Li et al., 2013) . A point like central ionizing source producing isotropic UV/optical emission illuminates the surrounding BLR clouds.

tion depends on the difference in time $t_i - t_j$, τ_d and σ_d are the damping timescale and standard deviation of variation and α is the smoothening parameter. α is fixed to unity in the model calculation as it is shown to be sufficient for variability (Kelly et al., 2009). In the next step, the code reconstructs the line light curve using a BLR model. In the code (a) the BLR is modeled considering BLR to be an axisymmetric disk composed of a large number of discrete, point-like clouds of equal density, that re-radiate the UV/optical ionizing continuum as emission lines, (b) the BLR clouds subtend a solid angle defined by the opening angle (θ_{opn}), whereas the BLR is viewed at an inclination angle (θ_{inc}) and (c) the central ionizing source is point like, thereby producing isotropic radiation. The disk-like structure of BLR assumed in this model is depicted in Fig. 5.1. The model regenerates the velocity integrated line light curve as given below

$$f_l(t) = A \int \Psi(\tau) f_c^{(1+\gamma)}(t-\tau) d\tau \tag{5.2}$$

with the transfer function

$$\psi(\tau) = \sum_i \delta(\tau - \tau_i) w_i \left(\frac{I_i}{R_i^2} \right)^{1+\gamma} \tag{5.3}$$

where τ_i is the time lag from the i^{th} cloud at a distance R_i from the central source, A denotes the response coefficient, w_i represents the weight of the cloud to the response of the ionizing continuum, I_i takes care of any possible anisotropic effects and deviations from the continuum, and γ represents the non-linearity of the line response to the continuum. The weight w_i is fixed to unity and I_i is neglected in all calculations considering emitting radiation to be isotropic. A value of $\gamma = 0$ signifies a linear response of BLR to the ionizing continuum variations. To determine the quality of the

generated light curves, the reduced χ^2 value (χ^2/dof), which is defined in Li et al. (2013) is used.

A detrending to the original light curves was applied when the value of χ^2/dof was large (> 1.5) before subjecting them to model fits. The detrending, which was done by subtracting a first-order polynomial fit to the original light curve as mentioned in Li et al. (2013), led to an improvement in the results which has also been noticed by Li et al. (2013). We noticed that for 6 objects, namely J0652+744, J1242+332, J1416+539, J1418+539, J1421+525 and J2303+088 though χ^2/dof is found to be slightly larger after detrending, we obtained better estimates of BLR size with smaller uncertainty.

5.2 RESULTS AND DISCUSSIONS

5.2.1 Study of flux variability

AGN are known to show flux variability over the entire electromagnetic spectrum and their optical flux variability has been found to correlate with many of their physical properties. Most of these studies are from photometric monitoring observations, however, in such studies, broad emission lines too can contaminate the photometric pass band, specifically if broad band filters are used for tracing the continuum. Spectroscopic monitoring observations can overcome these difficulties, however, it is time consuming. A dataset fulfilling such criteria is the one accumulated for RM studies. Though, the line and continuum light curves retrieved from RM observations and used in this work are primarily aimed to understand the BLR, it is also a good asset to investigate AGN variability. Having both continuum and line light curves, we defined the line and continuum variability of our sample by F_{var} (Edelson et al., 2002; Vaughan et al., 2003) and elaborated

Table 5.1: Result of the variability analysis. The median values of the SNR of the light curves are mentioned.

	α_{2000}	δ_{2000}	F_{var}		R		span (Δt)(days)		δt_{mean}(days)		SNR	SNR
No			continuum	line	continuum	line	continuum	line	continuum	line	continuum	line
1	00:10:31.01	+10:58:29.5	0.109	0.102	1.482	1.442	137.79	127.28	0.67	1.61	64	36
2	02:30:05.52	-08:59:53.2	0.062	0.042	1.438	1.283	116.75	116.75	1.54	1.54	169	266
3	06:52:12.32	+74:25:37.2	0.130	0.097	1.667	1.399	138.85	117.86	0.68	1.25	128	65
4	11:39:13.92	+33:55:51.1	0.085	0.093	1.510	1.500	146.79	146.79	4.45	4.45	68	72
5	12:42:10.61	+33:17:02.7	0.058	0.048	1.260	1.284	146.71	146.71	2.93	2.93	131	98
6	13:42:08.39	+35:39:15.3	0.071	0.171	1.337	1.841	47.01	47.01	1.62	1.62	164	290
7				0.164		1.909	47.01	47.01	1.62	1.62	164	983
8	14:05:18.02	+53:15:30.0	0.021	0.059	1.171	1.586	206.74	176.98	0.64	5.71	139	17
9				0.049		1.490	206.74	173.00	0.64	5.77	139	18
10	14:05:51.99	+53:38:52.1	0.024	0.046	1.421	1.449	206.75	173.00	0.66	5.77	53	21
11	14:07:59.07	+53:47:59.8	0.049	0.126	1.217	1.713	176.98	176.98	5.71	5.71	987	70
12	14:08:12.09	+53:53:03.3	0.026	0.103	1.359	1.639	195.03	176.98	0.94	5.71	158	28
13			0.022	0.056	1.144	1.363	206.75	173.00	0.79	5.77	90	22
14	14:09:04.43	+54:03:44.2	0.114	0.130	1.696	2.135	206.74	176.98	0.92	5.71	37	15
15	14:09:15.70	+53:27:21.8	0.030	0.059	1.180	1.337	206.75	173.00	0.50	5.77	148	26
16	14:10:04.27	+52:31:41.0	0.012	0.032	1.142	1.197	206.74	176.98	0.63	5.71	143	35
17			0.012	0.019	1.142	1.313	206.74	173.00	0.63	5.77	143	20
18	14:10:18.04	+53:29:37.5	0.064	0.170	1.482	2.097	176.98	176.98	5.71	5.71	211	21
19			0.023	0.039	1.222	1.384	206.75	176.98	0.42	5.71	63	15
20			0.023	0.037	1.222	1.381	206.75	173.00	0.42	5.77	63	19
21	14:10:31.33	+52:15:33.8	0.037	0.164	1.391	2.449	206.74	176.98	0.90	5.71	57	16
22	14:10:41.25	+53:18:49.0	0.070	0.121	2.014	1.645	195.02	176.98	0.77	5.71	23	51
23			0.070	0.050	2.014	1.241	195.02	173.00	0.77	5.77	23	75
24	14:11:12.72	+53:45:07.1	0.030	0.044	1.128	1.261	176.98	176.98	6.32	6.32	386	60
25	14:11:15.19	+51:52:09.0	0.035	0.046	1.434	1.226	195.01	176.98	0.77	5.71	31	43
26			0.030	0.079	1.253	4.246	206.74	173.00	0.63	5.77	49	7
27	14:11:23.42	+52:13:31.7	0.072	0.125	1.356	1.561	195.01	176.98	0.95	5.71	40	33
28			0.071	0.065	1.515	1.286	206.79	173.00	0.66	5.77	41	49
29	14:11:35.89	+51:50:04.5	0.055	0.067	2.003	3.174	195.07	176.98	0.51	5.71	14	6
30	14:12:14.20	+53:25:46.7	0.028	0.112	1.130	1.753	176.98	176.98	5.71	5.71	852	69
31	14:12:53.92	+54:00:14.4	0.055	0.136	1.232	1.912	176.98	176.98	5.90	5.90	446	22
32	14:13:14.97	+53:01:39.4	0.045	0.149	4.060	2.769	195.06	176.98	0.59	5.71	6	7
33	14:13:18.96	+54:32:02.4	0.048	0.041	1.408	1.294	191.86	176.98	0.66	5.71	64	29
34	14:13:24.28	+53:05:27.0	0.029	0.055	1.250	1.298	195.06	176.98	0.79	5.71	60	29
35			0.029	0.098	1.203	1.440	206.75	173.00	0.69	5.77	134	38
36	14:14:17.13	+51:57:22.6	0.094	0.120	1.414	1.553	176.98	176.98	6.10	6.10	79	25
37			0.032	0.406	3.880	8.170	195.07	176.98	0.82	5.71	8	4
38	14:15:32.36	+52:49:05.9	0.114	0.091	3.890	1.769	195.06	176.98	0.71	5.71	13	20
39	14:16:25.71	+53:54:38.5	0.068	0.037	1.270	1.173	176.98	176.98	5.90	5.90	792	152
40			0.053	0.010	1.290	1.104	206.75	173.00	1.02	5.77	84	54
41	14:16:44.17	+53:25:56.1	0.044	0.095	1.165	1.550	176.98	176.98	5.90	5.90	301	30
42	14:16:45.15	+54:25:40.8	0.072	0.282	1.308	3.842	176.98	176.98	5.71	5.71	440	21
43			0.041	0.138	1.281	1.751	206.82	173.00	0.54	5.77	93	16

	α_{2000}	δ_{2000}	F_{var}		R		span (Δt)(days)		δt_{mean}(days)		SNR	SNR
No			continuum	line	continuum	line	continuum	line	continuum	line	continuum	line
44	14:16:45.58	+53:44:46.8	0.076	0.141	1.628	1.944	176.98	176.98	5.71	5.71	270	21
45			0.025	0.031	1.198	1.434	206.82	173.00	0.53	5.77	76	15
46	14:16:50.93	+53:51:57.0	0.037	0.106	1.160	1.566	176.98	176.98	5.90	5.90	181	37
47	14:17:06.68	+51:43:40.1	0.038	0.045	1.142	1.217	176.98	176.98	5.71	5.71	473	57
48	14:17:12.30	+51:56:45.5	0.115	0.348	12.431	5.887	206.78	176.98	0.42	5.90	9	4
49			0.115	0.602	12.431	9.087	206.78	173.00	0.42	5.97	9	3
50	14:17:24.59	+52:30:24.9	0.064	0.044	1.359	1.305	206.78	176.98	0.48	5.71	65	40
51			0.064	0.018	1.359	1.287	206.78	173.00	0.48	5.77	65	29
52	14:17:29.27	+53:18:26.5	0.014	0.050	1.147	1.426	195.06	176.98	0.67	5.71	118	33
53			0.015	0.022	1.077	1.197	206.75	173.00	0.63	5.77	294	29
54	14:17:51.14	+52:23:11.1	0.029	0.043	1.399	1.188	195.09	173.00	0.44	5.77	33	36
55	14:18:56.19	+53:58:45.0	0.014	0.058	1.644	1.435	206.78	176.98	0.69	5.71	112	35
56	14:19:23.37	+54:22:01.7	0.062	0.109	1.308	1.479	206.78	176.98	0.69	5.71	87	26
57			0.062	0.061	1.308	1.305	206.78	173.00	0.69	5.77	87	24
58	14:19:41.11	+53:36:49.6	0.056	0.041	3.212	1.443	195.11	176.98	0.56	5.71	32	20
59	14:19:52.23	+53:13:40.9	0.088	0.035	1.859	1.516	206.78	176.98	0.67	5.71	24	12
60	14:19:55.62	+53:40:07.2	0.047	0.131	1.253	2.014	206.78	153.02	0.84	5.67	50	11
61	14:19:55.62	+53:40:07.2	0.047	0.038	1.253	1.617	206.78	148.05	0.84	5.92	50	14
62	14:20:10.25	+52:40:29.6	0.109	0.201	2.217	2.753	195.10	176.98	0.55	5.71	25	26
63			0.106	0.107	1.758	1.738	206.78	143.98	0.53	5.76	40	14
64	14:20:23.88	+53:16:05.1	0.116	0.088	1.850	1.914	206.78	176.98	0.68	5.71	23	10
65	14:20:38.52	+53:24:16.5	0.057	0.085	1.302	1.426	176.98	176.98	5.71	5.71	516	49
66			0.022	0.029	1.368	1.218	206.79	173.00	0.46	5.77	84	26
67	14:20:39.80	+52:03:59.7	0.070	0.105	1.245	1.601	176.98	176.98	5.90	5.90	415	57
68			0.075	0.045	1.440	1.272	206.77	173.00	0.80	5.77	55	45
69	14:20:43.53	+52:36:11.4	0.013	0.049	1.161	1.268	195.10	173.00	0.41	5.77	68	32
70	14:20:49.28	+52:10:53.3	0.074	0.116	1.326	1.532	176.98	176.98	6.10	6.10	249	44
71			0.113	0.148	1.684	2.295	195.09	176.98	0.70	5.71	24	14
72	14:20:52.44	+52:56:22.4	0.018	0.029	1.128	1.142	206.78	176.98	0.68	5.71	71	72
73	14:21:03.53	+51:58:19.5	0.010	0.069	1.160	1.699	206.77	176.98	0.80	5.71	149	34
74			0.010	0.024	1.160	1.187	206.77	173.00	0.80	5.77	149	44
75	14:21:12.29	+52:41:47.3	0.037	0.110	1.375	2.033	195.10	176.98	0.54	5.90	33	8
76	14:21:35.90	+52:31:38.9	0.021	0.293	1.184	3.738	206.77	176.98	0.66	5.71	89	12
77			0.021	0.123	1.184	1.604	206.77	173.00	0.66	5.77	89	33
78	14:24:17.22	+53:02:08.9	0.148	0.710	2.665	1.017	206.78	176.98	1.04	5.90	15	5
79	15:36:38.40	+54:33:33.2	0.045	0.047	1.184	1.249	109.65	109.65	2.49	2.49	185	284
80	15:59:09.62	+35:01:47.6	0.053	0.035	1.284	1.147	55.86	55.86	2.15	2.15	124	128
81	17:19:14.49	+48:58:49.4	0.309	0.099	3.964	1.731	8138.42	8392.42	71.39	71.73	11	33
82	23:03:15.67	+08:52:25.3	0.035	0.062	1.204	1.381	137.80	108.86	0.50	1.51	140	51

Note: Col. (1): Number. Col. (2): RA. Col. (3): Dec. Col. (4): Excess variance for continuum. Col. (5): Excess variance for line. Col. (6): Maximum to minimum flux ratio for continuum. Col. (7): Maximum to minimum flux ratio for line. Col. (8): Total duration of observation for continuum. Col. (9): Total duration of observation for line. Col. (10): Mean cadence of observation for continuum. Col. (11): Mean cadence of observation for line. Col. (12): Median signal to noise ratio for continuum. Col. (13): Median signal to noise ratio for line.

Table 5.2: Results of BLR modeling for the Hβ line light curves. Detrending was performed for the objects with *, while for the others detrending was not done. The BLR model fits are shown for the objects with • in Fig. 5.3 and Fig. 5.16.

α_{2000}	δ_{2000}	continuum	$\log(\tau_d)$(days)	$\tau_{\rm model}$ (days)	$\theta_{\rm inc}$(degree)	$\theta_{\rm opn}(degree)$	γ	$f_{\rm BLR}$	χ^2/dof
00:10:31.01	+10:58:29.5	—	2.78 ± 2.88	11.18 ± 5.7	46.10 ± 25.43	46.87 ± 25.88	-0.55 ± 0.10	—	1.13
02:30:05.52	-08:59:53.2	—	0.61 ± 0.58	50.61 ± 25.30	67.61 ± 21.52	36.24 ± 26.93	0.07 ± 0.08	0.83 ± 0.36	1.20
02:30:05.52	-08:59:53.2*	—	—	54.28 ± 19.54	75.22 ± 17.54	28.96 ± 23.49	—	—	1.20
06:52:12.32	+74:25:37.2	—	—	43.0 ± 18.49	44.72 ± 24.61	44.17 ± 26.18	—	—	1.47
06:52:12.32	+74:25:37.2*	—	2.81 ± 2.32	11.96 ± 4.54	32.96 ± 23.22	38.73 ± 24.87	-0.31 ± 0.09	1.45 ± 1.19	1.62
11:39:13.92	+33:55:51.1	—	0.72 ± 0.80	10.37 ± 5.7	52.09 ± 24.59	47.74 ± 25.90	0.12 ± 0.15	—	0.90
11:39:13.92	+33:55:51.1	—	0.09 ± 0.20	5.63 ± 3.66	56.40 ± 24.31	47.40 ± 26.27	0.41 ± 0.19	—	0.85
11:39:13.92	+33:55:51.1*	—	—	5.35 ± 3.96	54.51 ± 24.86	47.32 ± 26.31	—	—	0.90
12:42:10.61	+33:17:02.7	—	—	52.3 ± 16.74	73.75 ± 12.91	35.61 ± 22.71	—	—	0.89
12:42:10.61	+33:17:02.7*	—	1.32 ± 1.32	51.26 ± 17.43	77.33 ± 12.85	25.20 ± 22.81	-0.02 ± 0.12	0.88 ± 0.25	1.60
13:42:08.39	+35:39:15.3	—	0.10 ± 0.10	2.20 ± 1.76	51.1 ± 24.92	48.5 ± 25.82	1.67 ± 0.28	—	1.08
14:05:18.02	+53:15:30.0	g	1.05 ± 1.26	23.73 ± 19.46	47.88 ± 24.79	48.19 ± 25.6	1.70 ± 0.82	—	1.06
14:05:18.02	+53:15:30.0	i	—	24.70 ± 28.90	45.76 ± 25.24	47.05 ± 25.98	—	—	1.08
14:07:59.07	+53:47:59.8•	—	0.99 ± 1.08	18.74 ± 7.50	65.02 ± 22.13	36.95 ± 26.54	1.76 ± 0.29	0.85 ± 0.38	1.24
14:08:12.09	+53:53:03.3	g	—	11.83 ± 6.50	39.30 ± 25.34	43.51 ± 26.13	—	—	1.51
14:08:12.09	+53:53:03.3	i	2.93 ± 2.82	11.25 ± 6.86	40.91 ± 25.47	44.23 ± 25.76	2.77 ± 0.18	—	1.17
14:09:04.43	+54:03:44.2	g	2.68 ± 2.82	15.56 ± 8.40	44.16 ± 25.21	46.39 ± 25.96	0.20 ± 0.14	—	1.01
14:09:04.43	+54:03:44.2	i	—	19.77 ± 9.29	49.62 ± 24.77	48.59 ± 25.84	—	—	0.86
14:10:04.27	+52:31:41.0	g	0.91 ± 1.36	44.11 ± 11.03	51.84 ± 24.39	50.25 ± 25.49	2.36 ± 0.47	—	1.13
14:10:18.04	+53:29:37.5	g	1.33 ± 1.62	15.56 ± 7.00	48.48 ± 24.93	47.89 ± 25.78	2.43 ± 0.41	—	0.89
14:10:31.33	+52:15:33.8*	g	1.09 ± 1.46	30.72 ± 13.52	29.99 ± 22.58	34.88 ± 25.56	2.46 ± 0.53	1.73 ± 1.62	2.98
14:10:41.25	+53:18:49.0	i	2.65 ± 2.58	27.75 ± 11.66	32.66 ± 22.51	41.74 ± 24.78	0.96 ± 0.19	—	1.02
14:11:12.72	+53:45:07.1•	—	0.62 ± 0.84	21.72 ± 7.60	26.37 ± 22.59	32.47 ± 23.17	0.90 ± 0.29	2.06 ± 2.05	0.97
14:11:15.19	+51:52:09.0	i	1.78 ± 2.20	42.00 ± 13.86	62.27 ± 22.28	45.13 ± 26.42	0.83 ± 0.26	—	0.98
14:11:23.42	+52:13:31.7	i	2.69 ± 2.64	15.70 ± 7.53	38.03 ± 24.10	45.02 ± 24.90	1.20 ± 0.15	—	0.75
14:11:35.89	+51:50:04.5	g	—	17.45 ± 19.72	45.30 ± 25.66	45.74 ± 25.90	—	—	1.15
14:11:35.89	+51:50:04.5	i	1.60 ± 2.26	17.10 ± 15.39	45.66 ± 25.68	45.53 ± 26.04	1.31 ± 0.73	—	1.06
14:12:53.92	+54:00:14.4	—	0.62 ± 0.66	24.74 ± 10.14	42.23 ± 26.23	44.35 ± 26.0	2.18 ± 0.39	—	1.01
14:13:14.97	+53:01:39.4	g	—	33.58 ± 17.13	49.58 ± 28.67	35.84 ± 27.01	—	—	1.65
14:13:14.97	+53:01:39.4	i	1.31 ± 1.90	33.25 ± 14.30	52.24 ± 26.20	42.56 ± 26.84	1.83 ± 0.71	—	1.42
14:13:18.96	+54:32:02.4	g	1.72 ± 2.06	20.93 ± 7.32	30.25 ± 26.58	31.74 ± 25.12	1.14 ± 0.48	1.88 ± 2.00	1.32
14:13:18.96	+54:32:02.4	i	—	19.13 ± 7.08	47.07 ± 24.97	44.13 ± 25.80	—	—	1.53
14:13:24.28	+53:05:27.0	g	—	29.79 ± 12.51	53.74 ± 25.36	45.69 ± 26.19	—	—	1.02
14:13:24.28	+53:05:27.0	i	1.18 ± 1.62	21.85 ± 9.83	53.83 ± 24.75	47.42 ± 26.18	0.48 ± 0.24	—	0.86
14:14:17.13	+51:57:22.6	i	2.01 ± 1.84	11.68 ± 12.14	41.83 ± 25.69	43.98 ± 26.08	1.97 ± 0.66	—	2.00
14:14:17.13	+51:57:22.6*	i	—	11.11 ± 12.66	43.80 ± 25.71	44.96 ± 26.01	—		1.97
14:15:32.36	+52:49:05.9	i	-0.01 ± 0.14	7.32 ± 8.64	44.56 ± 25.95	44.63 ± 26.17	0.07 ± 0.27	—	1.18
14:16:25.71	+53:54:38.5	—	—	37.21 ± 12.28	41.60 ± 22.29	52.74 ± 24.13	—	—	1.02
14:16:25.71	+53:54:38.5*	—	1.80 ± 2.12	26.49 ± 9.8	68.47 ± 18.79	39.71 ± 25.38	0.03 ± 0.11	0.79 ± 0.30	1.61
14:16:45.15	+54:25:40.8	—	—	22.02 ± 11.89	58.06 ± 22.50	46.67 ± 26.53	—	—	1.75
14:16:45.15	+54:25:40.8*	—	0.77 ± 0.90	19.14 ± 10.34	53.12 ± 23.09	49.88 ± 25.75	2.71 ± 0.21	—	1.65
14:16:45.58	+53:44:46.8	—	0.62 ± 0.74	17.53 ± 10.87	41.63 ± 23.84	48.32 ± 24.78	2.26 ± 0.38	—	1.10

α_{2000}	δ_{2000}	continuum	$\log(\tau_d)$ (days)	$\tau_{\rm model}$ (days)	$\theta_{\rm inc}$ (degree)	$\theta_{\rm opn}$ (degree)	γ	$f_{\rm BLR}$	χ^2/dof
14:17:06.68	+51:43:40.1	—	—	25.11 ± 9.29	50.71 ± 22.7	54.20 ± 25.50	—	—	2.36
14:17:06.68	+51:43:40.1*•	—	1.20 ± 1.32	22.95 ± 8.95	57.91 ± 21.62	51.79 ± 25.78	1.44 ± 0.41	—	1.50
14:17:12.30	+51:56:45.5	g	2.67 ± 2.56	17.10 ± 8.55	42.17 ± 26.37	44.16 ± 25.0	1.89 ± 0.40	—	1.24
14:17:24.59	+52:30:24.9	g	2.69 ± 2.42	19.04 ± 10.28	39.66 ± 23.99	43.85 ± 26.19	0.37 ± 0.46	—	1.39
14:17:29.27	+53:18:26.5	g	—	13.29 ± 13.96	48.16 ± 25.21	46.32 ± 26.17	—	—	1.43
14:17:29.27	+53:18:26.5	i	1.09 ± 1.30	13.03 ± 15.38	45.75 ± 26.07	45.24 ± 26.06	1.90 ± 0.53	—	1.34
14:18:56.19	+53:58:45.0	g	—	34.78 ± 13.56	39.74 ± 23.28	44.89 ± 25.30	—	—	2.29
14:18:56.19	+53:58:45.0*	g	0.60 ± 0.74	17.62 ± 9.89	40.6 ± 24.97	43.99 ± 25.66	2.33 ± 0.53	—	2.32
14:19:23.37	+54:22:01.7	g	2.88 ± 2.58	15.62 ± 10.93	48.03 ± 25.69	46.87 ± 25.82	0.93 ± 0.20	—	1.35
14:19:41.11	+53:36:49.6	g	—	26.35 ± 20.56	45.01 ± 25.78	45.11 ± 26.06	—	—	1.51
14:19:41.11	+53:36:49.6	i	2.36 ± 2.50	33.84 ± 21.66	40.19 ± 25.57	43.81 ± 25.54	0.30 ± 0.54	—	1.33
14:19:52.23	+53:13:40.9	g	2.63 ± 2.58	21.47 ± 30.70	36.61 ± 25.47	42.35 ± 25.07	0.12 ± 0.81	—	1.73
14:19:55.62	+53:40:07.2	g	2.59 ± 2.54	8.34 ± 10.76	42.57 ± 26.21	43.91 ± 26.02	2.70 ± 0.24	—	1.43
14:20:10.25	+52:40:29.6*	i	1.39 ± 1.66	5.28 ± 5.96	61.91 ± 23.02	39.83 ± 25.76	2.95 ± 0.04	0.84 ± 0.39	7.09
14:20:23.88	+53:16:05.1	g	2.62 ± 2.42	11.47 ± 15.60	53.48 ± 26.47	45.38 ± 25.72	0.59 ± 0.63	—	1.47
14:20:23.88	+53:16:05.1	i	—	14.01 ± 14.43	52.70 ± 25.91	44.96 ± 26.07	—	—	1.37
14:20:38.52	+53:24:16.5	—	1.00 ± 1.14	25.92 ± 9.33	50.10 ± 23.85	51.24 ± 25.20	0.70 ± 0.22	—	1.05
14:20:39.80	+52:03:59.7	—	—	29.14 ± 11.07	22.77 ± 22.81	27.69 ± 23.85	—	—	1.56
14:20:39.80	+52:03:59.7*	—	0.81 ± 1.00	27.17 ± 9.51	27.89 ± 24.09	33.61 ± 24.82	1.10 ± 0.36	1.90 ± 1.92	1.02
14:20:49.28	+52:10:53.3	g	—	47.93 ± 7.19	14.34 ± 14.98	19.19 ± 17.13	—	—	2.01
14:20:49.28	+52:10:53.3	i	2.30 ± 2.60	46.52 ± 7.44	17.42 ± 17.38	25.05 ± 19.50	-0.34 ± 0.12	3.72 ± 4.33	1.85
14:20:49.28	+52:10:53.3*	i	—	42.94 ± 8.59	26.97 ± 21.62	34.91 ± 23.34	—	—	1.21
14:20:52.44	+52:56:22.4	g	0.67 ± 0.94	16.84 ± 7.07	49.01 ± 24.60	48.93 ± 25.68	0.82 ± 0.24	—	0.71
14:21:03.53	+51:58:19.5	g	1.88 ± 2.20	20.63 ± 12.99	37.81 ± 26.62	38.66 ± 25.71	2.61 ± 0.32	1.31 ± 1.07	2.83
14:21:12.29	+52:41:47.3	g	—	18.33 ± 9.35	41.37 ± 25.47	44.44 ± 26.07	—	—	1.13
14:21:12.29	+52:41:47.3	i	1.88 ± 2.34	15.16 ± 9.25	42.83 ± 25.63	45.21 ± 26.13	2.09 ± 0.59	—	1.15
14:21:35.90	+52:31:38.9	g	—	7.6 ± 4.79	15.08 ± 16.91	20.51 ± 18.85	—	—	8.06
14:21:35.90	+52:31:38.9*•	g	2.88 ± 2.42	6.54 ± 3.14	15.67 ± 18.49	21.10 ± 20.72	2.96 ± 0.04	4.94 ± 7.20	8.14
14:24:17.22	+53:02:08.9	g	2.70 ± 2.80	19.36 ± 22.46	47.18 ± 26.15	46.45 ± 26.20	2.01 ± 0.45	—	2.38
15:36:38.40	+54:33:33.2	—	1.16 ± 1.22	26.89 ± 5.92	63.46 ± 21.38	47.87 ± 26.73	0.33 ± 0.15	—	1.29
15:59:09.62	+35:01:47.6	—	1.12 ± 1.16	13.32 ± 3.46	57.50 ± 22.92	49.20 ± 25.99	0.12 ± 0.16	—	1.42
17:19:14.49	+48:58:49.4	—	1.53 ± 1.54	65.12 ± 16.93	64.18 ± 20.44	45.31 ± 26.54	-0.63 ± 0.03	—	1.12
17:19:14.49	+48:58:49.4*	—	—	65.78 ± 17.10	58.85 ± 22.23	49.24 ± 26.21	—	—	1.21
23:03:15.67	+08:52:25.3	—	—	52.67 ± 16.86	54.83 ± 10.46	10.76 ± 14.0	—	—	1.07
23:03:15.67	+08:52:25.3*	—	1.17 ± 1.22	7.06 ± 1.41	42.84 ± 25.72	44.15 ± 25.45	0.07 ± 0.08	—	2.16

Table 5.3: Results of Hα and Mg II lines. Detrending was performed for the objects with *, while for the others detrending was not done. The BLR model fits are shown for the objects with • in Fig. 5.3 and Fig. 5.16.

α_{2000}	δ_{2000}	continuum	$\log(\tau_d)$ (days)	$\tau_{\rm model}$ (days)	$\theta_{\rm inc}$ (degree)	$\theta_{\rm opn}$ (degree)	γ	χ^2/dof
13:42:08.39	+35:39:15.3*	—	0.02 ± 0.02	2.29 ± 2.24	42.20 ± 26.05	42.36 ± 25.29	1.13 ± 0.28	1.56
14:05:18.02	+53:15:30.0	g	1.09 ± 1.09	20.43 ± 30.03	43.42 ± 25.63	45.66 ± 25.51	0.58 ± 1.06	1.63
14:05:51.99	+53:38:52.1	g	1.46 ± 1.60	41.06 ± 27.92	40.04 ± 25.22	45.38 ± 25.43	0.82 ± 0.75	1.36
14:08:12.09	+53:53:03.3	g	2.21 ± 2.21	11.48 ± 6.54	40.70 ± 25.48	44.39 ± 26.00	1.98 ± 0.37	1.08
14:09:15.70	+53:27:21.8	g	1.44 ± 1.52	46.08 ± 12.90	32.25 ± 22.35	38.86 ± 24.43	2.24 ± 0.46	0.92
14:10:04.27	+52:31:41.0	g	1.04 ± 1.14	7.15 ± 13.72	47.96 ± 25.67	45.76 ± 26.02	0.68 ± 1.04	1.60
14:10:18.04	+53:29:37.5	g	1.37 ± 1.51	23.92 ± 10.05	39.83 ± 24.69	45.95 ± 25.30	1.01 ± 0.72	1.03
14:10:41.25	+53:18:49.0	g	—	26.13 ± 10.19	32.70 ± 22.69	39.85 ± 24.91	—	1.14
14:10:41.25	+53:18:49.0	i	2.53 ± 2.41	21.61 ± 8.21	37.80 ± 24.96	43.35 ± 25.42	-0.12 ± 0.08	0.94
14:11:15.19	+51:52:09.0	g	0.98 ± 1.10	1.07 ± 2.05	45.87 ± 25.93	45.06 ± 25.99	0.64 ± 0.93	1.39
14:11:23.42	+52:13:31.7	g	2.73 ± 2.35	39.38 ± 12.60	46.32 ± 24.38	48.79 ± 25.25	0.16 ± 0.10	0.94
14:13:24.28	+53:05:27.0	g	2.74 ± 2.26	47.20 ± 10.86	35.84 ± 22.00	43.54 ± 24.66	-0.64 ± 0.32	0.58
14:16:25.71	+53:54:38.5	g	2.04 ± 2.24	38.73 ± 18.20	38.66 ± 23.54	45.94 ± 25.59	-0.52 ± 0.19	0.95
14:16:45.15	+54:25:40.8	g	2.85 ± 2.51	17.49 ± 8.40	51.18 ± 24.10	49.99 ± 25.71	2.42 ± 0.32	1.16
14:16:45.58	+53:44:46.8	g	1.90 ± 2.14	18.62 ± 12.47	44.58 ± 25.35	45.83 ± 26.07	1.36 ± 0.84	1.32
14:17:12.30	+51:56:45.5•	g	2.71 ± 2.35	3.25 ± 7.12	$43.8^{\pm}26.21$	44.56 ± 26.02	-0.63 ± 0.48	1.51
14:17:24.59	+52:30:24.9	g	2.05 ± 2.21	6.94 ± 12.55	43.75 ± 25.72	44.91 ± 25.77	-0.69 ± 0.27	1.34
14:17:29.27	+53:18:26.5	g	1.17 ± 1.27	3.81 ± 7.92	45.95 ± 25.83	45.58 ± 25.93	0.23 ± 0.77	1.67
14:17:51.14	+52:23:11.1	g	—	17.16 ± 9.44	48.20 ± 25.32	46.14 ± 26.07	—	0.94
14:17:51.14	+52:23:11.1	i	1.87 ± 2.17	13.91 ± 6.68	47.23 ± 25.29	45.59 ± 25.99	0.75 ± 0.26	0.86
14:19:23.37	+54:22:01.7	g	2.88 ± 2.50	62.08 ± 14.74	40.01 ± 26.54	42.12 ± 26.31	0.53 ± 0.24	1.21
14:19:55.62	+53:40:07.2	g	2.48 ± 2.39	3.64 ± 7.67	46.31 ± 25.89	45.82 ± 25.41	0.61 ± 0.66	1.17
14:20:10.25	+52:40:29.6	g	2.63 ± 2.37	46.67 ± 9.8	39.52 ± 24.53	44.69 ± 25.25	0.70 ± 0.39	1.73
14:20:38.52	+53:24:16.5	g	1.68 ± 2.14	24.17 ± 13.53	49.87 ± 25.44	46.47 ± 25.83	0.39 ± 0.34	0.94
14:20:39.80	+52:03:59.7	g	2.81 ± 2.57	35.95 ± 14.38	37.17 ± 24.81	42.06 ± 25.36	-0.26 ± 0.09	1.26
14:20:43.53	+52:36:11.4	i	1.61 ± 1.73	3.78 ± 4.65	44.33 ± 26.20	43.91 ± 26.30	2.54 ± 0.35	1.52
14:21:03.53	+51:58:19.5	g	1.76 ± 2.12	5.57 ± 6.29	45.6 ± 25.76	44.97 ± 25.91	0.97 ± 0.58	1.23
14:21:35.90	+52:31:38.9	g	—	14.84 ± 8.46	29.49 ± 20.67	37.35 ± 24.13	—	2.30
14:21:35.90	+52:31:38.9*	g	2.80 ± 2.24	13.98 ± 7.27	30.83 ± 21.3	39.16 ± 24.54	2.94 ± 0.06	2.14
14:10:18.04	+53:29:37.5	—	0.61 ± 0.61	32.62 ± 11.74	44.73 ± 27.21	43.98 ± 26.54	2.65 ± 0.26	1.30
14:12:14.20	+53:25:46.7*•	—	0.86 ± 0.86	38.59 ± 6.95	4.00 ± 2.79	6.02 ± 3.97	2.96 ± 0.03	4.91
14:14:17.13	+51:57:22.6	—	0.37 ± 0.49	28.15 ± 10.42	46.02 ± 25.77	46.68 ± 25.84	0.52 ± 0.24	0.92
14:16:44.17	+53:25:56.1	—	-0.13 ± 0.10	19.80 ± 9.90	32.44 ± 25.46	36.60 ± 25.58	1.38 ± 0.36	1.13
14:16:50.93	+53:51:57.0	—	0.08 ± 0.04	17.41 ± 15.67	45.00 ± 27.06	44.00 ± 26.23	2.07 ± 0.39	1.07
14:20:49.28	+52:10:53.3	—	1.18 ± 1.20	34.12 ± 10.24	62.23 ± 22.69	47.69 ± 27.15	1.10 ± 0.26	1.23

in Chapter 3. The light curves analyzed here for some objects were corrected for the constant host galaxy contribution to the observed continuum and the narrow-line contamination to the observed line fluxes. For a few sources, the host galaxy and the narrow line contamination to the observed continuum and line fluxes were not removed. That might have some effect on the obtained F_{var} values, however, might not lead to biases considering a comparative analysis of the F_{var} values between the continuum and different emission lines. The results of variability analysis is given in Table 5.1. The distributions of F_{var} for both the continuum and line which includes Mg II, Hβ and Hα, are given in Fig. 5.2. Using a two sample Kolmogorov-Smirnov (KS) test, we found that the two distributions are indeed different with a statistic of 0.317 and a p value of 4.0×10^{-4}. The mean F_{var} values were found to be 0.058 ± 0.001 and 0.107 ± 0.012 for continuum and line, respectively. A total of 50 measurements for Hβ, 26 for Hα and 6 for Mg II line were used in this study. Separating the sample into different lines used, for Hβ we found mean F_{var} values of 0.066 ± 0.002 and 0.120 ± 0.012 for continuum and line, respectively. For Hα the mean F_{var} values are 0.041 ± 0.001 and 0.076 ± 0.018 for continuum and line, respectively, while for Mg II we found mean F_{var} of 0.057 ± 0.000 and 0.120 ± 0.002 for continuum and line, respectively. Hence, the F_{var} value in emission line is found to exceed that of the continuum. Such increased variations of emission lines relative to the continuum indicate the deviation of BLR from the linear response to the ionizing continuum (Rashed et al., 2015; Li et al., 2013). Though, photoionization calculations predict that Mg II line should be less responsive to the ionizing continuum than Balmer lines (Korista & Goad, 2000, 2004), Woo (2008) found F_{var} in Mg II line higher than that of the continuum, similar to what is found in this work. For intermediate-redshift quasars the Mg II line may be produced almost

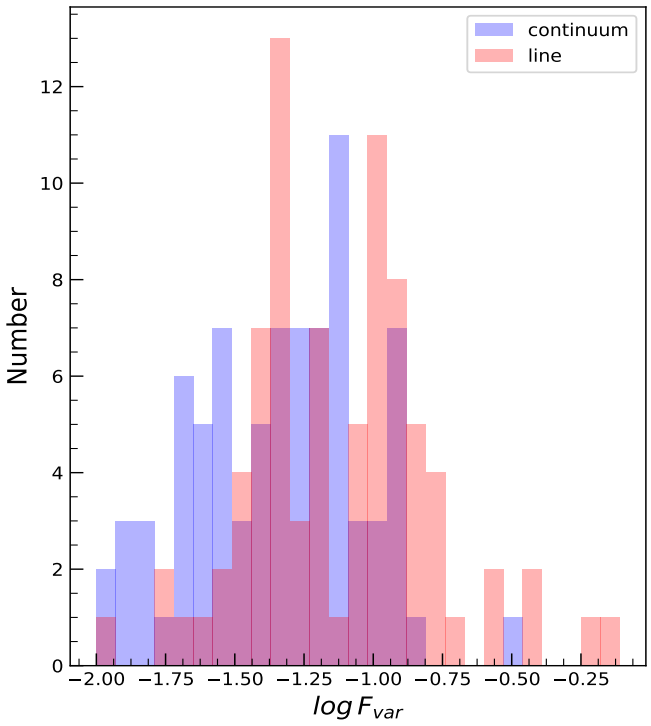

Figure 5.2: Distribution of excess variance, F_{var}, of the objects studied here.

in the same region as Hβ, as can be seen in the cases of NGC 3783 and NGC 4151, in which similar time lags were obtained using Hβ and Mg II lines (Reichert et al., 1994; Peterson et al., 2004; Metzroth et al., 2006; Woo, 2008). Therefore, there is a possibility of detecting a similar kind of emission line variability in both the Hβ and Mg II lines in these objects.

5.2.2 BLR characteristics

Pancoast et al. (2011) developed a Bayesian approach to model the BLR and subsequently, this approach was applied to Arp 151 (Brewer et al., 2011) and Mrk 50 (Pancoast et al., 2012). Apart from Mrk 50 and Arp 151, more AGN were subjected to BLR modeling (Pancoast et al., 2014; Grier et al., 2017a; Williams et al., 2018; Li et al., 2013). The BLR modeling based on Li et al. (2013), which is used in this work, is an independent im-

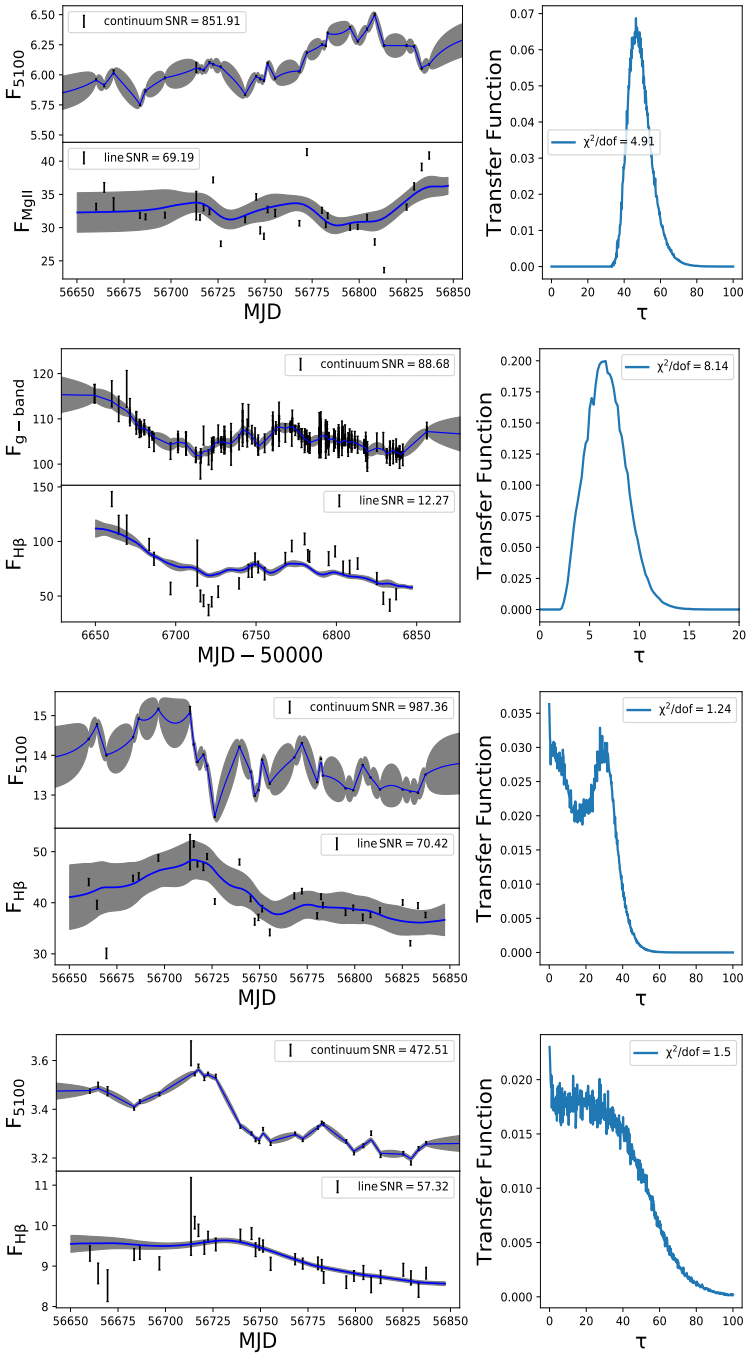

Figure 5.3: Examples of BLR model fits returned by PBMAP code to four objects J1412+534, J1421++525, J1407+537 and J1417+517 from top to bottom, respectively. The data points with error bars represent the observed light curves, whereas, the thick solid lines are the reconstructed light curves in the left hand panels. The grey shaded areas show the uncertainties in the modeled light curves. The corresponding transfer function for each object is shown on the right hand panel.

plementation of the approach of Pancoast et al. (2011), with the additional inclusion of (a) non-linear response of emission lines to the ionizing continuum variations and (b) option to perform a detrending of the light curves whenever required. Here, the data for 57 objects were analysed with 82 independent measurements for Hβ, Hα and Mg II lines, which is about twice the number of AGN studied earlier (Li et al., 2013) for uncovering the BLR characteristics. The final fitting results are given in Table 5.2 for Hβ and in Table 5.3 for Hα and Mg II lines. We illustrate few examples of our BLR model fits to their observed continuum and line RM data in Fig. 5.3. In these plots, the data points with error bars represent the observed light curves, whereas the thick solid lines are the reproduced light curves by the model. For the object J1412+534, few points of the observed line light curve are found to deviate from the reconstructed light curve. The obtained $\chi^2/dof = 4.91$ is also quite large pointing to poor fit to the observed light curve. The most deviant observed points in the line light curve from the model fit are found to deviate from the general pattern of the observed line light curve resulting in larger χ^2/dof in the fitting. The non-linear parameter γ is also found to be 2.96 pointing to a non-linear response of the Mg II line light curve to the optical continuum at 5100 Å. There is a discrepancy between the observed and model fitted line light curve for the object J1421+525. The obtained χ^2/dof of 8.14 could be because of poor sampling and/or SNR of the emission line measurements. The corresponding transfer functions obtained from the model for those four objects are illustrated in the right hand panel of Fig. 5.3. We found different shapes of transfer functions for different objects. For example in J1412+534 (top panel; α_{2000} = 14:12:14.20, δ_{2000} = 53:25:46.7), the transfer function shows single peak at $\tau = \tau_{lag}$ with $\theta_{inc} = 4.0 \pm 2.8$ deg and $\theta_{opn} = 6.0 \pm 3.9$ deg. For the object J1407+537 (α_{2000} = 14:07:59.07, δ_{2000} = 53:47:59.8), the

transfer function is double peaked, for which we found θ_{inc} = 65.0 $\pm$ 22.1 deg and θ_{opn} = 37.0 $\pm$ 26.5 deg. For J1417+517 (bottom panel; α_{2000} = 14:17:06.68, δ_{2000} = 51:43:40.1), the transfer function is found to have a top hat structure with θ_{inc} and θ_{opn} of 57.9 $\pm$ 21.6 deg and 51.8 $\pm$ 25.8 deg, respectively. The peak of the transfer function may trace the size of the BLR for the objects with single peaked transfer function, but can not be used as a reliable indicator to measure the delay between the continuum and line time series. The first moment of transfer function, which represents the time lag in CCF analysis, gives better estimate of the average size of the BLR (Gaskell & Sparke, 1986; Gaskell & Peterson, 1987; Kovačević et al., 2014). We noticed a) for a thick disk, larger $\theta_{\rm inc}$ tends to give a double-peaked transfer function, as seen in the case of object J1407+537 (third panel of Fig. 5.3 from the top) having $\theta_{\rm inc}$ = 65.0 $\pm$ 22.1 deg. The object appears more edge on as $\theta_{\rm inc}$ increases, and the contribution of radiation both from the front and back surfaces makes a double peaked transfer function, where the stronger peak appears closer to the center, b) a larger opening angle $\theta_{\rm opn}$ has a tendency to broaden the transfer function toward top-hat as can be seen in case of J1417+517 (bottom panel of Fig. 5.3) with $\theta_{\rm opn}$ of 51.8 $\pm$ 25.8 degree. The BLR tends to a spherical geometry as $\theta_{\rm opn}$ increases and the virial motion of the clouds causes the transfer function to broaden towards a top-hat structure.

The distribution of χ^2/dof obtained for the best fit model returned by PBMAP code is shown in Fig. 5.4. For a few sources, the fits are indeed bad (with $\chi^2/dof > 4$), namely J141214.20+532546.7, J141941.11+533649.6 and J142135.90+523138.9. These sources are found to have poor quality (less number of sparsely sampled points) data and is likely the reason for large χ^2/dof. Though the overall distribution of χ^2/dof seems skewed toward values greater than 1.0, in majority of the sources, we found a low

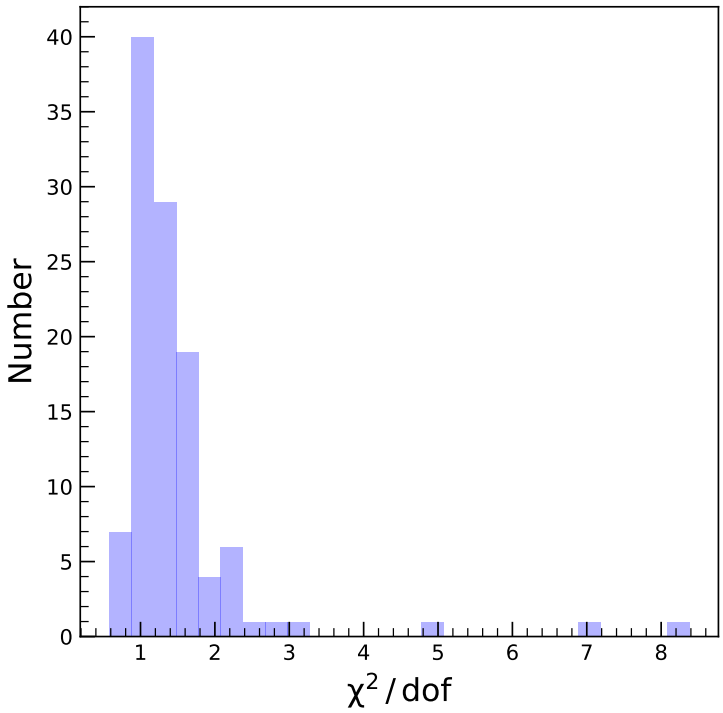

Figure 5.4: Distribution of χ^2/dof obtained from the model fitting for the objects analysed in this work.

χ^2/dof close to 1.0. We obtained $\chi^2/dof \leq 1.2$ for about 60% of the light curves. The poorer χ^2/dof in some objects is because of low SNR with continuum and line light curves having SNR < 50. Also, systematic errors because of calibration which are usually not included in the reported errors of the original light curve data could affect the χ^2 value. Overall, the continuum and emission line light curves reproduced by the model are found to be in good agreement with the observed data.

The distribution of the non-linearity parameter γ obtained from modeling is illustrated in Fig. 5.5. The mean values of γ are found to be $< \gamma_{MgII} >= 1.78 \pm 0.86$, $< \gamma_{H\beta} >= 1.18 \pm 1.03$ and $< \gamma_{H\alpha} >= 0.76 \pm 0.99$ for Mg II, Hβ and Hα, respectively. This clearly shows a non-linear response of emission-lines coming from the BLR to the ionizing optical continuum from the accretion disk. The anisotropic and non axis-symmetric emis-

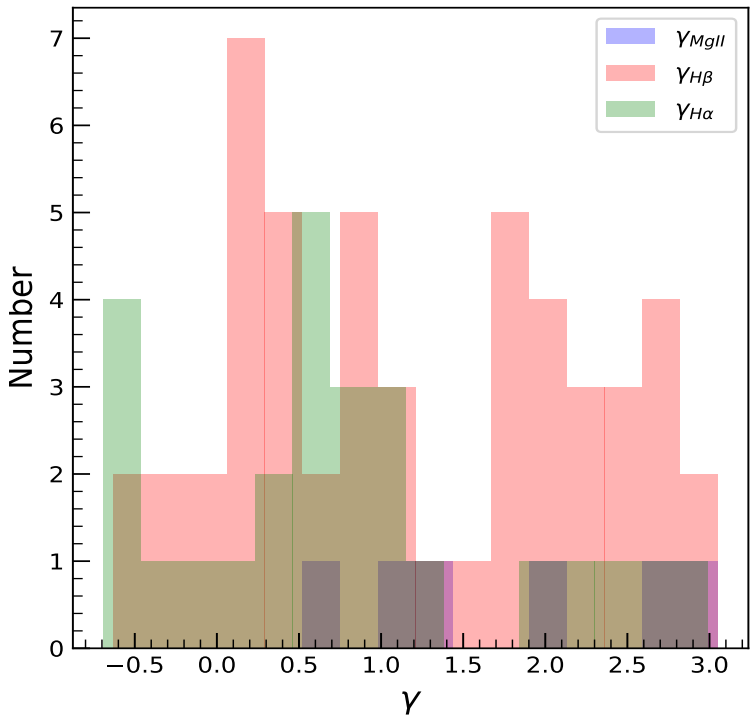

Figure 5.5: Distribution of γ, the non-linearity parameter for different emission lines.

sion originating from different spectral regions in AGN can cause such non-linear response of emission-line flux to the ionizing continuum (Korista & Goad, 2000, 2004; Gaskell et al., 2019). Also, it is noted that the shorter wavelength UV continuum usually vary larger compared to the longer wavelength optical continuum, hence, the response of a given emission line could be different depending on the continuum (O'Brien et al., 1995; Zhu et al., 2017).

5.2.3 Correlation of damping time scale with luminosity at 5100 Å for Hβ line fitting

Kelly et al. (2009) found the time scale of variability to correlate with luminosity by modeling the light curves of 100 quasars using DRW. Recently, Lu et al. (2019) applied DRW modeling of 73 AGN that includes high-

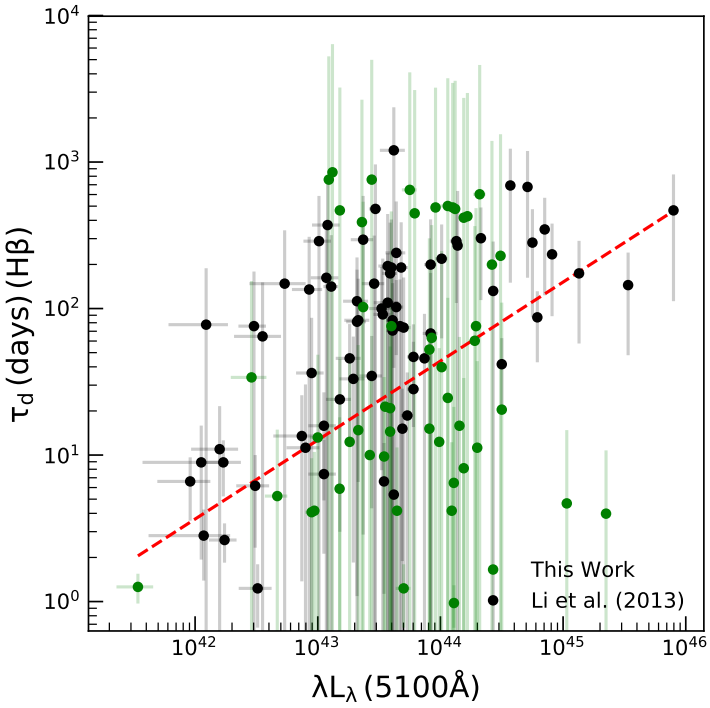

Figure 5.6: Dependence of the damping time scale (τ_d) on the monochromatic continuum luminosity at 5100 Å. Here, the filled green circles represent the objects studied in this work, whereas, filled black circles are the objects taken from Li et al. (2013). The best fit to the data points including measurements from this work and Li et al. (2013) is represented by the dashed red line.

accreting sources, which are also studied here. They found the damping time scale to correlate with the luminosity with a slope of 0.46 ± 0.09. However, MacLeod et al. (2010) using SDSS stripe 82 data, were unable to find any strong correlation with luminosity. In our study, we fitted emission line and continuum model parameters, simultaneously allowing us to study this relation.

The correlation between the derived damping time scale in rest frame and the observed host-galaxy corrected continuum luminosity at 5100 Å is shown in Fig. 5.6. The damping time scale τ_d is found to be positively

correlated with the luminosity at 5100 Å. By fitting linear least squares to the data, we found

$$\log\left(\frac{\tau_{d(H\beta)}}{1\text{day}}\right) = \beta + \alpha\log(\lambda L_{\lambda})(5100) \tag{5.4}$$

with $\alpha = 0.54 \pm 0.06$ and $\beta = -22.09 \pm 2.67$. The obtained slope of the correlation is similar to the value of $\alpha = 0.60 \pm 0.06$ found by Li et al. (2013), who did BLR modeling, in the same fashion as we performed here, from an analysis of 50 AGN with Hβ lags. It is noted that the scatter in the obtained relation is much higher than Lu et al. (2019), mainly because they fitted continuum light curves with only two main parameters, whereas we fitted both continuum and BLR model parameters, simultaneously. Moreover, their sample does not comprise objects from the SDSS RM sample, which has relatively less variability and time sampling. From a careful analysis it is found that the more deviant points have lower variability and therefore, the model parameters are not well constrained.

We calculated the Spearman rank correlation coefficient (r_s) using Monte Carlo simulation in which each point in the $\tau_d - \lambda L_{\lambda}$ plane is modified by a random Gaussian deviate which is consistent with the measured uncertainty to check the correlation between τ_d and luminosity at 5100 Å. The Monte Carlo simulation was performed for 10000 iterations and the median value of r_s from that distribution is found to be $0.218^{+0.065}_{-0.066}$ with a probability (p) of no correlation of $0.016^{+0.079}_{-0.015}$. The upper and lower uncertainties are obtained at the 15.9 and 84.1 percentile of the distributions of those 10000 iterations. According to Kozłowski (2017b,a), deriving damping time scale from light curves of short duration leads to biased result and the time length of the light curve must be 10 times the expected damping time scale. It is noted that RM light curves available are usually shorter in length in comparison with the long-term survey light curves, like those

from the Sloan Digital Sky Survey and the Catalina Real Time Transient Survey. In fact, for the light curves used to generate Fig. 5.6, the median ratios of the total span (Δt) of the light curves to the damping time scale τ_d are found to be 4.84 and 4.35 for continuum and line light curves, respectively. Considering only those objects having light curve length $> 10 \times \tau_d$, which corresponds to a total of 20 objects from our sample and 21 objects from Li et al. (2013), r_s is found to be $0.304^{+0.104}_{-0.104}$ with p-value of $0.053^{+0.155}_{-0.045}$ (10000 iterations) for the $\tau_d - \lambda L_\lambda$ relation. The least-square fit using Equation 5.4 gives $\alpha = 0.39 \pm 0.08$ and $\beta = -15.99 \pm 3.50$. Thus, the correlation obtained between τ_d and λL_λ is found to be significant at greater than 90% level. This result is consistent with Lu et al. (2019), who studied the characteristic of optical variability of RM data and found $\alpha = 0.46 \pm 0.09$ and $\beta = -18.52 \pm 4.06$ in the $\tau_d - \lambda L_\lambda$ relation, for the sources with light curve lengths greater than 10 times τ_d.

5.2.4 Comparison between R_{BLR}^{mod} and R_{BLR}^{CCF}

The comparison of the BLR size derived by the modeling approach (R_{BLR}^{mod}) with that obtained from the conventional CCF analysis (R_{BLR}^{CCF}) is illustrated in Fig. 5.7 (top panel). The derived BLR size from the model is in general consistent with that obtained from traditional CCF, however, with a large scatter. The median ratio of the size of BLR estimated by modeling to that obtained from CCF is found to be 1.09 with a standard deviation of 1.24. Li et al. (2013) found that the sizes of the BLR obtained from CCF analysis are underestimated by 20%. Though, from our analysis, we found a few objects to have R_{BLR} from model larger than that obtained from CCF analysis, a few others are found to have model R_{BLR} smaller than that of CCF. The distribution of the ratio between R_{BLR} model and R_{BLR} CCF is shown in the bottom panel of Fig. 5.7, where 3 objects are found to deviate from

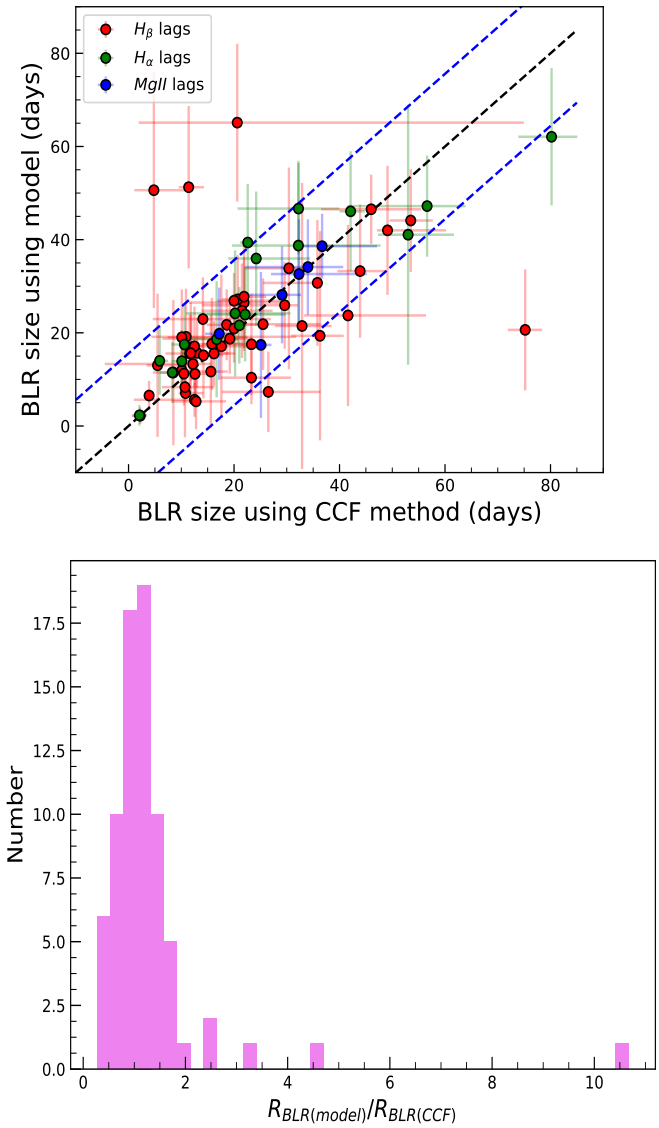

Figure 5.7: (Top) Comparison of the model BLR size obtained in this work and BLR size obtained from the traditional CCF analysis taken from literature. Red colored circles are the Hβ lags, whereas green and blue circles represent the Hα and Mg II lags, respectively. The black dashed line represents the y=x line, while the blue dashed lines show y = x $\pm$ σ, where $\sigma = 15.59$ days is the standard deviation of the BLR sizes obtained by CCF analysis. (Bottom) Distribution of the ratio of the BLR size derived from model ($R_{BLR(model)}$) to that obtained from CCF ($R_{BLR(CCF)}$).

the unit ratio by a factor larger than 3. It was found that the objects that show larger deviation from the $R_{\rm BLR}^{mod} = R_{\rm BLR}^{CCF}$ line also have large χ^2/dof (> 1.5) values giving ample indication of poor model fitting which could be due to the following reasons (a) light curves having low SNR, (b) inadequate sampling of the light curves and (c) presence of multiple peaks in the CCF leading to ambiguity in the determination of the peak of the CCF and hence, $R_{\rm BLR}$.

5.2.5 BLR size−luminosity correlation

RM observations over the years have led to a power law relation ($R_{\rm BLR} \propto L^{\alpha}$) between the BLR size and the optical luminosity of the AGN. The $R_{\rm BLR} - L$ relation can be used to determine $M_{\rm BH}$ using single epoch spectroscopic observations. Also, it can provide a means to consider AGN as standard candles (Loli Martínez-Aldama et al., 2019). Thus, it is important to check whether the obtained $R_{\rm BLR}$ from fitting shows the power law dependence with the optical luminosity that we know from observations. $R_{\rm BLR}$ from the model fitting has been found using Hβ, Hα and Mg II lines for sources spanning over a varied range of redshift. The correlation between $R_{\rm BLR}$ and luminosity for the line Hβ is shown in Fig. 5.8. Note that the luminosities are taken from the original literature and they are corrected for host-galaxy contamination.

The weighted linear least squares fit to the data points gives the following relation

$$\log\left(\frac{R_{\rm BLR(H\beta)}}{1\rm day}\right) = \beta + \alpha \log(\lambda L_{\lambda})(5100) \tag{5.5}$$

with $\alpha = 0.58 \pm 0.03$ and $\beta = -24.08 \pm 1.13$. Our obtained results are found to be similar to the value of $\alpha = 0.519^{+0.063}_{-0.066}$ and $\beta = -21.3^{+2.9}_{-2.8}$ obtained by Bentz et al. (2009) with $R_{\rm BLR}$ derived from the CCF analysis of

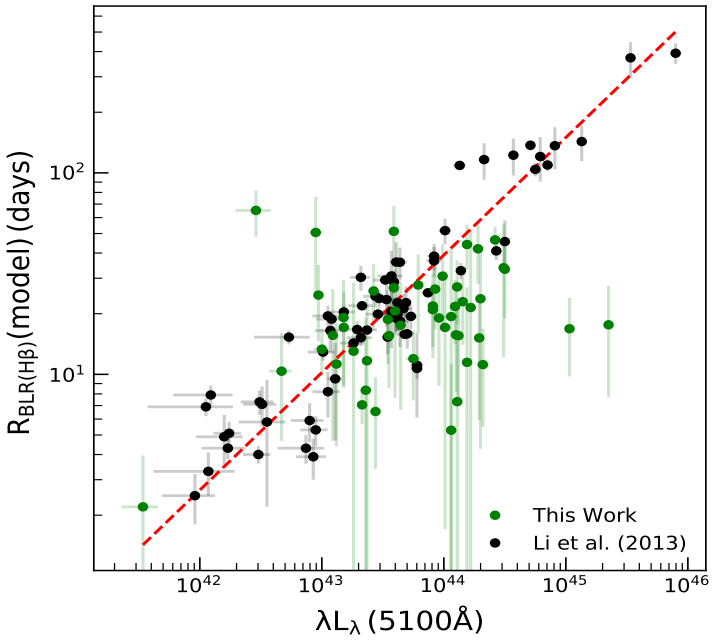

Figure 5.8: Relationship between the BLR radius obtained from the model for sources with Hβ line light curves and their continuum luminosity at 5100 Å. In the figure, the filled green circles represent the objects studied in this work, whereas the filled black circles are the measurements for the objects taken from Li et al. (2013). The dashed red line represents the best fit to the data points including measurements both from this work and Li et al. (2013).

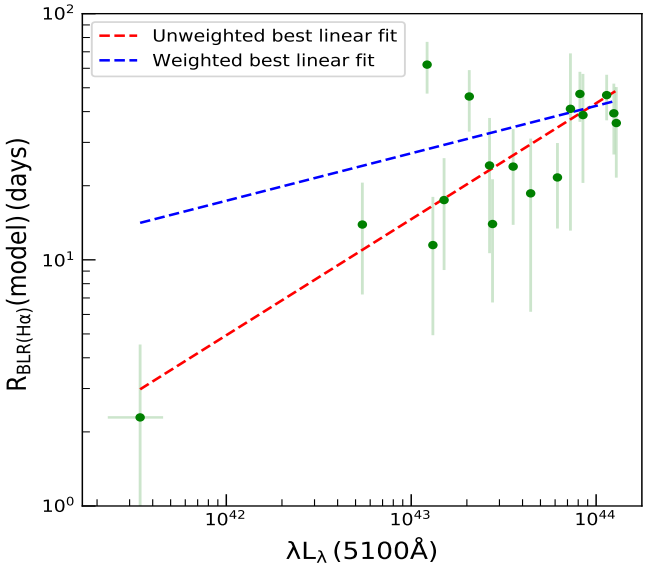

Figure 5.9: Relation between R_{BLR} and luminosity at 5100 Å for sources with Hα line light curves. The dashed blue and red lines represent the weighted and unweighted linear least squares fit, respectively, to the data points.

the observed continuum and line light curves. Bentz et al. (2013) obtained a slope of $\alpha = 0.533^{+0.035}_{-0.033}$ and $\beta = 1.527^{+0.031}_{-0.031}$ based on the lag-luminosity relation in the form of $\log\left(\frac{R_{BLR(H\beta)}}{1\,day}\right) = \beta + \alpha \log(\lambda L_\lambda / 10^{44}\, erg\, s^{-1})(5100)$. Our derived values closely match with those obtained by Bentz et al. (2013) within the uncertainties. Li et al. (2013) using the same approach adopted in this work for 40 quasars with Hβ lag measurements, found a value of α = 0.55 $\pm$ 0.03, which again is in agreement with our measurements using a different sample of 50 AGN for the Hβ line.

Similarly, for objects with Hα measurements, the relation between R_{BLR} and L_{5100} is illustrated in Fig. 5.9. Only those measurements with fractional error (ratio of the obtained uncertainty to its measured value) less than 1, were used in this correlation. The weighted linear least squares fit

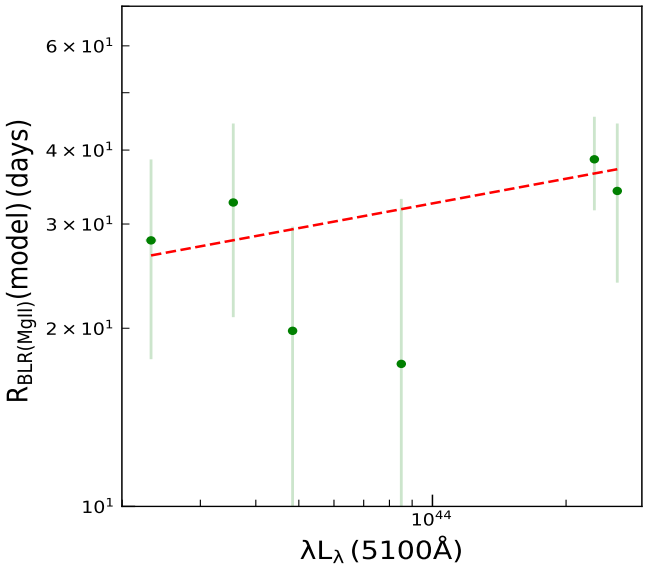

Figure 5.10: R_{BLR} versus the continuum luminosity at 5100 Å for objects with Mg II line light curves. The dashed red line represents the weighted linear least squares fit to the data points.

to the data gives

$$\log\left(\frac{R_{\mathrm{BLR}(H\alpha)}}{1\mathrm{day}}\right) = \beta + \alpha\log(\lambda L_\lambda)(5100) \tag{5.6}$$

with $\alpha = 0.19 \pm 0.12$ and $\beta = -6.86 \pm 5.16$ as shown by the dashed blue line. Using unweighted linear least squares fit to the data shown by dashed red line, we found

$$\log\left(\frac{R_{\mathrm{BLR}(H\alpha)}}{1\mathrm{day}}\right) = \beta + \alpha\log(\lambda L_\lambda)(5100) \tag{5.7}$$

with $\alpha = 0.47 \pm 0.08$ and $\beta = -19.10 \pm 3.67$ that closely matches with α=0.5 expected from simple photoionization arguments. The unweighted fit is found to be driven by a single data point at low luminosity. This point represents the object J1342+356 (NGC 5273), which has AGN luminosity of $\log L_{\mathrm{AGN}} = 41.534 \pm 0.144$ erg s^{-1} and a BLR size of $2.06^{+1.42}_{-1.31}$ days based on Hα line derived from the traditional CCF analysis by Bentz

et al. (2014). The size of the BLR obtained from our modeling approach is 2.29 ± 2.24 days which is similar to that obtained by Bentz et al. (2014) within errors.

We applied the model fitting for only six objects with Mg II line light curves. The relation between R_{BLR} and L_{5100} for those objects is shown in Fig. 5.10. Weighted linear least squares fit to the data gives

$$\log\left(\frac{R_{\mathrm{BLR}(MgII)}}{1\mathrm{day}}\right) = \beta + \alpha \log(\lambda L_{\lambda})(5100) \tag{5.8}$$

with $\alpha = 0.14 \pm 0.08$ and $\beta = -4.59 \pm 3.58$. The obtained relation between R_{BLR} and luminosity for objects with Mg II line light curves deviate from the value expected from photoionization argument due to the poor quality of measurement available on small number of sources. We need R_{BLR} measurements on large number of objects to firmly establish the relation between R_{BLR} and luminosity for Mg II emission lines and hence, the coefficients of Equation 5.8, needs to be taken with caution.

5.2.6 The Virial factor f_{BLR}

The virial factor f_{BLR} defined in Equation 1.1 depends on the geometry, kinematics and inclination of the BLR. One of the many advantages provided by the Bayesian based modeling approach on BLR adopted here is the capability to estimate f_{BLR}. For a BLR with disk-like structure, (see Collin et al., 2006; Li et al., 2013; Rakshit et al., 2015) f_{BLR} can be given as

$$f_{\mathrm{BLR}} \approx (\sin^2\theta_{\mathrm{opn}} + \sin^2\theta_{\mathrm{inc}})^{-1} \tag{5.9}$$

where, θ_{inc} represents the inclination angle and θ_{opn} is the opening angle of the disk. We calculated f_{BLR} for only those objects having $\theta_{opn} < 40^{\circ}$ following Li et al. (2013). Our obtained values of f_{BLR} are found to range

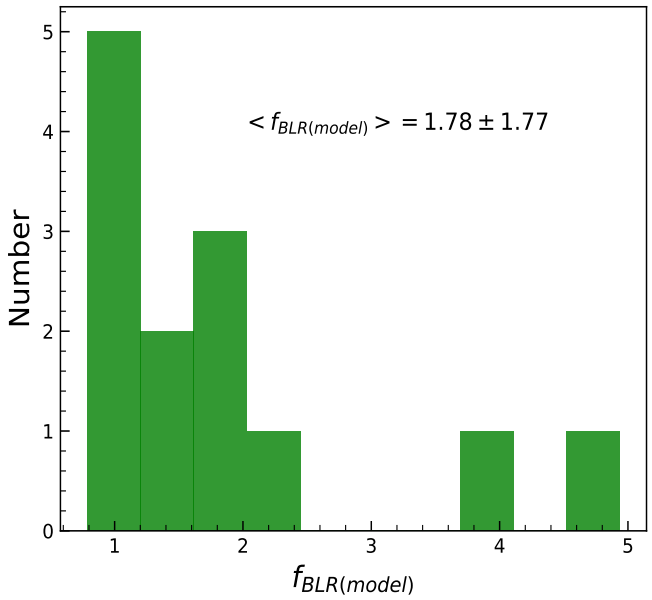

Figure 5.11: Distribution of the virial factor $f_{\rm BLR}$ measured for the objects analysed in this work.

from 0.79 to 4.94, with a mean value of 1.78 ± 1.77. A distribution of $f_{\rm BLR}$ is illustrated in Fig. 5.11. We found an average value of $< \log(f_{\rm BLR}) >$ = 0.17, which closely matches with the value of $< \log(f_{\rm BLR}) >$ = 0.18, obtained by Collin et al. (2006). The large error bars in our calculated $f_{\rm BLR}$ values are because of large uncertainties present in both $\theta_{\rm inc}$ and $\theta_{\rm opn}$.

$f_{\rm BLR}$ can also be estimated for objects that have measurements of stellar velocity dispersion. A tight correlation is found to exist between M_{BH} and bulge or spheroid stellar velocity dispersion (σ_*) for local inactive galaxies, given as (Ferrarese & Merritt, 2000; Gebhardt et al., 2000)

$$\log\left(\frac{M_{BH}}{M_\odot}\right) = \alpha + \beta \log\left(\frac{\sigma_*}{200\,\mathrm{km\,s^{-1}}}\right) \tag{5.10}$$

with $\alpha = 8.13 \pm 0.06$ and $\beta = 4.02 \pm 0.32$ (Tremaine et al., 2002). Considering AGN too follow the above equation, it is possible to estimate M_{BH}. By comparing this M_{BH} with the virial product, given as VP = $\left(\frac{\Delta V^2 R_{\rm BLR}}{G}\right)$

obtained by RM, we can get an estimate of $f_{\rm BLR}$ using the following relation

$$f_{\rm BLR} = \frac{M_{BH}^{\sigma_*}}{\rm VP} \tag{5.11}$$

We were able to obtain both the $f_{\rm BLR}$ measurements, one based on the BLR modeling based on Bayesian approach and the other obtained from the ratio of $M_{\rm BH}^{\sigma_*}$ to VP obtained from RM based on Equation 5.11 for a total of seven sources from our sample. Considering the dispersion of ~ 0.4 dex present in the $M_{\rm BH} - \sigma_*$ relation our modeling approach is able to give $f_{\rm BLR}$ consistent with that determined from RM method and $M_{\rm BH} - \sigma_*$ relation shown in Fig. 5.12. We found a Spearman rank correlation coefficient of $0.29^{+0.39}_{-0.54}$ with a p-value of $0.38^{+0.44}_{-0.31}$ from linear least squares fit to the data points in Fig. 5.12. Removing the most deviant data point with $f_{\rm BLR} > 10$, also the one with very large uncertainty, linear least squares fit gave Spearman rank correlation coefficient of $0.14^{+0.46}_{-0.51}$ and a p value of $0.47^{+0.40}_{-0.31}$. Though, the points are found to be scattered around the dashed y=x line in Fig. 5.12, the derived $f_{\rm BLR(model)}$ have large uncertainties resulting in no tight correlation between the scale factors obtained by both the methods. Most of the $f_{\rm BLR(model)}$ values are found to be lesser than 3 pointing to a BLR with a thick geometry viewed at an inclination angle. As $f_{\rm BLR}$ are found to have a large range, the $M_{\rm BH}$ obtained from single epoch measurements using a single $f_{\rm BLR}$ are bound to have large uncertainties. By comparing $M_{\rm BH}$ obtained from accretion disk model fitting and virial methods, Mejía-Restrepo et al. (2018) found that $f_{\rm BLR}$ is correlated with the width of the broad emission lines as $f_{\rm BLR} \propto {\rm FWHM}^{-1}$.

Also, Collin et al. (2006) and Goad et al. (2012) suggested a possible correlation between the inclination angle and the ratio of FWHM to the line dispersion of broad Hβ line. However, Pancoast et al. (2014) did not find any correlation from a small sample of 5 objects with good quality mea-

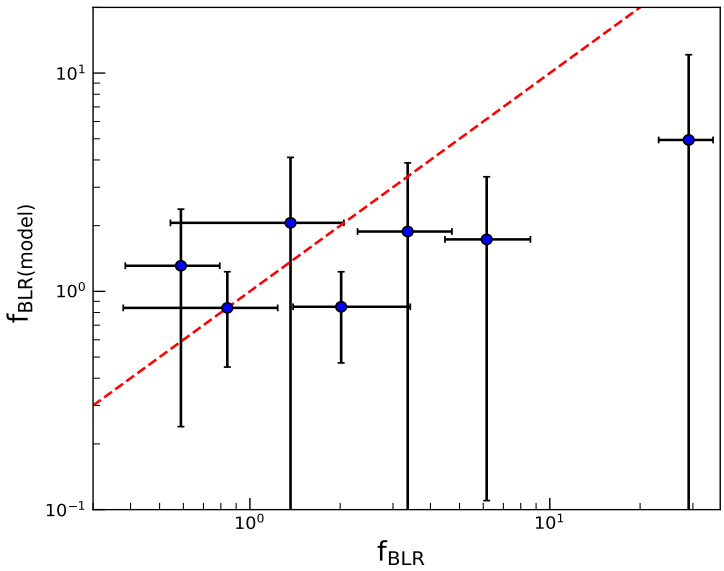

Figure 5.12: Comparison between $f_{\mathrm{BLR}(model)}$ obtained from model fits and f_{BLR} calculated from the ratio of M_{BH} from stellar velocity dispersion (σ_*) to the virial product (VP). The dotted red line is the y=x line.

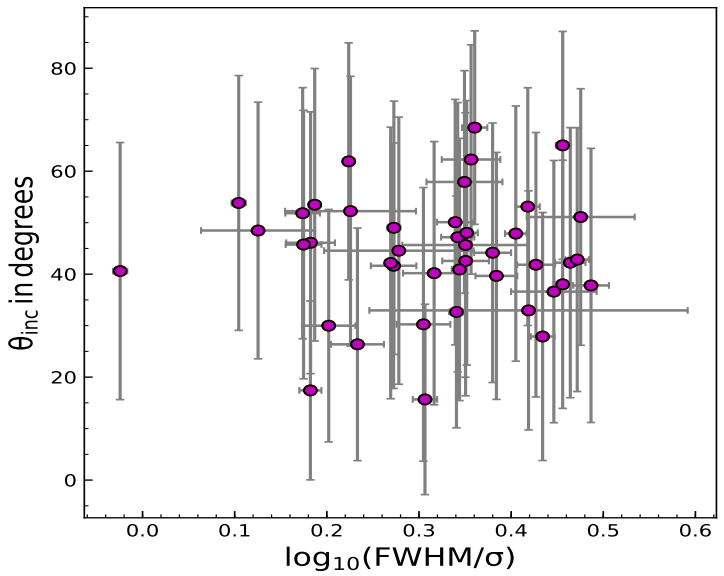

Figure 5.13: Inclination angle obtained from model as a function of the ratio of the FWHM to the Hβ line dispersion σ.

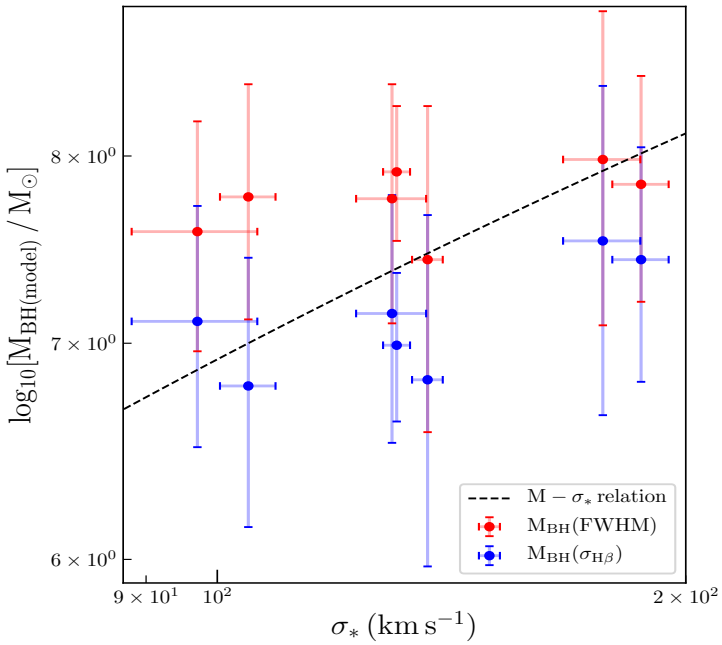

Figure 5.14: Comparison between the obtained black hole masses from the model and the M $-$ σ_* relation. The M $-$ σ_* relation is shown by the dashed black line.

surements. Using the available FWHM and line dispersion measurements obtained from the RMS spectra of broad Hβ line collected from the literature, we plotted the inclination angle from the model against the ratio of the FWHM to the line dispersion, shown in Fig. 5.13. We do not find any strong correlation between the inclination angle and the ratio of FWHM to the line dispersion of broad Hβ line, which agrees with the finding of Pancoast et al. (2014).

5.2.7 Measurement of M_{BH} and accretion rates

We calculated the black hole masses using Equation 1.1, where we adopted $f_{\rm BLR}$ and $R_{\rm BLR}$ of the Hβ line obtained from the model fitting. The velocity width ΔV can be determined either from the FWHM or from the line dispersion $\sigma_{\rm H\beta}$. The black hole masses were estimated for those 11 objects

Table 5.4: $M_{\rm BH}$ and accretion rate $\dot{M}$ measurements. Black hole masses are in solar mass unit.

α_{2000}	δ_{2000}	$\log(M_{\rm BH})$(FWHM)	$\log(M_{\rm BH})(\sigma_{\rm H\beta})$	$\dot{M}$
02:30:05.52	-08:59:53.2	7.98 ± 0.70	7.53 ± 0.70	0.018
06:52:12.32	+74:25:37.2	8.51 ± 0.85	7.67 ± 0.54	0.011
14:07:59.07	+53:47:59.8	7.91 ± 0.38	6.99 ± 0.37	0.232
14:10:31.33	+52:15:33.8	7.84 ± 0.63	7.43 ± 0.62	0.510
14:11:12.72	+53:45:07.1	7.58 ± 0.62	7.11 ± 0.61	2.266
14:13:18.96	+54:32:02.4	7.76 ± 0.66	7.15 ± 0.63	0.563
14:16:25.71	+53:54:38.5	7.75 ± 0.35	7.03 ± 0.33	2.188
14:20:39.80	+52:03:59.7	8.14 ± 0.60	7.27 ± 0.60	0.187
14:20:49.28	+52:10:53.3	9.29 ± 0.59	8.93 ± 0.58	0.002
14:21:03.53	+51:58:19.5	7.77 ± 0.65	6.79 ± 0.65	0.211
14:21:35.90	+52:31:38.9	7.43 ± 0.86	6.82 ± 0.85	0.420

which have $f_{\rm BLR}$(model) measurements using both FWHM and line dispersion $\sigma_{\rm H\beta}$, separately as $\sigma_{\rm H\beta}$ is found to give less biased $M_{\rm BH}$ measurement than using the FWHM (Peterson, 2011; Grier et al., 2012). In Fig. 5.14, we compared our obtained $M_{\rm BH(model)}$ values with the $M-\sigma_*$ relation as given in Equation 5.10. The Fig. 5.14 shows that most of the $M_{\rm BH(model)}$ measurements using FWHM lie above $M-\sigma_*$ relation, whereas most of the $M_{\rm BH(model)}$ values obtained using $\sigma_{\rm H\beta}$ are found to lie below the $M-\sigma_*$ line. But considering the errors all $M_{\rm BH(model)}$ measurements are found to be consistent with the $M-\sigma_*$ relation.

We also calculated the dimensionless accretion rate following the relation

given by Du et al. (2018)

$$\dot{M} = 20.1 \left(\frac{L_{44}}{\cos i} \right)^{3/2} m_7^{-2} \tag{5.12}$$

where, $m_7 = M_{\rm BH}/10^7\,{\rm M}_\odot$, $L_{44} = L_{5100}/10^{44} erg\,s^{-1}$ and i represents the inclination angle. Our derived values for those 11 objects as mentioned in Table 5.4 show low to moderately accreting black holes with $\dot{M}$ spanning from 0.002 to 2.266.

5.2.8 Reliability of the recovered model parameters: effect of signal to noise ratio

Modeling of the continuum and line light curves of AGN to derive various BLR parameters depends on the SNR of the light curves used. According to Collier et al. (2001) and Horne et al. (2004), BLR parameters can be well recovered with (a) continuum light curves of SNR $\approx$ 100 and (b) line light curves of SNR $\approx$ 30. But practically, it is often difficult to find RM dataset satisfying the above mentioned qualities simultaneously.

The SNR distribution of the continuum and line light curves used in this work is illustrated in Fig. 5.15 (top left), which shows that the SNR of the used light curves spans a wide range from as low as 5 to as high as 1000. The median SNR values of the continuum and line light curves are found to be about 84 and 30, respectively. To check for the effects of SNR on the estimated BLR parameters, we carried out simulations. In our simulation, we firstly selected sources having continuum light curves with SNR greater than 300. This results in a total of 10 objects from our sample. The SNR of the continuum and line light curves of those 10 objects were then degraded by multiplying a factor of 2, 3, 4, 5, 8, 10 and 15 to the original flux errors and adding a Gaussian random deviate of zero mean and standard deviation given by the new flux errors. We then extracted the BLR parameters by

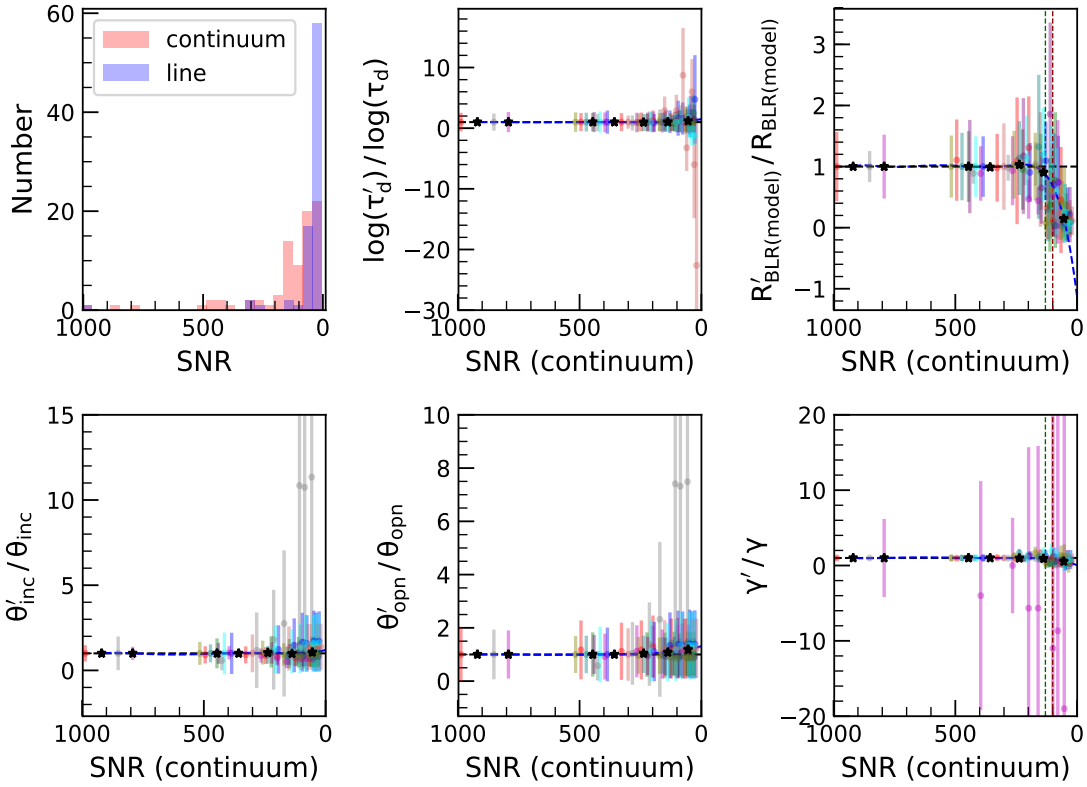

Figure 5.15: From top left to bottom right: Distribution of SNR of all the objects studied in this work in continuum and line and comparison of the recovered model parameters $\tau'_{\rm d}$, $\rm R'_{BLR(model)}$, $\theta'_{\rm inc}$, $\theta'_{\rm opn}$ and γ' from the SNR degraded simulated light curves to those obtained from the original light curves. Measurements from each object are shown by an unique colour. The sample median is also shown by a star marker. The dashed black lines are the y=1 lines, whereas the dashed blue lines are the best polynomial fit to the sample median values in each panel. The vertical green and red lines correspond to the SNR values where the comparisons deviate from the unit ratio by 10% and 30%, respectively.

applying the PBMAP code on the simulated light curves. The ratios of the recovered to the original BLR model parameters are plotted against their continuum SNR in Fig. 5.15. We notice from Fig. 5.15 that this ratio is close to unity for most of the BLR model parameters, except for the the BLR size. The radius of the BLR is found to deviate by 10% and 30%, when the continuum SNR are 130 and 100, as shown by the vertical green and red lines, respectively. In a similar way, for the line light curves too, we found that the ratios of the recovered to the original BLR model parameters are close to unity except for the BLR size, which deviates by 10% and 30%, when the line SNR are 25 and 15, respectively. These are also in agreement with the continuum and line SNR cut-off of 100 and 30, respectively, suggested by Collier et al. (2001) and Horne et al. (2004) to derive BLR parameters from RM data. We decided to adopt a SNR cut off of 100 and 15 for the continuum and line light curves, respectively. With this cut-off the derived model parameters are accurate to 70%.

We have a total of 82 different measurements of Hβ, Hα and Mg II lines for 57 objects studied in this work, out of which $\sim$ 42% of objects have continuum and line SNR greater than 100 and 15, respectively. We found consistent BLR size for all the objects obtained from model fits with those derived from conventional CCF analysis within the uncertainties. However, as the SNR is found to play a major effect on the estimated BLR size from the simulations, we note that the BLR sizes derived for sources with continuum and line light curves with SNR lesser than 100 and 15, respectively, need to be used with caution. We also performed an analysis of the correlation between τ_d and the BLR sizes obtained from the model to the luminosity restricting to those sources that have the continuum and line light curves SNR greater than 100 and 15, respectively. Though the trend of the correlation is found to be similar to that of the full sample, the

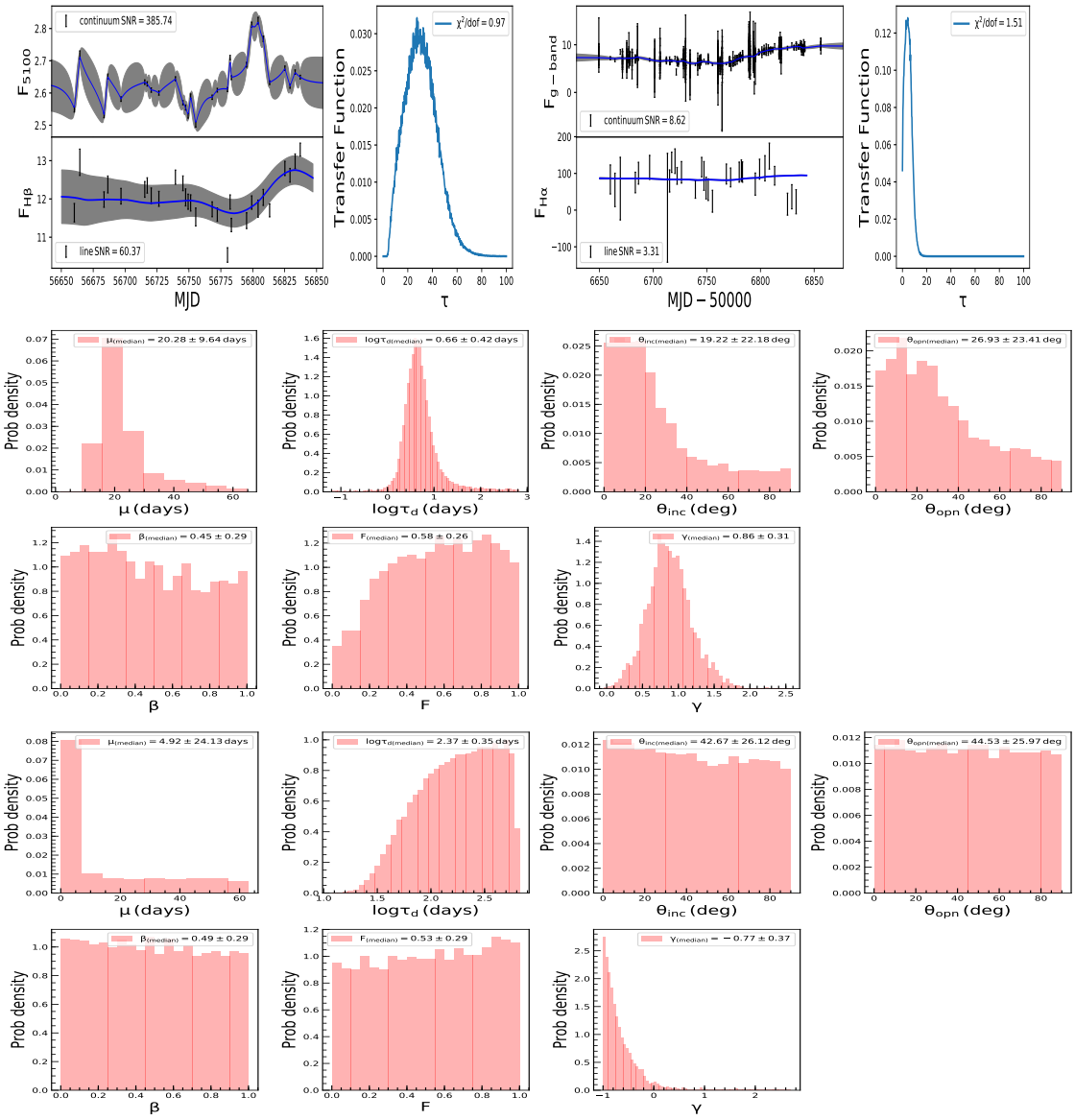

Figure 5.16: (Top) Model fits for the source (J1411+537) with high SNR light curves (left) and the source (J1417+519) with low SNR light curve (right). In the left-hand panels the data points with error bars are the observed light curves and the thick solid lines are the reconstructed light curves. The gray shaded areas represent the uncertainties in the reconstructed light curves. The corresponding transfer function for each objects is shown on the right hand panels. The SNR of the light curve is mentioned at each panel. Posterior probability distributions of different model parameters are also shown for J1411+537 (middle) and J1417+519 (bottom).

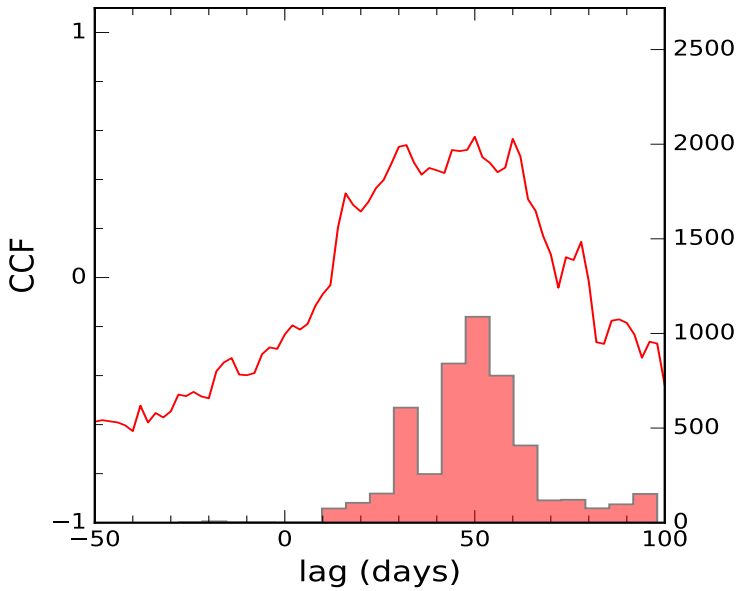

Figure 5.17: The red solid line is the average ICCF between g-band and Hα line light curves, while the histogram represents the centroid lag distribution for object J1420+526 with a $\tau_{\rm cent} = 49.88^{+11.99}_{-17.88}$ days in observed frame of the object.

significance of the correlation is not strong because of the small number of sources.

We show in Fig. 5.16, sample light curves and the recovered transfer functions for two sources. One belongs to J1411+537 with good quality light curves having continuum and line SNR of about 386 and 60, respectively. The other belongs to J1417+519, which has SNR of about 9 and 3 for the continuum and line light curves, respectively. From these examples, it is evident that the BLR model parameters are well constrained only for sources with good SNR data.

5.3 MEASUREMENT OF THE BLR SIZE OF J1420+526 BASED ON Hα LINE USING ICCF

Though Grier et al. (2017b) provided the RM data of g-band continuum and Hα line light curves for the source J1420+526, they did not perform CCF analysis to measure the Hα lag for this object. We estimated the Hα lag for this object using ICCF analysis method which is shown in Fig. 5.17. We found the lag and its uncertainty using a Monte Carlo simulation based on FR and RSS. The median of the cross-correlation centroid distribution is considered as the final lag, while uncertainties were estimated within a 68% confidence interval around the median value. We obtained the redshift corrected rest frame Hα lag of $32.22^{+7.75}_{-11.55}$ days from ICCF method. The estimated lag based on modeling approach is 46.67 ± 9.8 days which is found to be consistent with CCF lag within uncertainties.

5.4 SUMMARY

We analysed RM data taken from the literature for a total of 57 AGN which includes 50 objects with Hβ data, 26 objects with Hα data and 6 objects with Mg II line data. The main motivation is to constrain the kinematics and structure of the BLR that emits Mg II, Hβ and Hα lines. The results from this work are summarized below

1. Our estimated BLR sizes derived from the model fitting are found to be consistent with that obtained from the conventional CCF analysis, however, some objects do show large deviation. We found that the objects which show large deviation from the $R_{BLR}(\text{model}) = R_{BLR}(\text{CCF})$ line have poor quality light curves.

2. The best-fitted model Hβ BLR size is found to be correlated with op-

tical luminosity L_{5100} with a slope of 0.58 ± 0.03. This is similar to the known values found from the CCF analysis available in the literature. We also examined the correlation beween R_{BLR} (Hα) and the continuum luminosity at 5100 Å and obtained a slope of 0.47 ± 0.08 similar to what is expected from photo-ionization prediction. However, more measurements based on Hα are required to better constrain this correlation.

3. We estimated virial factor (f_{BLR}) from the derived geometrical model parameters and obtained a mean of 1.78 ± 1.77. The f_{BLR} estimated from the model parameter is consistent with that calculated from the ratio of M_{BH} from $M - \sigma_*$ relation to the virial product obtained from RM. It is difficult to constrain the virial factor f_{BLR} using line light curves only (Li et al., 2013). For that reason our measured f_{BLR} have large uncertainties due to large errors present in both θ_{inc} and θ_{opn} estimated from the model fitting.

4. We found the mean value of the non linearity parameter γ to be non zero for different lines pointing deviation from the linear response of the emission lines to the ionizing optical continuum. This may arise because of a) the anomalous behaviour of the BLR region due to the poor correlation between the observed optical continuum variability and the ionizing continuum variability (Edelson et al., 1996; Maoz et al., 2002; Gaskell et al., 2019) and b) anisotropic line emission originating from the partially optically thick BLR. The effect of this anisotropic emission is not considered in the model used here.

5. From the variability analysis of the sample, we found that emission lines vary more than the continuum. The damping time scale derived from the modeling is found to be positively correlated with the contin-

uum luminosity at 5100 Å.

6. From our simulation on the light curves, we conclude that reliable estimation of BLR size, as well as other parameters using the modeling approach requires continuum and line light curves with SNR greater than 100 and 15, respectively.

Chapter 6

QUASARS IN THE ILMT STRIPE [4]

An ideal way to select quasars for RM observations is to find quasars that are variable. The forthcoming 4 m ILMT will carry out deep imaging in a single scan of a narrow stripe of sky in the Time Delayed Integration (TDI) mode. A cadence of about 3 days in each of the g', r', i' bands observations will provide unique opportunities to discover new quasars, different types of supernovae (SNe) and many other types of variable sources. Such a data set will help one to select quasars for reverberation observations. An alternate way is to identify known quasars from already existing surveys that will be covered by the ILMT. Such a quasar catalogue can also serve as astrometric calibrators to bring the ILMT observations from the pixels coordinate system to the world coordinate (α, δ) system.

6.1 METHODS FOLLOWED AND THE DERIVED CATALOGUE

Quasars represent quasi-ideal astrometric reference sources with negligible proper motion (PM) and parallaxes and are thus suitable for use to carry out astrometric calibration (Souchay et al., 2015) of the ILMT survey. We, therefore, retrieved accurate position, PM and trigonometric parallax for all quasars available in the Milliquas catalogue (Flesch, 2017) and cross-correlated with the *Gaia*-DR2 database. This was done to select a subset of them for the ILMT use as *Gaia*, operated by the European Space Agency provides precise positions of celestial sources with milli-arcsec accuracy. We used the relation given by Varshni (1982) to calculate the absolute or resultant PM (μ)

$$\mu = (\mu_\alpha^2 cos^2\delta + \mu_\delta^2)^{1/2} \tag{6.1}$$

where, α and δ represent the RA and DEC, respectively. The $\mu_\alpha cos\delta$

[4]The contents of this chapter are based on Mandal et al. (2020)

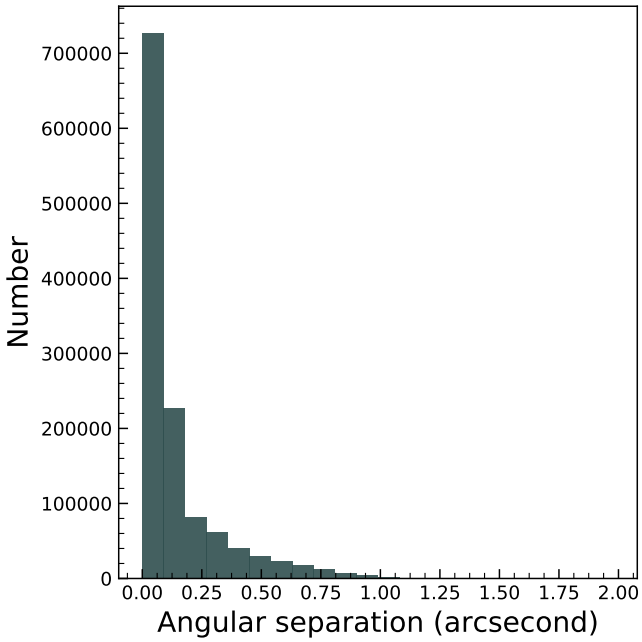

Figure 6.1: Distribution of the angular separation between the objects in the Milliquas catalogue and their counterparts in *Gaia*-DR2.

and μ_δ values were retrieved from the *Gaia*-DR2 database. We used the standard error propagation method to estimate the error in μ. We followed the following steps to arrive at a separate list of quasars visible to ILMT.

1. We cross-matched the nearly 2 million quasars in the Milliquas catalogue (Flesch, 2017) with the *Gaia*-DR2 within angular proximity lesser than 2". As a large fraction of the objects in the Milliquas catalogue comes from SDSS which has imaging data with seeing less than 2" (Ross et al., 2011), we used a 2" angular separation for cross-correlation. Cross-correlating the Milliquas catalogue with the *Gaia*-DR2, we obtained a sample of 1235600 objects spanning a range of redshifts up to $z = 6.4$. Fig 6.1 shows the distribution of the angular separation of the matched objects between the position in the Milliquas catalogue and that in *Gaia*-DR2. The angular separation has a range between 0 and 1.97" with a mean of 0.15" and a standard deviation of

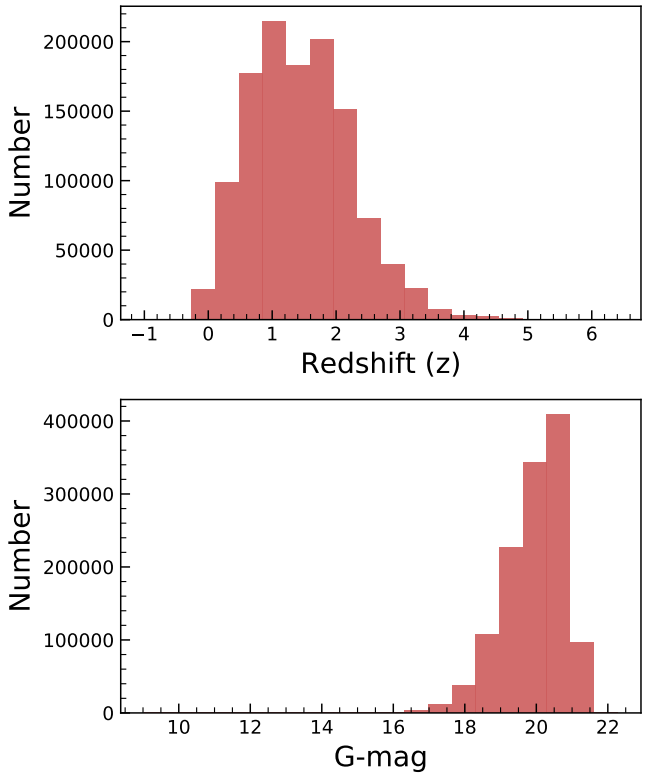

Figure 6.2: Distribution of redshift (top) and *Gaia* G-band magnitude (bottom) of the quasars selected from the Milliquas catalogue.

0.18". About 99.8% of the sources are found to match within 1". The distributions of redshift z and G-band magnitude of these objects are shown in Fig. 6.2.

2. *Gaia*-DR2 provides two important parameters which are relevant for quasar target selection. They are the astrometric excess noise (ε_i) and its significance, namely the astrometric excess noise significance (D). Excess noise ε_i gives the disagreement between the observations and the standard best-fitting astrometric model adopted by *Gaia* (Lindegren et al., 2012). A source is found to be astrometrically well behaved for $\varepsilon_i = 0$, and a value of $\varepsilon_i > 0$ implies that the residuals are statistically larger than expected. However, practically it is possible

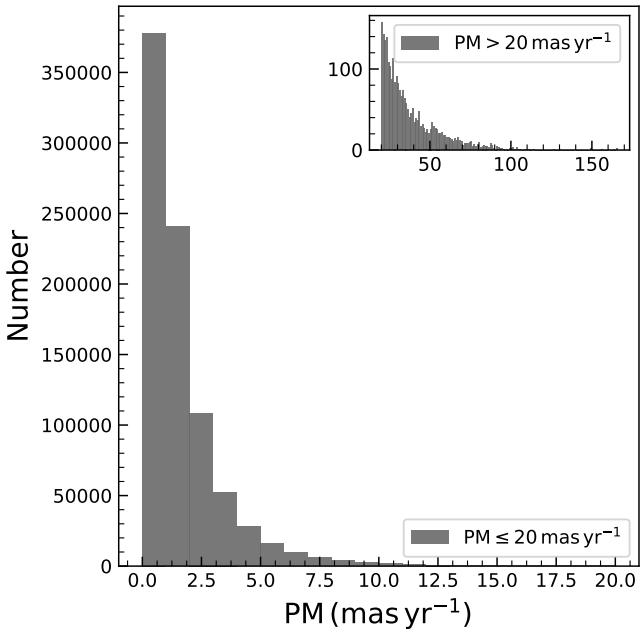

Figure 6.3: The PM distribution of the quasars in the Milliquas catalogue with D $\leq$ 2. There are about 2615 quasars found with PM $>$ 20 $mas\,yr^{-1}$ and their PM distribution is shown in the small box on the same figure.

that some sources may not behave exactly as per the adopted astrometric model. Therefore, to signify ε_i, *Gaia*-DR2 provides another parameter, namely significance of excess noise D (Lindegren et al., 2012). ε_i is probably not significant if D $\leq$ 2, and the source may be astrometrically well-behaved even if ε_i is found to be large[1]. Hence, we only selected objects with D $\leq$ 2 from *Gaia*-DR2. This resulted in a total of 1047747 quasars that cover the whole sky. For these 1047747 quasars, we calculated PM using Equation 6.1. The PM distribution of those objects is shown in Fig. 6.3. From this figure, it is obvious that except for a few sources (about 0.25%), most of them have PM $<$ 20 $mas\ yr^{-1}$ with a mean value and standard deviation of 1.808 $mas\,yr^{-1}$

[1] https://gea.esac.esa.int/archive/documentation/GDR2/Gaia_archive/chap_datamodel/sec_dm_main_tables/ssec_dm_gaia_source.html

and 2.878 $mas\,yr^{-1}$, respectively.

3. From the list of quasars that cover the whole sky, obtained at step 2 above, we constructed a separate catalogue of quasars for the ILMT stripe. The ILMT is being installed at the Devasthal observatory, located at a latitude near 29°22′26” (Surdej et al., 2018). The ILMT stripe has a width of ∼27’. However, because of precession, the ILMT sky at the zenith will change over time as illustrated in Fig. 6.4. We found that if we consider a $\sim 34'$ wide stripe instead of $\sim 27'$, the effect of precession during the next 10 years will be compensated. So, we selected only those sources with δ in the range $29.09° \leq \delta \leq 29.66°$ and G-mag $\leq$ 21 as *Gaia* has a limiting G-band magnitude of 21 mag[2], from the sample of 1047747 quasars obtained from step 2 since only these will be visible for observations with the ILMT. This yielded a total of 6904 quasars. For slightly less than 2% of these, the redshift information is not available in the Milliquas catalogue. Excluding those, finally, we arrived at a catalogue of 6755 quasars available in the ILMT stripe. Varshni (1982) claimed the existence of quasars with high PM, namely PHL 1033, LB 8956 and LB 8991 with PM values of 0.049 ± 0.013, 0.061 ± 0.018 and 0.050 ± 0.018 $arcsec\,yr^{-1}$, respectively. We checked their PM values in *Gaia*-DR2 and found PM values of 0.121 ± 0.435, 0.188 ± 0.151 and 0.056 ± 0.072 $mas\ yr^{-1}$ for PHL 1033, LB 8956 and LB 8991, respectively.

4. The distribution of PM of those 6755 objects as a function of their G-band brightness is shown in Fig. 6.5. From this figure, we found that the majority of the quasars have PM $<$ 20 $mas\,yr^{-1}$. Only 17 quasars in this list are found with PM $>$ 20 $mas\,yr^{-1}$ with *Gaia* G-

[2] https://www.cosmos.esa.int/web/gaia/dr2

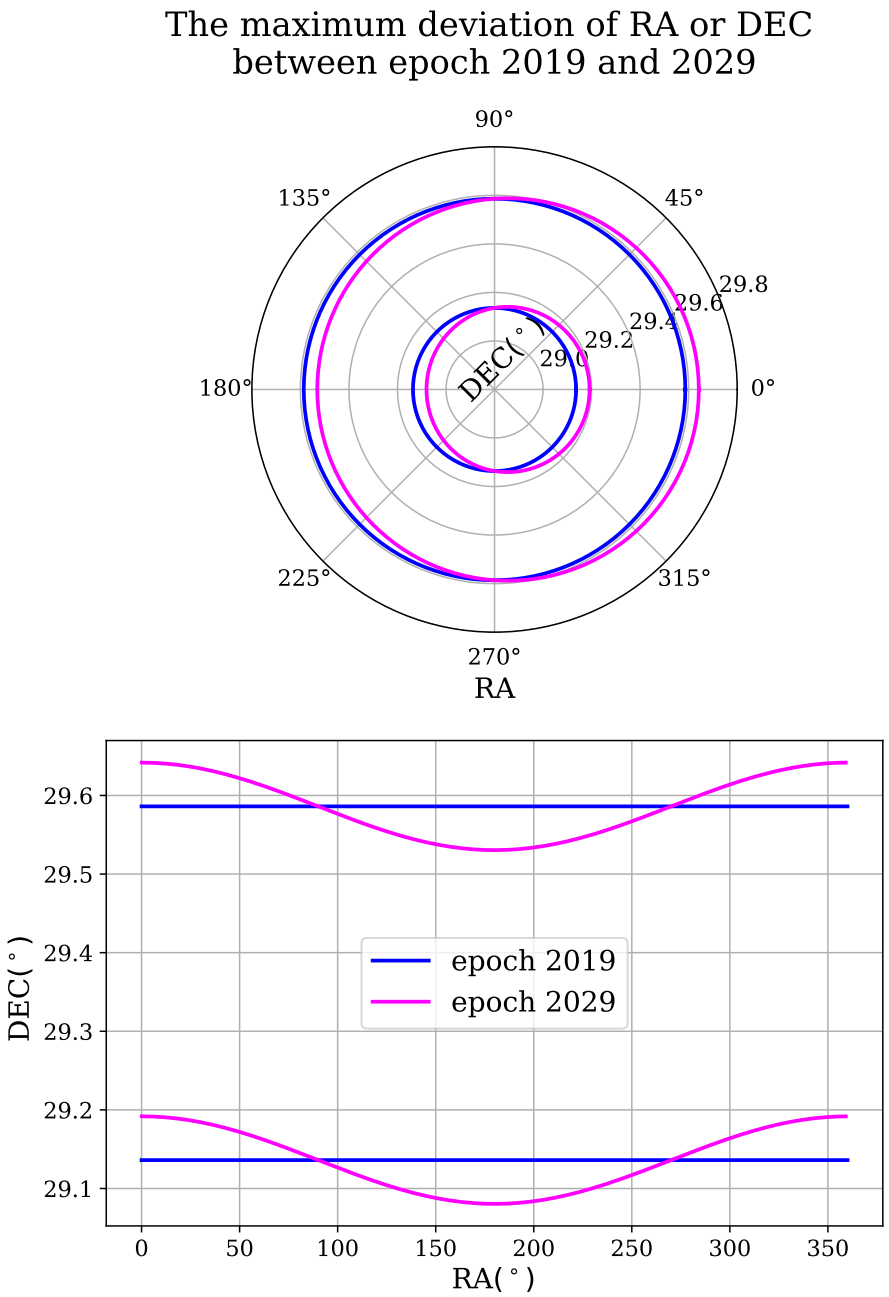

Figure 6.4: (Top) Polar representation of the astrometric deviation of the ILMT stripe between the 2019 and 2029 epochs because of precession. (Bottom) Deviation in astrometry between the 2019 and 2029 epochs assuming the original ILMT stripe to be rectangular in 2019 (blue lines) and pink lines represent the same in 2029.

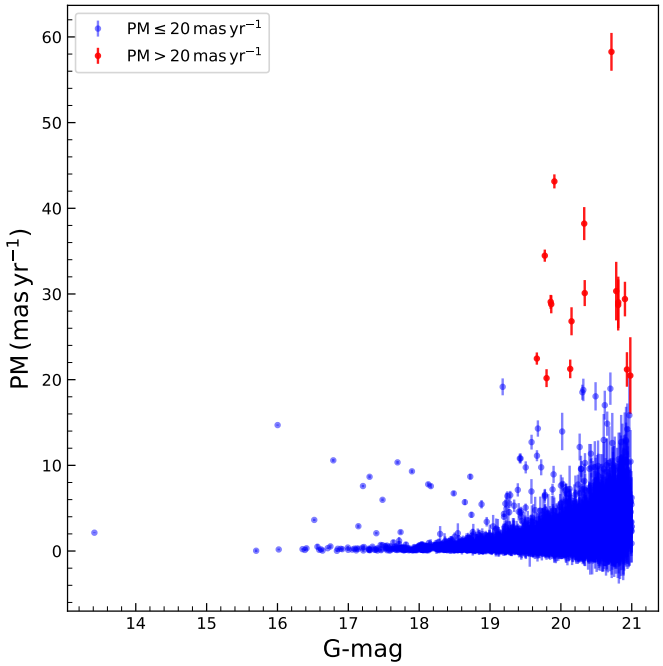

Figure 6.5: Proper motion as a function of G-mag of the quasars in the ILMT stripe.

band magnitude $>$ 19.5. The nature of these 17 objects could not be ascertained because of the lack of their optical spectra. Hence, we excluded those 17 quasars from our list and arrived at a final sample of 6738 quasars that will be available within the ILMT stripe and could be used as astrometric calibrators.

5. The distributions of redshifts, *Gaia* G-band magnitude and parallax of the ILMT quasars are shown in Fig. 6.6. The ILMT quasars span redshifts up to $z = 4.9$. Their distribution in the galactic coordinate system is also illustrated in Fig. 6.7. An outlay of the sample catalogue and the description of its columns are given in Table 6.1 and Table 6.2, respectively. The full catalogue is available at $https://doi.org/10.1007/s12036-020-09642-x$.

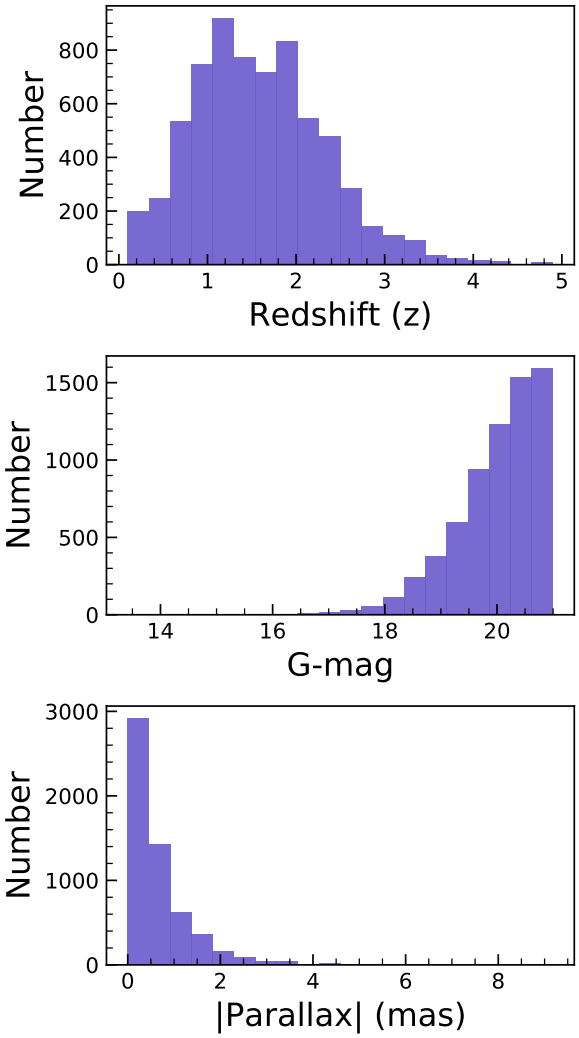

Figure 6.6: Distributions of the redshift, G-band magnitude and absolute parallax of the selected quasars in the ILMT stripe.

Table 6.1: An outlay of The ILMT Quasar (IQ) catalogue. The column information of this table is given in Table 2. The full catalogue is available at $https://doi.org/10.1007/s12036-020-09642-x$.

ID-1	RA	RA-ERR	DEC	DEC-ERR	z	...	...	PM-DEC	PM-DECERR	EPSILON	D
(1)*	(2)*	(3)*	(4)*	(5)*	(6)	...	...	(16)*	(17)*	(18)	(19)
2.85518e+18	0.06120	0.54785	29.23513	0.28529	1.90	...	...	1.31259	0.50398	0.00	0.00
2.85525e+18	0.07183	0.22781	29.50171	0.15339	1.40	...	...	0.27730	0.26071	0.00	0.00
2.85525e+18	0.10806	0.62917	29.50235	0.56513	2.51	...	...	-1.02912	1.06549	1.44	0.87

*The values are shown up to 5 decimal places, the original values taken from the *Gaia*-DR2 catalogue are mentioned in the IQ catalogue available at $https://doi.org/10.1007/s12036-020-09642-x$.

Table 6.2: Column information of the ILMT Quasar (IQ) catalogue.

Number	Column Name	Format	Unit	Description
1	ID-1	String		Object name as given in *Gaia*-DR2
2	RA	Double	degree	Right Ascension (J2000)
3	RA-ERR	Double	*mas*	Error in Right Ascension retrieved from *Gaia*-DR2
4	DEC	Double	degree	Declination (J2000)
5	DEC-ERR	Double	*mas*	Error in Declination retrieved from *Gaia*-DR2
6	z	Double		Redshift
7	ID-2	String		Object ID in the Milliquas catalogue
8	TYPE	String		Classification of the object
9	PROB	Double		Probability that the object is a quasar•
10	MAG	Double		*Gaia* G-band magnitude
11	MAG-ERR	Double		Error in *Gaia* G-band magnitude
12	PLX	Double	*mas*	Parallax
13	PLX-ERR	Double	*mas*	Error in parallax
14	PM-RA	Double	$mas\,yr^{-1}$	Proper motion in RA
15	PM-RAERR	Double	$mas\,yr^{-1}$	Error in proper motion in RA
16	PM-DEC	Double	$mas\,yr^{-1}$	Proper motion in DEC
17	PM-DECERR	Double	$mas\,yr^{-1}$	Error in proper motion in DEC
18	EPSILON	Double		Astrometric excess noise
19	D	Double		Significance of excess noise

• The details on how the probability is calculated to each quasar can be found in Flesch (2015).

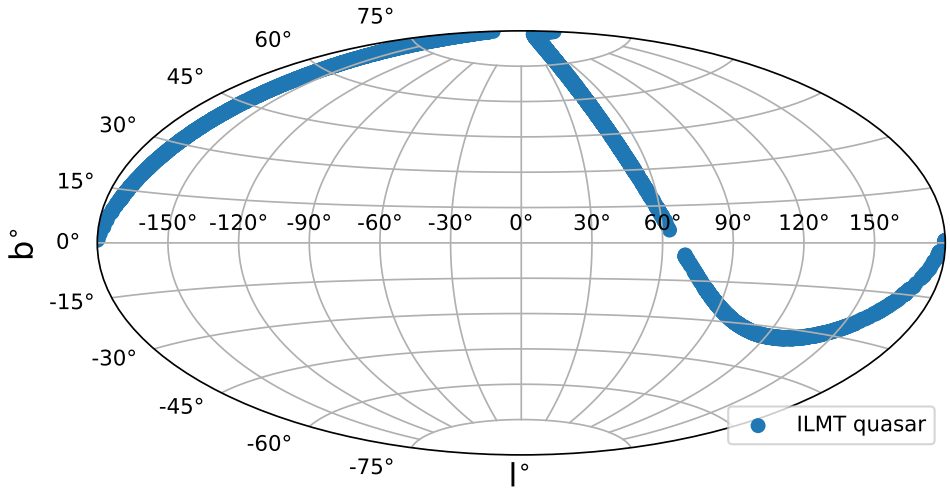

Figure 6.7: Sky distribution of the ILMT quasars in the galactic coordinate system. The real surface density of quasars is not considered here.

6.2 APPLICATIONS OF THE CATALOGUE

The upcoming ILMT will be continuously scanning a stripe of the sky passing over the zenith in time delayed integration (TDI) mode. Such an observational strategy will be of interesting use for a vast range of astrophysical applications like the detection of many extragalactic objects, such as supernovae, galaxy clusters, AGN/quasars, gravitationally lensed systems etc. (Surdej et al., 2018). Also, as it will be scanning repeatedly the zenith region, such accumulated observations will be very convenient for studies of photometric variability of different types of celestial objects. We describe below some of the potential astrophysical applications of our obtained quasar catalogue of 6738 sources that will be covered by ILMT.

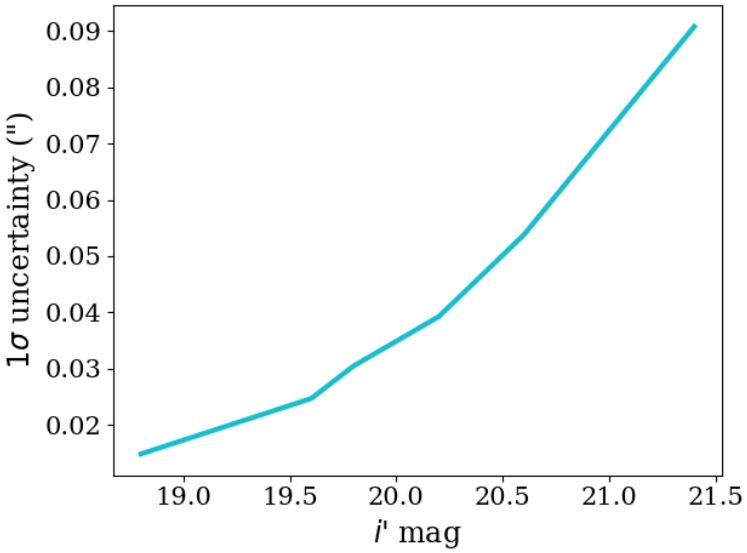

Figure 6.8: The uncertainty 1σ in the astrometric position of the point sources as a function of i' magnitudes in the ILMT CCD images.

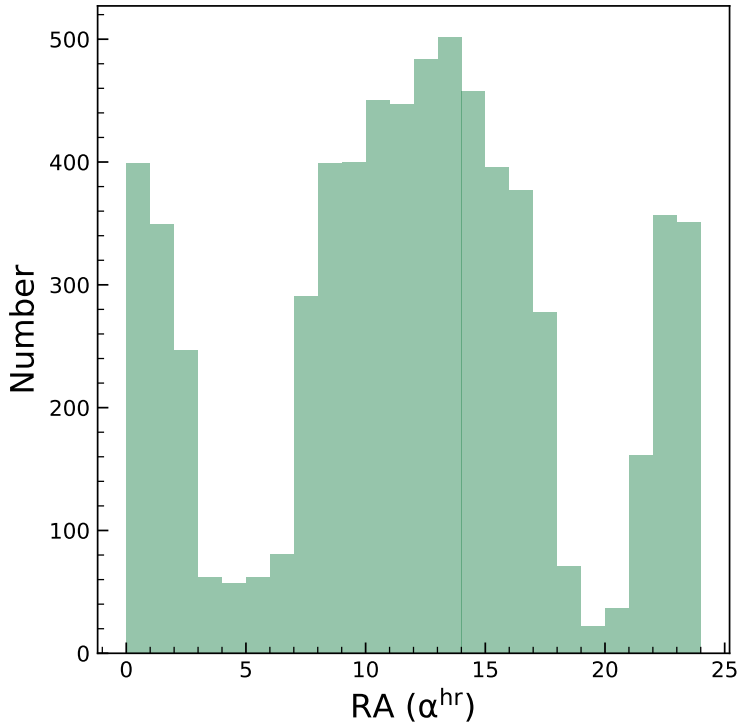

Figure 6.9: Distribution of the ILMT quasars in RA.

6.2.1 Astrometric calibration of the ILMT field

The main application of our derived quasar catalogue is to carry out astrometric calibration of the ILMT observations. As this catalogue provides accurate positions retrieved from the *Gaia*-DR2, with accuracy of the order of a few *mas*, we expect to achieve sub-arcsec astrometric accuracy using these quasars in the ILMT survey. To estimate the astrometric accuracy for the survey, we performed a Monte Carlo simulation. Considering median seeing at Devasthal observatory of 1.1" (Sagar et al., 2000, 2019) and the pixel scale of 0.4", we generated several synthetic CCD frames with a circular Gaussian point spread function at random locations for different SDSS i' magnitudes assuming a single scan of exposure time of 102 seconds as demonstrated by Kumar et al. (2018). We used the SOURCE EXTRACTOR (SEXTRACTOR) software (Barbary, 2016) to find the centroid of each synthetic source. The accuracy (1σ) in estimating the centroid of a point source with a limiting i' magnitude of 21.4 mag was found to be 0.09" (see Fig. 6.8) for the ILMT.

The distribution of the selected ILMT quasars in RA is illustrated in Fig. 6.9, which shows that the ILMT quasars cover the entire range of RA, however, in the RA range between $3-6$ hr and between $19-21$ hr, the numbers of quasars are found to be around 60 and 20 per hour angle in the ILMT stripe, respectively, much lower than the quasars available in the other RA ranges. In this RA range, we need to compromise with a separate catalogue of astrometric standards, such as the Tycho-2 catalogue (Høg et al., 2000) having an astrometric uncertainty of 0.06" per coordinate and an average star density of $\sim$180 per hour angle. Therefore, after adding this uncertainty of the Tycho-2 catalogue in quadrature to our estimated 1σ, the positional accuracy detectable by the ILMT for the faintest stars

will be degraded to 0.11" in those RA ranges.

6.2.2 Quasar variability

Quasars show optical flux variations over time. Optical flux variations of quasars have been studied over diverse time scales ranging from minutes to days (Wagner & Witzel, 1995; Ulrich et al., 1997). But most of the studies carried out till now, are limited by the time resolution of the observations resulting in gaps in the time series data. The ILMT has a 4K×4K CCD camera, which can operate over the 4000 to 11000 spectral range in three different SDSS equivalent filters, such as g', r' and i' with a typical exposure time of a single frame of ∼104 s (Surdej et al., 2018). Only one of those filters can be operated throughout a single night. The ILMT will be able to collect good quality data for most of the quasars that we obtained for the ILMT stripe, primarily for astrometric calibration. Monitoring observations in different bands can also be used to study their colour variability. It is also possible to discover new candidate quasars based on the colour-colour diagram (Richards et al., 2002) and/or optical variability characteristics (Graham et al., 2016), when more epochs of observations will be available from the ILMT in the future.

6.2.3 Variability of lensed quasar

Gravitational lensing which is caused due to the effect of deflection of light by a foreground intervening compact object, such as galaxy, cluster, etc., comprises a powerful tool that has many applications in astrophysical areas. Multiply imaged quasars are formed because of the gravitational lensing of distant quasars (Ehlers & Schneider, 1992; Narayan & Bartelmann, 1999). By measuring the time delays of such lensed quasars that show photometric variations through cross-correlating their light curves, it is possible to

determine the Hubble-Lemaître constant H_0 (Refsdal, 1964, 1966) to constrain the dark energy equation of state (Kochanek & Schechter, 2004). Till now, only 24 lensed quasars were studied to measure time delays that range from a few days to a few years between multiply imaged quasars (Rathna Kumar et al., 2015). Long term monitoring observations of lensed quasars are required to measure such time delays. Among the quasars catalogued for ILMT, we have only identified one gravitational lensed quasar, namely J1251+295 (α_{2000} = 12:51:07.57, δ_{2000} = 29:35:40.50) having 4 lensed images with maximum angular separation of $\sim$ 1.8". As the median seeing at Devasthal site is of the order of 1.1", these lensed images of J1251+295 can be easily resolved with the ILMT. Thus, the ILMT will be able to provide good quality light curves for this source as well as for many others. Moreover, once the ILMT becomes operational, it also expects to detect about 50 new multiply imaged quasars (Surdej et al., 2018) that opens up the ability of the ILMT to acquire more time delays among lensed quasars.

6.3 SUMMARY

Reverberation monitoring observations require quasars that are variable. The upcoming ILMT will be repeatedly scanning the sky that passes over it and therefore, the data from ILMT will allow one to find variable quasars. Therefore, it is ideal to have a list of quasars that will be covered by ILMT. Such a catalogue of quasars will also be of use as calibrator sources to convert the ILMT observations to the world coordinate system. This work was aimed to construct a catalogue of quasars falling in the ILMT stripe. The results of this work are summarized below

1. After cross-matching the Milliquas catalogue with the *Gaia*-DR2, and applying the condition of the matched sources to have astrometric

excess noise significance D $\leq$ 2, we obtained a sample of 1047747 quasars covering the whole sky. Of these, 6755 quasars are found in the ILMT stripe.

2. From the distribution of proper motion of these 6755 quasars, it was found that only 17 sources ($\sim$0.3%) have a PM greater than 20 $mas\,yr^{-1}$. As the nature of these 17 objects could not be established because of the lack of their optical spectra, we excluded them from our list. Thus, all quasars in the ILMT field have PM lesser than 20 $mas\,yr^{-1}$.

3. Our final ILMT quasar (IQ) catalogue contains 6738 quasars. Out of which, according to the Milliquas catalogue, 2405 are type I quasars confirmed from spectroscopic observations with broad emission lines, 3 are found to be AGN, 7 are BL Lac objects, 1 is a Type II AGN and 4322 objects are selected through photometric observations with a probability of $>$ 90% to be quasars. In addition to use quasars as astrometric calibrators, the catalogue that is made available in this work, can also serve as a large sample for quasar variability studies, which in turn can be used for RM study.

4. Using our obtained quasar catalogue, we expect to achieve an astrometric accuracy of better than 0.1" in the ILMT survey.

Chapter 7

SUMMARY AND FUTURE PROSPECTS

7.1 SUMMARY

Probing the central regions of AGN via the method of reverberation mapping is an established technique for more than three decades (Gaskell & Sparke, 1986; Gaskell & Peterson, 1987). Several observational programs carried out in the interim have increased the number of sources with known BLR and dusty torus size. These observational programs led to the acceptance of a general trend between R_{BLR} and the continuum luminosity as well as R_{torus} and the continuum luminosity. Also, very recently, advancements in observational techniques have lead to direct imaging of a few nearby AGN using very long baseline interferometry at the Very Large Telescope, at the European Southern Observatory. This is limited to bright and nearby sources. Therefore, there is a need to increase the number of sources with measured BLR and dust torus size that covers a range of redshift and luminosity to refine the correlations already known from observations that cover a limited luminosity range. This leads to the present program called REMAP that aims to observe more number of AGN to determine the dust torus size and BLR size. Such a program to determine the size of the BLR, using Indian observational facilities was undertaken for the first time about a decade ago (Stalin et al., 2011). Besides, RM data acquired as part of BLR reverberation in addition to determining BH mass, in conjunction with theoretical model can also be used to constrain the structure and dynamics of BLR in AGN. This kind of theoretical modeling using observed data were applied to a few AGN in the past to recover various model parameters that characterize the line emitting region.

The observational strategy followed in this present study is to carry out good SNR and time sampling observations of more AGN to get BLR as well as the torus size. We summarize the main results obtained from this

work here and also outline extensions of this project that will be pursued in the future. The major findings of the present study are

1. Using the technique of photometric reverberation, we found a lag between the continuum and Hα line in Mrk 590 to be $21.44^{+1.49}_{-2.11}$ days. Based on the light travel time argument the average BLR size based on Hα line is 0.018 pc from the central ionizing continuum region. This is in agreement with the lag obtained between the continuum and Hβ (lag = $20.7^{+3.5}_{-2.7}$ days) obtained from spectroscopic reverberation. This new measurement also lies on the known R_{BLR} − luminosity plot by Bentz et al. (2013), which was obtained based on Hβ-lag measurements. Using single epoch spectrum, we found the black hole mass for Mrk 590 to be $1.96^{+0.15}_{-0.21} \times 10^8\,M_\odot$ using Hα line.

2. We found the inner extent of the dusty torus in two AGN, namely H0507+164 and Z229−15 for the first time. We found R_{torus} = 0.029 and 0.017 pc for H0507+164 and Z229−15, respectively. These two new measurements also nicely fit into the R_{torus} − luminosity relation obtained based on the monitoring of about three dozen AGN. Our analysis carried out on Z229−15 disfavours the use of constant spectral index α to correct for the accretion disk contamination to the observed near infrared emission, as α is found to be correlated significantly with the B and V band fluxes with a bluer when brighter trend.

3. By compiling line and continuum light curves from the literature for a sample of 57 AGN, and by following the Markov chain Monte Carlo approach, we were able to determine the structure and other characteristics of BLR. Our analysis indicates that the BLR model parameters are well recovered for RM data with continuum and line SNR greater than 100 and 15, respectively.

4. As reverberation mapping observations rely on the variability nature of quasars, it is ideal to observe quasars that are known to be variable. The upcoming survey with the ILMT will provide good cadence data, which will enable one to pre-select variable quasars for further reverberation monitoring. Towards this, we have identified 6738 known quasars that lie in the ILMT stripe. Future ILMT observations will quantify their variability nature. This new quasar catalogue can also serve as astrometric calibrators to bring the ILMT observations in the world co-ordinate system.

7.2 FUTURE PLAN

As an extension of the research work carried out in this thesis, I plan to pursue the following research activities in the future.

7.2.1 Continuum reverberation

From the standard accretion disk model (Shakura & Sunyaev, 1973) the accretion disk temperature is found to depend on the radius as $T \sim R^{-3/4}$. So, the hot, inner parts of the accretion disk emit UV photons, whereas the cooler, outer parts emit in the optical and NIR. Therefore, there will be a time delay between the ionizing UV continuum and optical continuum variations that is proportional to the size of the accretion disk (Krolik et al., 1991). While Fausnaugh et al. (2017) and Kokubo (2018) were able to find a wavelength dependent accretion disk sizes, most attempts to measure continuum lags have not been able to detect time delays at $> 3\sigma$ (Sergeev et al., 2005; Arévalo et al., 2008; Breedt et al., 2010; Jiang et al., 2017). So, it is required to study more AGN to better constrain the accretion disk size and check the consistency with standard model via observing them in different UV and optical bands, simultaneously.

7.2.2 Constraining the location of the corona via X-ray reverberation

In radio-quiet AGN, X-rays, which are produced in the X-ray corona via inverse Compton scattering of the optical and UV accretion disk photons, can either be observed directly as the X−ray continuum or it can get back-scattered off from the disk as the reflection component. Depending on the location of the corona, time delays between the direct and reflection components are expected. Such X-ray reverberations lags are known since 2009. Efforts will be taken to study a few sources to constrain the location of the corona in AGN using existing X-ray data.

7.2.3 BLR reverberation to estimate black hole masses

By carrying out spectroscopic monitoring of AGN (hereafter referred to as spectroscopic reverberation), it is possible to estimate the mass of the black hole using the principle of the delayed response of the emission lines arising from the BLR in response to changes in the central ionizing continuum. As of now, only about 117 AGN have been monitored for spectroscopic RM. These targets have inherent selection biases as they have been selected based on a combination of factors, such as their apparent brightness as well as their favourable position in the sky. Due to the way these sources were selected/observed, they are limited to only redshifts lesser than 0.3 with about 70% of them having z < 0.05 and having luminosities ranging from $10^{42}\,\mathrm{erg\,sec^{-1}}$ to $10^{46}\,\mathrm{erg\,sec^{-1}}$. Also, the now known relationship between the radius of the BLR and the luminosity of AGN is based on sources with z < 0.3 and with optical luminosity between $10^{42}\,\mathrm{erg\,sec^{-1}}$ to $10^{46}\,\mathrm{erg\,sec^{-1}}$. It is not clear if this same linear trend holds for sources with optical continuum luminosity lesser than $10^{42}\,\mathrm{erg\,sec^{-1}}$ and for sources with optical continuum luminosity greater than $10^{46}\,\mathrm{erg\,sec^{-1}}$. It is therefore, impera-

tive to extend reverberation mapping estimates for sources with lesser luminosity ($L < 10^{42}\,erg\,sec^{-1}$) as well as sources with higher luminosity ($L > 10^{46}\,erg\,sec^{-1}$) than sources that are currently studied using RM observations. An ideal way to fill the low luminosity end is to monitor AGN with low mass BH ($10^5 - 10^7\,M_\odot$). Efforts will be made to observe a few low luminosity AGN, with the expected outcome of (a) getting new black hole masses and (b) to check if the as of now known linear relationship between the radius of the BLR and luminosity of the AGN extends to low luminosities as well.

To execute the above objective, I would like to explore the possibility of carrying our photometric RM using a set of narrow band filters available at the 2 m HCT and the 1.3 m telescope in Devasthal. Such a dedicated observational campaign using the 2 m class telescope will have a lasting value in the field of AGN.

7.2.4 Estimating the size of the inner edge of the dusty torus in AGN through simultaneous optical, infrared photometry and spectroscopy

The method of dust reverberation mapping (DRM) as of now has been applied to about forty AGN to measure the inner rim of the torus (Suganuma et al., 2006; Koshida et al., 2014; Mandal et al., 2018; Minezaki et al., 2019; Mandal et al., 2021c). These measurements carried out on 2 m class telescopes have (a) large error bars due to gaps in the time series data and (b) incomplete treatment of the contribution of the accretion disk emission to the observed IR emission (a constant spectral index is assumed in existing studies, while in reality AGN are known to show spectral variations). Conventionally DRM is carried out via photometric monitoring observations in optical V and NIR J, H and K bands. These observations

are either simultaneous or quasi-simultaneous and the contribution of the accretion disk emission to the observed IR emission are not taken into account properly. Imaging observations in optical filters, such as B and V bands and NIR K band can be carried out to measure the inner radius of the dust torus by finding the lag between V and K-band. In this observing plan, the observations in the optical B and V bands can be used to derive the spectral index α, which can then be used to correct for the contribution of accretion disk emission to the observed NIR fluxes. Alternatively, DRM observations that may overcome many uncertainties of photometric observations are via spectroscopy that has the capability to cover the optical and IR region. One such instrument is TANSPEC mounted on the 3.6 m Devasthal Optical Telescope (DOT), Nainital, India, as it provides simultaneous wavelength coverage from 550 nm to 2450 nm. TANSPEC observations will enable us to obtain optical spectral index at individual epoch which can be used to properly correct for the accretion disk contamination to the NIR fluxes. From TANSPEC spectra, we will derive several optical and near IR light curves suitable to get the (a) time lag between the optical and different IR bands to probe the structure and kinematics of different emitting components in the torus, (b) time lag between optical and K-band to find the radius of the inner edge of the torus and (c) lag between optical continuum and line emission from the obtained spectra and subsequently, measure black hole mass for the same object. I intend to carry out this on the 3.6 m DOT.

7.2.5 Study of lensed quasars: determination of Hubble-Lemaître constant H_0

If there is an intervening mass between a distant background quasar and the observer, the light rays from the background quasar will be bent due

to the gravitational field of the intervening mass resulting in the formation of multiple images that depend on the alignment of the quasar, lens and the observer. This phenomenon, known as gravitational lensing, results in the formation of multiply imaged quasars. It is possible to determine the Hubble-Lemaître constant H_0, which can constrain the dark energy equation of state by finding lag between the light curves obtained for multiply imaged quasars. Till now, there are a total of 218 known gravitationally lensed quasars (Lemon et al., 2018), of which for around 24 gravitationally lensed quasars, time delays have been reported in the literature (Rathna Kumar et al., 2015). So, each gravitational lensed quasar is important to constrain the cosmological parameters. Finding more and more gravitationally lensed quasars is very much needed. The upcoming 4 m ILMT can play an important role to find more new lensed quasars which can be confirmed from spectroscopic data acquired at the 3.6 m DOT. Besides, once the ILMT becomes operational, light curves for already known lensed quasars in different optical bands can also be used to constrain the Hubble-Lemaître constant H_0.

7.2.6 Interferometric observations of AGN as complementary to Reverberation mapping

Advancements in interferometric techniques over the last decade have lead to carryout interferometric observations on over three dozen AGN. It has been noticed that the dust torus sizes from near-infrared interferometric observations do not follow the known relation $\Delta t \propto L^{0.5}$, instead, the half light radius $R_{1/2}$, which is used as a representative size varies as $R_{1/2} \propto L^{0.21}$ (Kishimoto et al., 2011a). In addition to that, interferometric observations have revealed complicated structures in the circumnuclear dust distribution. Also, interferometric observations too have revealed that the notion

we have on torus (as postulated in unification models) is incorrect, and instead, the torus consists of a disk along with elongated structures in the polar direction (López-Gonzaga et al., 2016). To confirm interferometric size measurements vis-a-vis the size measurements from dust reverberation, in addition to resolving the torus structure in many AGN, it is ideal to carry out interferometric observations for those AGN having dust reverberation mapping measurements. Though interferometric observations provide more information about the torus, they are in fact complementary to the dust reverberation mapping measurements. Towards this, I plan to carry out observations using GRAVITY and MATISSE at VLT, operated by the European Southern Observatory (ESO), Germany.

Bibliography

Almeyda, T., Robinson, A., Richmond, M., Nikutta, R., & McDonough, B. 2020, ApJ, 891, 26

Almeyda, T., Robinson, A., Richmond, M., Vazquez, B., & Nikutta, R. 2017, ApJ, 843, 3

Andjelić, M., Stavrev, K., Arbutina, B., Ilić, D., & Urošević, D. 2011, Baltic Astronomy, 20, 459

Antonucci, R. 1993, ARA&A, 31, 473

Arévalo, P., Uttley, P., Kaspi, S., et al. 2008, MNRAS, 389, 1479

Barbary, K. 2016, The Journal of Open Source Software, 1, 58

Barth, A. J., & Bentz, M. C. 2016, MNRAS, 458, L109

Barth, A. J., Nguyen, M. L., Malkan, M. A., et al. 2011, ApJ, 732, 121

Barvainis, R. 1987, ApJ, 320, 537

—. 1992, ApJ, 400, 502

Bentz, M. C., & Katz, S. 2015, PASP, 127, 67

Bentz, M. C., Peterson, B. M., Netzer, H., Pogge, R. W., & Vestergaard, M. 2009, ApJ, 697, 160

Bentz, M. C., Denney, K. D., Cackett, E. M., et al. 2006, ApJ, 651, 775

Bentz, M. C., Walsh, J. L., Barth, A. J., et al. 2010, The Astrophysical Journal, 716, 993

Bentz, M. C., Horne, K., Barth, A. J., et al. 2010, ApJL, 720, L46

Bentz, M. C., Denney, K. D., Grier, C. J., et al. 2013, ApJ, 767, 149

Bentz, M. C., Horenstein, D., Bazhaw, C., et al. 2014, ApJ, 796, 8

Bessell, M. S. 1979, PASP, 91, 589

Bessell, M. S., Castelli, F., & Plez, B. 1998, A&A, 333, 231

Blandford, R. D., & McKee, C. F. 1982, ApJ, 255, 419

Boroson, T. A., & Green, R. F. 1992, ApJS, 80, 109

Bovy, J., Hennawi, J. F., Hogg, D. W., et al. 2011, The Astrophysical Journal, 729, 141

Breedt, E., McHardy, I. M., Arévalo, P., et al. 2010, MNRAS, 403, 605

Brewer, B. J., Treu, T., Pancoast, A., et al. 2011, ApJL, 733, L33

Carilli, C. L., Perley, R. A., Dhawan, V., & Perley, D. A. 2019, ApJL, 874, L32

Collier, S., Peterson, B. M., & Horne, K. 2001, in Astronomical Society of the Pacific Conference Series, Vol. 224, Probing the Physics of Active Galactic Nuclei, ed. B. M. Peterson, R. W. Pogge, & R. S. Polidan, 457

Collin, S., Kawaguchi, T., Peterson, B. M., & Vestergaard, M. 2006, A&A, 456, 75

Czerny, B., Hryniewicz, K., Maity, I., et al. 2013, A&A, 556, A97

Denney, K. D., Peterson, B. M., Pogge, R. W., et al. 2010, ApJ, 721, 715

Denney, K. D., De Rosa, G., Croxall, K., et al. 2014, ApJ, 796, 134

Du, P., Hu, C., Lu, K.-X., et al. 2014, ApJ, 782, 45

Du, P., Lu, K.-X., Zhang, Z.-X., et al. 2016, ApJ, 825, 126

Du, P., Zhang, Z.-X., Wang, K., et al. 2018, ApJ, 856, 6

Edelson, R., Turner, T. J., Pounds, K., et al. 2002, ApJ, 568, 610

Edelson, R. A., & Krolik, J. H. 1988, ApJ, 333, 646

Edelson, R. A., Alexander, T., Crenshaw, D. M., et al. 1996, ApJ, 470, 364

Edri, H., Rafter, S. E., Chelouche, D., Kaspi, S., & Behar, E. 2012, ApJ, 756, 73

Ehlers, J., & Schneider, P. 1992, Gravitational Lensing, ed. J. Ehlers & G. Schäfer, Vol. 410, 1

Enya, K., Yoshii, Y., Kobayashi, Y., et al. 2002, ApJS, 141, 45

Fabian, A. C. 1999, Proceedings of the National Academy of Science, 96, 4749

Fausnaugh, M. M., Peterson, B. M., Starkey, D. A., Horne, K., & AGN Storm Collaboration. 2017, Frontiers in Astronomy and Space Sciences, 4, 55

Fedorov, P. N., Akhmetov, V. S., & Bobylev, V. V. 2011, MNRAS, 416, 403

Ferrarese, L., & Merritt, D. 2000, ApJL, 539, L9

Fitzpatrick, E. L. 1999, PASP, 111, 63

Flesch, E. W. 2017, VizieR Online Data Catalog, VII/280

Gaia Collaboration, Mignard, F., Klioner, S. A., et al. 2018, A&A, 616, A14

Gaskell, C. M., Bartel, K., Deffner, J. N., & Xia, I. 2019, arXiv e-prints, arXiv:1909.06275

Gaskell, C. M., & Peterson, B. M. 1987, ApJS, 65, 1

Gaskell, C. M., & Sparke, L. S. 1986, ApJ, 305, 175

Gebhardt, K., Bender, R., Bower, G., et al. 2000, ApJL, 539, L13

Goad, M. R., Korista, K. T., & Ruff, A. J. 2012, MNRAS, 426, 3086

Gopal-Krishna, Sagar, R., & Wiita, P. J. 1995, MNRAS, 274, 701

Graham, M., Djorgovski, S. G., Stern, D., et al. 2016, in American Astronomical Society Meeting Abstracts, Vol. 227, American Astronomical Society Meeting Abstracts #227, 243.40

Gravity Collaboration, Sturm, E., Dexter, J., et al. 2018, Nature, 563, 657

GRAVITY Collaboration, Dexter, J., Shangguan, J., et al. 2019, arXiv e-prints, arXiv:1910.00593

Gravity Collaboration, Dexter, J., Shangguan, J., et al. 2020, A&A, 635, A92

Grier, C. J., Pancoast, A., Barth, A. J., et al. 2017a, ApJ, 849, 146

Grier, C. J., Peterson, B. M., Pogge, R. W., et al. 2012, ApJ, 755, 60

Grier, C. J., Martini, P., Watson, L. C., et al. 2013a, ApJ, 773, 90

Grier, C. J., Peterson, B. M., Horne, K., et al. 2013b, ApJ, 764, 47

Grier, C. J., Trump, J. R., Shen, Y., et al. 2017b, ApJ, 851, 21

Haas, M., Chini, R., Ramolla, M., et al. 2011, A&A, 535, A73

Ho, L. C., & Kim, M. 2014, ApJ, 789, 17

Høg, E., Fabricius, C., Makarov, V. V., et al. 2000, A&A, 355, L27

Hönig, S. F., Watson, D., Kishimoto, M., & Hjorth, J. 2014, Nature, 515, 528

Hönig, S. F., Watson, D., Kishimoto, M., et al. 2017, MNRAS, 464, 1693

Horne, K., Peterson, B. M., Collier, S. J., & Netzer, H. 2004, PASP, 116, 465

Jiang, Y. F., Green, P. J., Greene, J. E., et al. 2017, VizieR Online Data Catalog, J/ApJ/836/186

Kawaguchi, T., & Mori, M. 2011, ApJ, 737, 105

Kelly, B. C., Bechtold, J., & Siemiginowska, A. 2009, ApJ, 698, 895

Kim, M., Ho, L. C., Peng, C. Y., Barth, A. J., & Im, M. 2017, ApJS, 232, 21

Kishimoto, M., Antonucci, R., Blaes, O., et al. 2008, Nature, 454, 492

Kishimoto, M., Hönig, S. F., Antonucci, R., et al. 2011a, A&A, 527, A121

—. 2009, A&A, 507, L57

—. 2011b, A&A, 536, A78

Kishimoto, M., Hönig, S. F., Beckert, T., & Weigelt, G. 2007, A&A, 476, 713

Kobayashi, Y., Sato, S., Yamashita, T., Shiba, H., & Takami, H. 1993, ApJ, 404, 94

Kochanek, C. S., & Schechter, P. L. 2004, in Measuring and Modeling the Universe, ed. W. L. Freedman, 117

Kokubo, M. 2018, PASJ, 70, 97

Kokubo, M., & Minezaki, T. 2020, MNRAS, 491, 4615

Kokubo, M., Morokuma, T., Minezaki, T., et al. 2014, ApJ, 783, 46

Korista, K. T., & Goad, M. R. 2000, ApJ, 536, 284

—. 2004, ApJ, 606, 749

Koshida, S., Yoshii, Y., Kobayashi, Y., et al. 2009, ApJL, 700, L109

Koshida, S., Minezaki, T., Yoshii, Y., et al. 2014, ApJ, 788, 159

Kovačević, A., Popović, L. Č., Shapovalova, A. I., et al. 2014, Advances in Space Research, 54, 1414

Kozłowski, S. 2017a, ApJ, 835, 250

—. 2017b, A&A, 597, A128

Kozłowski, S., Kochanek, C. S., Udalski, A., et al. 2010, ApJ, 708, 927

Krolik, J. H., Horne, K., Kallman, T. R., et al. 1991, ApJ, 371, 541

Kumar, B., Pandey, K. L., Pandey, S. B., et al. 2018, MNRAS, 476, 2075

Lemon, C. A., Auger, M. W., McMahon, R. G., & Ostrovski, F. 2018, MNRAS, 479, 5060

Li, Y.-R., Wang, J.-M., Ho, L. C., Du, P., & Bai, J.-M. 2013, ApJ, 779, 110

Li, Y.-R., Zhang, Z.-X., Jin, C., et al. 2019, arXiv e-prints, arXiv:1909.04511

Li, Y.-R., Songsheng, Y.-Y., Qiu, J., et al. 2018, ApJ, 869, 137

Lindegren, L., Lammers, U., Hobbs, D., et al. 2012, A&A, 538, A78

Lira, P., Arévalo, P., Uttley, P., McHardy, I., & Breedt, E. 2011, MNRAS, 415, 1290

Loli Martínez-Aldama, M., Czerny, B., Kawka, D., et al. 2019, arXiv e-prints, arXiv:1903.09687

López-Gonzaga, N., Burtscher, L., Tristram, K. R. W., Meisenheimer, K., & Schartmann, M. 2016, A&A, 591, A47

Lu, K.-X., Huang, Y.-K., Zhang, Z.-X., et al. 2019, ApJ, 877, 23

Lynden-Bell, D. 1969, Nature, 223, 690

Lyu, J., Rieke, G. H., & Smith, P. S. 2019, ApJ, 886, 33

MacLeod, C. L., Ivezić, Ž., Kochanek, C. S., et al. 2010, ApJ, 721, 1014

Mandal, A. K., Pradhan, B., Surdej, J., et al. 2020, Journal of Astrophysics and Astronomy, 41, 22

Mandal, A. K., Rakshit, S., Pal, I., et al. 2019, Bulletin de la Societe Royale des Sciences de Liege, 88, 158

Mandal, A. K., Rakshit, S., Stalin, C. S., Mathew, B., & Sagar, R. 2021a, MNRAS

Mandal, A. K., Rakshit, S., Stalin, C. S., et al. 2021b, arXiv e-prints, arXiv:2101.00802

Mandal, A. K., Rakshit, S., Kurian, K. S., et al. 2018, MNRAS, 475, 5330

Mandal, A. K., Rakshit, S., Stalin, C. S., et al. 2021c, MNRAS, 501, 3905

Maoz, D., Markowitz, A., Edelson, R., & Nand ra, K. 2002, AJ, 124, 1988

Marrese, P. M., Marinoni, S., Fabrizio, M., & Altavilla, G. 2019, A&A, 621, A144

Mejía-Restrepo, J. E., Lira, P., Netzer, H., Trakhtenbrot, B., & Capellupo, D. M. 2018, Nature Astronomy, 2, 63

Metzroth, K. G., Onken, C. A., & Peterson, B. M. 2006, ApJ, 647, 901

Meusinger, H., Hinze, A., & de Hoon, A. 2011, A&A, 525, A37

Minezaki, T., Yoshii, Y., Kobayashi, Y., et al. 2019, ApJ, 886, 150

Myers, A. D., Palanque-Delabrouille, N., Prakash, A., et al. 2015, ApJS, 221, 27

Narayan, R., & Bartelmann, M. 1999, in Formation of Structure in the Universe, ed. A. Dekel & J. P. Ostriker, 360

Ninan, J. P., Ojha, D. K., Ghosh, S. K., et al. 2014, Journal of Astronomical Instrumentation, 3, 1450006

Noguchi, K., Aoki, W., Kawanomoto, S., et al. 2002, PASJ, 54, 855

O'Brien, P. T., Goad, M. R., & Gondhalekar, P. M. 1995, MNRAS, 275, 1125

Oknyanskij, V. L., & Horne, K. 2001, in Astronomical Society of the Pacific Conference Series, Vol. 224, Probing the Physics of Active Galactic Nuclei, ed. B. M. Peterson, R. W. Pogge, & R. S. Polidan, 149

Oknyanskij, V. L., Lyuty, V. M., Taranova, O. G., & Shenavrin, V. I. 1999, Astronomy Letters, 25, 483

Onken, C. A., Ferrarese, L., Merritt, D., et al. 2004, ApJ, 615, 645

Pancoast, A., Brewer, B. J., & Treu, T. 2011, ApJ, 730, 139

Pancoast, A., Brewer, B. J., Treu, T., et al. 2014, MNRAS, 445, 3073

—. 2012, ApJ, 754, 49

Peng, C. Y., Ho, L. C., Impey, C. D., & Rix, H.-W. 2002, AJ, 124, 266

Peters, C. M., Richards, G. T., Myers, A. D., et al. 2015, ApJ, 811, 95

Peterson, B. M. 1993, PASP, 105, 247

—. 2011, arXiv e-prints, arXiv:1109.4181

Peterson, B. M., & Horne, K. 2004, Astronomische Nachrichten, 325, 248

Peterson, B. M., Wanders, I., Bertram, R., et al. 1998a, ApJ, 501, 82

Peterson, B. M., Wanders, I., Horne, K., et al. 1998b, PASP, 110, 660

Peterson, B. M., Ferrarese, L., Gilbert, K. M., et al. 2004, ApJ, 613, 682

Peterson, B. M., Grier, C. J., Horne, K., et al. 2014, ApJ, 795, 149

Petrov, R. G., Millour, F., Lagarde, S., et al. 2012, in , Vol. 8445, Optical and Infrared Interferometry III, 84450W

Pozo Nuñez, F., Haas, M., Chini, R., et al. 2014, A&A, 561, L8

Pozo Nuñez, F., Ramolla, M., Westhues, C., et al. 2015, A&A, 576, A73

Rafter, S. E., Kaspi, S., Chelouche, D., et al. 2013, ApJ, 773, 24

Raimundo, S. I., Vestergaard, M., Koay, J. Y., et al. 2019, MNRAS, 486, 123

Rakshit, S., Petrov, R. G., Meilland, A., & Hönig, S. F. 2015, MNRAS, 447, 2420

Rakshit, S., Stalin, C. S., & Kotilainen, J. 2020, ApJS, 249, 17

Ramolla, M., Haas, M., Westhues, C., et al. 2018, A&A, 620, A137

Rani, P., Stalin, C. S., & Rakshit, S. 2017, MNRAS, 466, 3309

Rashed, Y. E., Eckart, A., Valencia-S., M., et al. 2015, MNRAS, 454, 2918

Rathna Kumar, S., Stalin, C. S., & Prabhu, T. P. 2015, A&A, 580, A38

Refsdal, S. 1964, MNRAS, 128, 307

—. 1966, MNRAS, 132, 101

Reichert, G. A., Rodriguez-Pascual, P. M., Alloin, D., et al. 1994, ApJ, 425, 582

Richards, G. T., Fan, X., Newberg, H. J., et al. 2002, AJ, 123, 2945

Richards, G. T., Myers, A. D., Gray, A. G., et al. 2009, ApJS, 180, 67

Richards, G. T., Myers, A. D., Peters, C. M., et al. 2015, VizieR Online Data Catalog, J/ApJS/219/39

Ross, A. J., Ho, S., Cuesta, A. J., et al. 2011, MNRAS, 417, 1350

Sagar, R., Kumar, B., & Omar, A. 2019, Current Science, 117, 365

Sagar, R., Stalin, C. S., Pandey, A. K., et al. 2000, A&AS, 144, 349

Salpeter, E. E. 1964, ApJ, 140, 796

Sánchez, P., Lira, P., Cartier, R., et al. 2017, ApJ, 849, 110

Sanders, D. B., Phinney, E. S., Neugebauer, G., Soifer, B. T., & Matthews, K. 1989, ApJ, 347, 29

Schlegel, D. J., Finkbeiner, D. P., & Davis, M. 1998, ApJ, 500, 525

Schnülle, K., Pott, J. U., Rix, H. W., et al. 2015, A&A, 578, A57

Sergeev, S. G., Doroshenko, V. T., Golubinskiy, Y. V., Merkulova, N. I., & Sergeeva, E. A. 2005, ApJ, 622, 129

Shakura, N. I., & Sunyaev, R. A. 1973, A&A, 500, 33

Shapovalova, A. I., Popović, L. Č., Burenkov, A. N., et al. 2013, A&A, 559, A10

Shen, Y., Horne, K., Grier, C. J., et al. 2016, ApJ, 818, 30

Souchay, J., Andrei, A. H., Barache, C., et al. 2015, A&A, 583, A75

Stalevski, M., Fritz, J., Baes, M., & Popovic, L. C. 2013, arXiv e-prints, arXiv:1301.4244

Stalin, C. S., Jeyakumar, S., Coziol, R., Pawase, R. S., & Thakur, S. S. 2011, MNRAS, 416, 225

Suganuma, M., Yoshii, Y., Kobayashi, Y., et al. 2006, ApJ, 639, 46

Surdej, J., Hickson, P., Borra, H., et al. 2018, Bulletin de la Societe Royale des Sciences de Liege, 87, 68

Tomita, H., Yoshii, Y., Kobayashi, Y., et al. 2006, ApJL, 652, L13

Tremaine, S., Gebhardt, K., Bender, R., et al. 2002, ApJ, 574, 740

Ulrich, M.-H., & Horne, K. 1996, MNRAS, 283, 748

Ulrich, M.-H., Maraschi, L., & Urry, C. M. 1997, ARA&A, 35, 445

Urry, C. M., & Padovani, P. 1995, PASP, 107, 803

Varshni, Y. P. 1982, SScT, 5, 521

Vaughan, S., Edelson, R., Warwick, R. S., & Uttley, P. 2003, MNRAS, 345, 1271

Wagner, S. J., & Witzel, A. 1995, ARA&A, 33, 163

Wandel, A., Peterson, B. M., & Malkan, M. A. 1999, ApJ, 526, 579

Wang, J.-M., Du, P., Hu, C., et al. 2014, ApJ, 793, 108

Watson, D., Denney, K. D., Vestergaard, M., & Davis, T. M. 2011, ApJL, 740, L49

Welsh, W. F. 1999, PASP, 111, 1347

Wilhite, B. C., Vanden Berk, D. E., Kron, R. G., et al. 2005, ApJ, 633, 638

Williams, P. R., Pancoast, A., Treu, T., et al. 2018, ApJ, 866, 75

Woo, J.-H. 2008, AJ, 135, 1849

Woo, J.-H., Yoon, Y., Park, S., Park, D., & Kim, S. C. 2015, ApJ, 801, 38

Xiao, M., Du, P., Horne, K., et al. 2018, ApJ, 864, 109

Yoshii, Y., Kobayashi, Y., Minezaki, T., Koshida, S., & Peterson, B. A. 2014, ApJL, 784, L11

Zacharias, N., Finch, C., & Frouard, J. 2017, VizieR Online Data Catalog, I/340

Zhu, D., Sun, M., & Wang, T. 2017, The Astrophysical Journal, 843, 30

Zu, Y., Kochanek, C. S., & Peterson, B. M. 2011, ApJ, 735, 80

PUBLICATIONS AND CONFERENCE PRESENTATIONS

REFEREED JOURNAL PUBLICATIONS PERTAINING TO THIS THESIS

1. **A. K. Mandal**, S. Rakshit, C. S. Stalin, R. G. Petrov, B. Mathew, R. Sagar, *Estimation of the size and structure of the Broad Line Region in AGN using Bayesian approach*, **2021**, (**MNRAS**, in press)

2. **A. K. Mandal**, S. Rakshit, C. S. Stalin, D. Wylezalek, M. K. Patig, R. Sagar, B. Mathew, S. Muneer, I. Pal, *Dust Reverberation Mapping of Z229−15*, **2021**, **MNRAS**, 501, 3905

3. **A. K. Mandal**, B. Pradhan, J. Surdej, C. S. Stalin, R. Sagar, B. Mathew, *Quasar catalogue for the astrometric calibration of the forthcoming ILMT survey*, **2020**, **JApA**, 41, 22

4. **A. K. Mandal**, S. Rakshit, I. Pal, C. S. Stalin, R. Sagar, B. Mathew, *REMAP: Determination of the inner edge of the dust torus in AGN by measuring time delays*, **2019**, **Bulletin de la Société Royale des Sciences de Liège in Proceedings of the Second Belgo-Indian Network for Astronomy & Astrophysics (BINA) workshop**, 88, 158

5. **A. K. Mandal**, S. Rakshit, K. S. Kurian, C. S. Stalin, B. Mathew, S. Hoenig, P. Gandhi, R. Sagar, M. Pandge, *Determination of the size of*

the dust torus in H0507+164 through optical and infrared monitoring, **2018**, **MNRAS**, 475, 5330

ADDITIONAL REFEREED JOURNAL PUBLICATIONS

1. B. Rajput, C. S. Stalin, S. Sahayanathan, S. Rakshit, **A. K. Mandal**, *Temporal correlation between the optical and γ-ray flux variations in the blazar 3C 454.3*, **2019**, **MNRAS**, 486, 1781

2. S. Paliya Vaidehi, M. Ajello, S. Rakshit, **A. K. Mandal**, C. S. Stalin, A. Kaur, D. Hartmann, *Gamma-Ray-emitting Narrow-line Seyfert 1 Galaxies in the Sloan Digital Sky Survey*, **2018**, **ApJL**, 853

ARTICLE UNDER PREPARATION RELATED TO THIS THESIS

1. **A. K. Mandal**, S. Rakshit, C. S. Stalin, M. Schramm, B. Mathew, R. Sagar, *Black hole mass measurement of Changing-look AGN Mrk 590 using Photometric Reverberation Mapping*, **2021**, (**MNRAS**, in preparation)

REPORT ARTICLE

1. **A. K. Mandal**, A. Singh, C. S. Stalin, S. Chandra, P. Gandhi, *Near Infrared JHKs observations of the transient MAXI J1820+070 / ASASSN-18ey*, **2018**, **ATel**, 11462

SEMINARS/ CONFERENCES/ WORKSHOPS ATTENDED

1. International conference on 'Extragalactic Relativistic Jets: Cause and Effect' organised by ICTS in October, 2015.

2. Astronomical Society of India meeting; presented a poster on 'Determination of the size of the dust torus in H0507+164 through Optical−IR monitoring' at B.M. Birla Auditorium, Jaipur, India in March, 2017.

3. Young Astronomers' Meet (YAM), 2017 at IUCAA; presented a poster on 'Determination of the size of the dust torus in H0507+164 through Optical−IR monitoring' in September, 2017.

4. Belgo−Indian Network for Astronomy & Astrophysics (BINA) (09 − 12 October, 2018) at Royal Observatory of Belgium, Brussels, Belgium, presented contributory talk on 'REMAP: Reverberation Mapping of Active galactic nuclei Program'.

5. Astronomical Society of India meeting, presented contributory talk on 'Estimation of the size and structure of the BLR region using Bayesian approach' at CHRIST (Deemed to be University), Bengaluru in February, 2019.

6. "Recent Trends in the Study of Compact Objects: Theory and Observation (RETCO−IV)" during 17 − 20 April, 2019 at IUCAA, Pune and presented a poster on "Reverberation measurement of the extent of the dust torus in AGN".

7. International conference on "Mapping Central Regions of Active Galactic Nuclei" held in Guilin, China during 19−24 September, 2019: presented a contributory talk on "Echo Mapping of Active Galactic Nuclei".

8. Online international workshop "ILMT − International Liquid Mirror Telescope Workshop" conducted by Aryabhatta Research Institute of Observational Sciences (ARIES), Nainital, India during 29 June − 01 July, 2020 and presented a contributory talk on "Astrometric calibration of ILMT fields: selection of calibrators and applications".